Alma Mater Studiorum - Universitá di Bologna

DOTTORATO DI RICERCA IN FISICA

XXVII Ciclo

Settore Concorsuale di afferenza: 02/A1 – Fisica sperimentale delle interazioni fondamentali

Settore Scientifico disciplinare: FIS/01 – Fisica sperimentale

Radiative neutron capture cross section on ^{238}U at the n_TOF CERN facility: a high precision measurement

Presentata da: Federica Mingrone

Coordinatore di Dottorato
Prof. Fabio Ortolani

Relatore
Prof. Gianni Vannini

Correlatore
Dott. Cristian Massimi

Esame finale anno 2015

"Conoscere tutto, non avere più domande, non avere più curiosità, sarebbe negare la nostra stessa essenza di umani. Sapere come va a finire ogni storia, nell'attimo stesso in cui il narratore inizia a raccontartela; anzi, sapere già che il narratore ha deciso di raccontartela in quel momento, in quell'istante. Conoscere ogni cosa, ogni persona, sapere ricondurre ogni fatto a regole da noi applicabili, alla lunga renderebbe la vita un'abitudine, e gli esseri umani ad automi."

Marco Malvaldi, *Argento vivo*

Abstract

The aim of this work is to provide a precise and accurate measurement of the ^{238}U(n,γ) reaction cross section. This reaction is of fundamental importance for the design calculations of nuclear reactors, governing the behaviour of the reactor core. In particular, fast neutron reactors, which are experiencing a growing interest for their ability to burn radioactive waste, operate in the high energy region of the neutron spectrum. In this energy region inconsistencies between the existing measurements are present up to 15%, and the most recent evaluations disagree each other. In addition, the assessment of nuclear data uncertainty performed for innovative reactor systems shows that the uncertainty in the radiative capture cross-section of ^{238}U should be further reduced to 1-3% in the energy region from 20 eV to 25 keV. To this purpose, addressed by the Nuclear Energy Agency as a priority nuclear data need, complementary experiments, one at the GELINA and two at the n_TOF facility, were scheduled within the ANDES project within the 7th Framework Project of the European Commission.

The results of one of the ^{238}U(n,γ) measurement performed at the n_TOF CERN facility are presented in this work, carried out with a detection system constituted of two liquid scintillators. The very accurate cross section from this work is compared with the results obtained from the other measurement performed at the n_TOF facility, which exploit a different and complementary detection technique. The excellent agreement between the two data-sets points out that they can contribute to the reduction of the cross section uncertainty down to the required 1-3%.

Abstract

Lo scopo di questa tesi é quello di fornire una misura precisa e accurata della sezione d'urto della reazione ^{238}U(n,γ). Quest'ultima ricopre un ruolo fondamentale nelle simulazioni e nei calcoli di progetto di reattori nucleari, governando il comportamento del nucleo dei reattori. In particolare, i cosiddetti reattori veloci, che stanno conoscendo in questo periodo storico un rinnovato interesse grazie alla loro capacitá di bruciare scorie radioattive, operano sfruttando la regione di alte energie dello spettro neutronico. In questo intervallo energetico, le numerose misure presenti nei database sperimentali differiscono anche del 15%, e le principali librerie di dati nucleari sono in disaccordo tra loro. Inoltre, una valutazione delle incertezza relative ai dati nucleari di interesse per i nuovi prototipi di reattore mostra che, nella regione di energie tra 20 eV e 25 keV, l'incertezza sulla sezione d'urto di cattura radiativa su ^{238}U deve essere ridotta all'1-3%. A questo scopo, inserito dall'Agenzia per l'Energia nuclear (NEA) tra le priorit\'L, sono stati programmati tre esperimenti complementari tra loro, uno alla facility GELINA in Belgio e due alla facility n_TOF al CERN, all'interno del progetto ANDES della Commissione Europea (EC-FP7 project ANDES).

In questo lavoro di tesi sono presentati i risultati della misura della reazione ^{238}U(n,γ) compiuta ad n_TOF con un setup sperimentale costituito da due di scintillatori liquidi. La sezione d'urto ottenuta, di alta qualit\'L e precisione, é stata messa a confronto con i risultati ottenuti da una diversa misura, effettuata sempre alla facility n_TOF ma con una diversa tecnica sperimentale. L'ottimo accordo tra le due sezioni d'urto segnala che le due misure, una volta unite, andranno a contribuire alla riduzione dell'incertezza sulla sezione d'urto fino al richiesto 1-3%.

Contents

Introduction

In modern society the use of technological tools and devices has penetrated so deep to revolutionize our habits and the way we live. Energy has become one among the main fuel for social and economic development. Nowadays, the amount of energy used is massive, and it is destined to rise as population and wealth increase. Needless to say that energy-related activities have significant environmental impacts. The main and most addressed issue is the emission of greenhouse-gas that follows the production of energy through fossil fuels as coal, oil and natural gas, and which results in serious damage on climate, biodiversity and human health. In addition, the construction of power plants itself is often cause of massive land transformation, and the potential accidents as oil spills, floods from dam explosions and radioactive fallout have large and lasting regional impacts on natural areas. Moreover, the new more efficient technologies to extract fossil fuels, e.g. the shale gas development in the United States, help on one hand to enlarge the energy-source assessment giving an economically-attractive access to enormous resources, but represent, on the other hand, a potential threat to environment and health.

To avoid the business-as-usual dependence on fossil fuels, both conventional and unconventional, a map of future energy mix that incorporates alternative sources is needed. Several low-carbon resources should be part of this sustainable energy portfolio, as biofuels and waste, wind, solar, hydro power, geothermal and marine energies, and nuclear energy. Although renewable energies are clearly experiencing strong enthusiasm among society, a scenario where their share in global energy mix is dominant needs a lot of technological effort. The main issue is related to the fact that energy-production via renewable sources depends on geography and climate conditions, resulting in a supply-demand mismatch which cannot be solved by only accurate energy policies. The requirements of energy storage call for a strong development from present technologies, which imply a too large-scale solution (regardless to the massive production of chemical waste).

The case of nuclear power is complex and contradictory. The main global energy bodies as the International Energy Agency (IEA) and the World Energy Council (WEC), as well as a large part of the scientific community, comment on nuclear energy as one of the few options available at scale to reduce carbon-dioxide emissions while providing or displacing other forms of baseload generation. Nuclear power plants can contribute to the reliability and the security of the power system, reducing the dependence on foreign supplies and limiting the exposure to fuel price movements in international markets. Nevertheless, there is a strong public concern about the safety of nuclear energy production, related to potential accidents during the reactor operation and to the risk of radioactive waste and nuclear-weapons proliferation. To address this concern, significant efforts have been made in the direction of improved reactor technologies that will lead to an intrinsic-safe nuclear energy production. In particular, a renovated interest is growing nowadays towards the so-called fast neutron reactors (FNRs), that have a more efficient use of nuclear fuel and, with their high-flux of fast neutrons, can burn radioactive waste transmuting transuranic elements in less radiotoxic nuclides. Towards this direction, the Generation IV International Forum (GIF) works from 2001 to identify and select six nuclear energy systems that will be commercially available by 2030-2040. In addition, the concept of a nuclear subcritical device called accelerator driven system (ADS) is being developed both for energy production and radioactive waste disposal.

This new reactor concepts require accuracy and precision that still challenge the present knowledge of nuclear data. The prediction of the behaviour of the reactor cores depends strongly on neutron-induced reaction cross-sections, which can be measured with different experimental methods in neutron facilities, or predicted by theoretical models. In this context, the measurement of the ^{238}U radiative capture cross section is of high priority and is part of the NEA High Priority Request List [1], a compilation of the most relevant nuclear data requirements. In fact, ^{238}U constitutes more than 90% of nuclear fuel in power reactors, being one of the most important isotopes for neutron transport calculations in the active zone of a reactor. In particular, for ordinary thermal nuclear reactors the uncertainties on fundamental design parameters such as the multiplication factor, the power peak and the reactivity coefficient depend on the ^{238}U(n,γ) reaction cross-section for incident neutron energies from 0.0253 eV to 25 keV. Moreover, also the uncertainty on the the plutonium inventory in spent fuel is mostly due to the capture cross-section on ^{238}U. In the fast region of neutron spectrum, which is fundamental for calculation of fast neutron reactors, inconsistencies between published experimental data can reach the 15%, and the most recent evaluations disagree each other. To solve these inconsistencies and to lower the uncertainty in the cross section down to 1-3% in the energy range from 20 eV to 25 keV, as required from the Nuclear Energy Agency, a proposal

of three complementary measurements at the n_TOF facility at CERN (Switzerland) and at the EC-JRC-IRMM facility GELINA (Belgium) was launched [2].

The subject of this work is the determination of high-accuracy radiative capture cross-section on ^{238}U, starting from the measurement performed at the n_TOF facility in April 2012 with C_6D_6 scintillators.

The international n_TOF collaboration was formed in 2000 in order to build and operate the neutron time-of-flight facility n_TOF at CERN. Italy is an active member of the collaboration with four INFN sections and researchers from ENEA. The white neutron source of the n_TOF facility covers about eleven orders of magnitude in energy from thermal to GeV, and has unique characteristics such as a very-high instantaneous neutron flux combined to an excellent energy resolution, which allow to perform very accurate and precise measurements. For neutron capture experiments, two different experimental setups are in use at n_TOF, and both of them have been exploited to measure ^{238}U(n,γ) cross section. As outlined, this work is focused on the measurement performed via the total energy detection technique, exploiting a low solid angle detection system based on an array of liquid scintillation detectors optimized to minimize the background induced by sample-scattered neutrons. This capture setup makes measurements of capture cross-sections in the high energy region feasible. In this work, the ^{238}U(n,γ) cross section has been analyzed from 1 eV up to 480 keV.

The thesis is organized as follows: in Chapter 1 the motivations for the demand of accurate nuclear data are discussed. Starting from an overview of the energy resources, particular emphasis is given to nuclear power and nuclear reactor concepts. Among these, attention is paid to fast neutron reactors, in which ^{238}U is the main fuel exploiting the so-called U-Pu cycle. Moreover, new Generation-IV reactors and accelerator driven systems are briefly presented. The role of ^{238}U radiative neutron capture in nuclear reactor design is analyzed, and an outlook of the previous measurements performed is given.

Chapter 2 contains an introduction to neutron-nucleus reaction theory, with particular attention to the compound nucleus reactions and to the R-matrix theory with its practically useful approximations. A practical application of the resonance area analysis is presented to determine the correctness of ^{238}U resonance-spin assignment.

The n_TOF facility is described in Chapter 3, where its characteristics are reported, e.g. the neutron-producing target, the beam-line and the neutron flux. The resolution function of the n_TOF spectrometer, a fundamental input for the analysis of the cross-section resonances, is studied in details. For sake of completeness detectors and data acquisition in use at n_TOF are briefly presented together with a brief overview of the second experimental area recently built at n_TOF.

Chapter 4 contains the measurement principles and the detection techniques for neutron capture measurements. The two detection systems available at n_TOF are analyzed with their advantages and drawbacks. A detailed description of the multiple scattering contribution and, in particular, of the background induced by scattered neutrons is given. The latter is one of the main sources of background for capture measurement, and its identification presents several difficulties.

Chapter 5 is dedicated to the data reduction from raw data to experimental capture yield. The details of the measurement are given, starting from the measurement campaign and the description of the samples used. The procedure followed to extract the final capture yield is reported with all the details, and special emphasis is given to the background subtraction, a fundamental step towards the required accuracy.

The experimental yield obtained in Chapter 5 is analyzed in order to extract the ^{238}U(n,γ) reaction cross section in Chapter 6. In particular, in the so-called the resolved resonance region (1 eV $< E_n <$ 3 keV), a parametrization of the capture cross-section is obtained analyzing the experimental yield with the resonance shape analysis (RSA) code SAMMY. At higher energy, i.e. in the unresolved resonance region, the cross section is obtained applying to the experimental yield a correction factor that takes into account the self-shielding and multiple scattering effects. The cross section derived from the data analyzed in this work is compared to the values present in literature and to the other measurements part of the proposal.

Chapter 1
Nuclear data for nuclear technology

Nuclear reactions induced by neutrons play a fundamental role in nuclear technology, being at the basis of reactor physics, and are of great importance also in other fields such as Nuclear Astrophysics and fundamental Nuclear Physics. Many of the existing experimental data have been evaluated and made available through nuclear data libraries. Nevertheless, new developments in emerging nuclear technologies require more precise and accurate data, together with new measurements for a large number of isotopes. In this context, the n_TOF facility at CERN enters as an unique tool to provide accurate and precise nuclear data for science and technology.

In this chapter we will give an overview of the consumption and demand of energy in general and nuclear energy in particular. A brief introduction to nuclear power, to the problem of nuclear waste and to new nuclear reactor concepts will be given. Moreover, the role of nuclear data in energy-producing systems is discussed, with particular emphasis on the role played by the ^{238}U(n,γ) reaction.

1.1 World energy resources

The world around us has changed significantly over the past 20 years. Technology has become one of the main drivers of economic and social development. The rapid advancement of Information and Technology (IT) has transformed the way we live, being, together with the Internet, strongly present in all aspects of human life. Needless to say that practically all these technologies run on electricity, with the result that the demand of electric energy is increasing very rapidly, faster than the present supply (referred to as Total Primary Energy Supply, TPES).

Table 1.1 shows the actual values for a number of significative indicators from the World Energy Council [3] (the United Nation-accredited global energy body). The status

Table 1.1: Key indicators for 1993, 2011 and 2020, data are taken from Ref. [5] and reference therein. The acronyms used stand for: Gross Domestic Product (GDP), Total Primary Energy Supply (TPES), tonnes of oil equivalent (toe), kilos of oil equivalent (koe). The entry *other renewables* stand for all renewable energies apart from hydro.

	1993	**2011**	**2020**	**% Growth 1993-2011**
Population (billion)	5.5	7	8.1	27%
GDP (Trillion USD)	25	70	65	180%
TPES (Mtoe)	9'532	14'092	17'208	48%
Coal (Mt)	4'474	7'520	10'108	68%
Oil (Mt)	3'179	3'973	4'594	25%
Natural Gas (bcm)	2'176	3'518	4'049	62%
Nuclear (TWh)	2'106	2'386	3'761	13%
Hydro Power (TWh)	2'286	2'767	3'826	21%
Biomass (Mtoe)	1'036	1'277	1'323	23%
Other renewables (TWh)	44	515	1'999	n/a
Electricity Production/year				
Total (TWh)	12'607	22'202	23'000	76%
Per capita (MWh)	2	3	3	52%
CO_2 emissions/year				
Total CO_2 (Gt)	21	30	42	44%
Per capita CO_2 (t)	4	4	n/a	11%
Energy intensity (koe/2005 USD)	0.24	0.19	n/a	-21%

of these indicators is shown for 1993 and 2011, while for 2020 the table reports the projections made in the WEC report Energy for Tomorrow's World (1993) [4]. The comparison demonstrates that future developments are often underestimated. Even the highest projections made 20 years ago, in fact, fall far below the reality. This means that the demand for energy might grow significantly faster than expected, and if properly managed, energy resources and technologies should be available to meet this demand.

The changes in the energy industry over the past 20 years have been significant. The 2013 WEC World Energy Resources survey [5] has pointed out that there are more energy resources in the world today than ever before. However, the increase in resource assessments in 2013 can be attributed in many cases to new, more efficient technologies. As can be seen from left panel of Figure 1.1 the Total Primary Energy Supply is mostly covered by fossil fuels, a trend that will increase with the recent extraction-technology of shale gas, which despite its potential environmental damaging is cheap and readily available. From the survey, it is clear that the main fossil fuels as coal, oil and natural

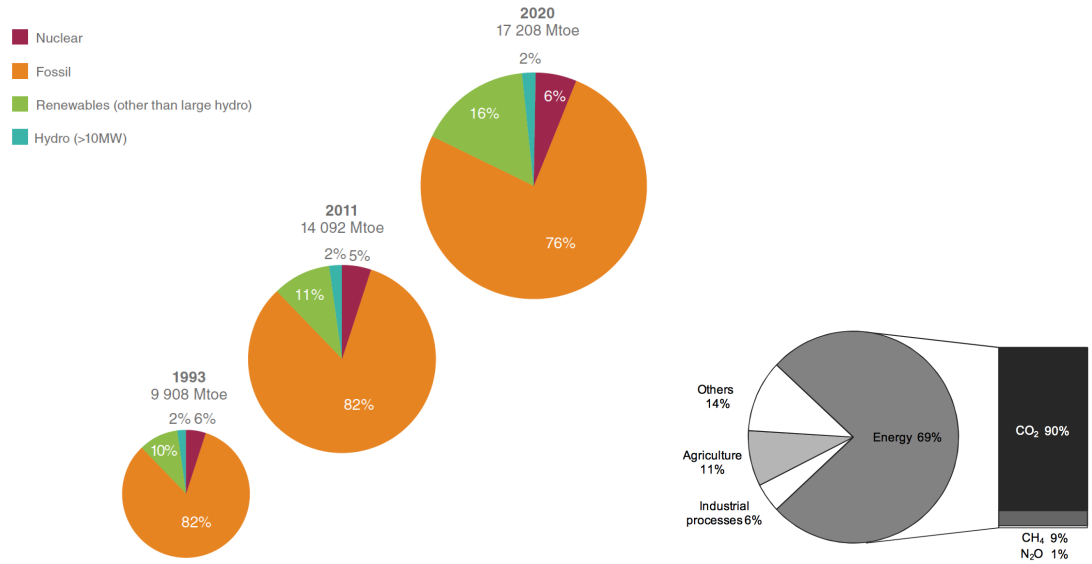

Fig. 1.1: Left panel: Total Primary Energy Supply by resource in 1993, 2011 and 2020, expressed in million tonnes of oil equivalent (Mtoe). Figure from [5]. Right panel: Shares of global anthropogenic greenhouse-gas (GHG) in 2010. Others include large-scale biomass burning, post-burn decay, peat decay, indirect N_2O emissions from non-agricultural emissions of NO_x and NH_3, Waste, and Solvent Use. Figure from [8].

gas are plentiful and will last for decades, and the International Energy Agency (IEA) [6] World Energy Outlook [7] forecasts their ongoing dominance for at least the next five decades. The drawback of this scenario is that the energy production from fossil fuels is the principal source of anthropogenic greenhouse-gas (GHG) emission [8], as shown in the right panel of Figure 1.1, with the related consequences of climate changes and biodiversity harm.

Several energy mix scenarios have been studied to improve the sustainability of energy production, which has three important and often conflicting goals:

Energy Security. Includes the effective management of primary energy supply from domestic and external sources, the reliability of energy infrastructure and the ability of energy providers to meet current and future demand.

Energy Equity. Means accessibility and affordability of energy supply across the population.

Environmental Sustainability. Deals with the achievement of supply and demand with an improvement in energy efficiencies, and with the development of energy supply from renewable and other low-carbon sources.

In Figure 1.2 the global electricity production by source, with the corresponding GHG emission, is shown for 2011 together with three different future scenarios. One is the

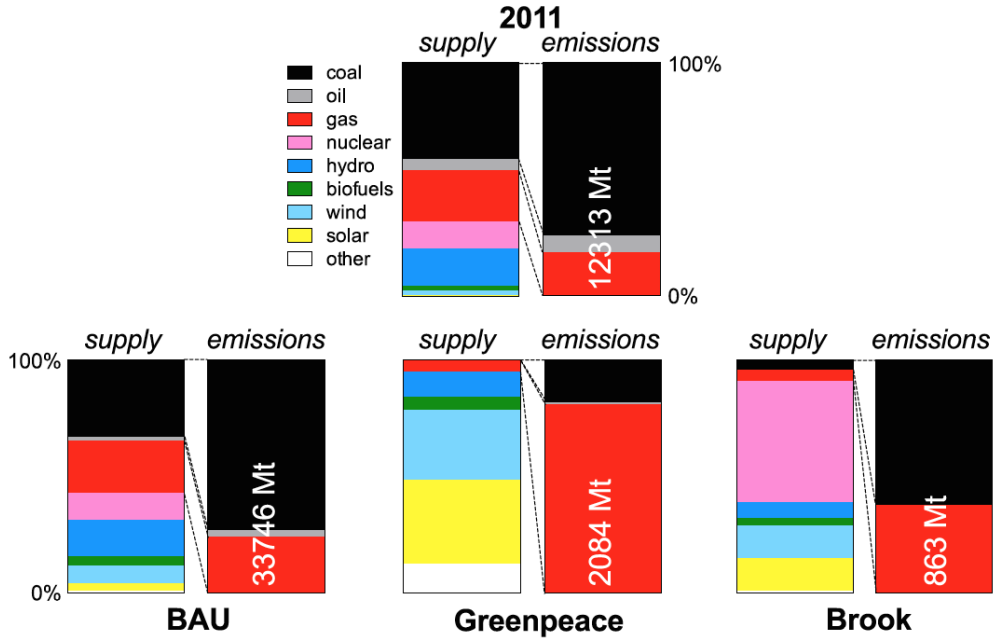

Fig. 1.2: Comparison of energy mix scenarios. Top: Global electricity production by source with the corresponding greenhouse-gas emission in 2011 [7]. Bottom: three possible future scenarios of electricity supply and greenhouse-gas emissions by source. On the left the IEA BAU scenario for 2035 [7], in the middle the Greenpeace high renewable-energy mix scenario for 2050 [9], and on the right the large nuclear-energy share scenario for 2060 by Brook [10]. Figure from [11].

business-as-usual (BAU) scenario for 2035, which already implements announced national energy policies and assumes a continue growth of energy demand related to the growth of global population (IEA, [7]). The two alternative scenarios presented are considered plausible by literature: a high renewable-energy mix with no nuclear power (scenario for 2050), which relies in a massive efficiency gain of renewable energy-production and energy-storage (Greenpeace, [9]), and an energy mix scenario for 2060 with a large share of nuclear energy combined with smaller contribution of renewables, fossil fuels and carbon capture and storage (Brook, [10]). As visible from the plots, the two alternative scenarios lead to a strong reduction of the greenhouse-gas emissions with respect to a business-as-usual dependence on fossil fuels. In the scenario proposed by Greenpeace the emissions of greenhouse-gas are reduced to $\sim 6.1\%$ of the BAU ones, while a high nuclear-energy mix is predicted to result in a reduction of the greenhouse-gas emissions down to $\sim 2.5\%$ of the BAU ones, i.e. less than a half of the high renewable-energy mix ones.

In a very recent study on the role of energy in global biodiversity conservation, Brook and Bradshaw [11] used a multi-criteria decision-making analysis (MCDMA, as described

by Hong *et al.* [12]) to classify seven important electricity-production sources: coal, gas, nuclear, biomass, hydro, wind, and solar. The analysis is based on cost and benefit, represented by seven indicators (GHG emissions, cost of electricity, dispatchability, land use, safety, solid waste and radiotoxic waste) to which a weight could be applied depending on philosophical ideas (no weighting, economic rationalism, environmentalism). The results show that, regardless to weighting, wind and nuclear energy are the electricity-production sources with the highest benefit-to-cost ratio.

Starting from the point that a reduction of greenhouse-gas emissions is mandatory, it is necessary to take into account the requirements that a new electricity generator should fulfil in order to serve as a real replacement for coal-fired electricity: it should be dispatchable (i.e. it can be delivered on demand) without need for large or expensive external storage, and it should have a reliable fuel supply. It must also have low to moderate carbon-emissions intensity, and be able to deliver a near-constant supply across a 24-hour period or longer [13]. Given that no ideal energy source is now available (i.e. one that is simultaneously low-cost, low-impact, zero-carbon emission, non-polluting, completely safe and always available on demand), a compromise among various social, economic and environmental issues should be found.

Renewable power generation, which benefit from a strong community support, continues to progress rapidly and is approaching the targets of the IEA Energy Technology Perspectives 2014 2°C Scenario (2DS) [14]. However, several drawbacks are present also for renewable-energy sources, as can be seen in Reference from [15] to [20]. In particular, main concerns are about the storage of wind and photovoltaic energy, whose production is bound to geography and weather conditions (present batteries technologies imply a very large scale storage), and about the massive land transformations required by hydroelectric dams.

The other carbon-free source of energy comes from nuclear. Despite the present public concern about nuclear power, which recently grew after the accident at the Japan's Fukushima Daiichi nuclear power plant, it is one of a limited number of options available at scale to reduce CO_2 emissions. It is worth to notice that since 1971 nuclear has avoided the release of an estimated 56 Gt of CO_2, closely equivalent to two years of emissions at current rates. Nevertheless, the issue of safety in nuclear energy production needs to be addressed, especially in relation with possible accidents in operating reactors, with the management of radioactive waste and with the prevention of the proliferation of nuclear weapons. The new-generation technologies of nuclear reactors could be the decisive step towards an unquestioned nuclear energy production in matters of intrinsic safety and nuclear waste disposal. As will be described, the design of these new reactors rests its foundations upon accurate and precise nuclear data.

1.2 Nuclear energy outlook

The nuclear industry has a relatively short history, as the first nuclear reactor was commissioned in 1954. The production of energy in nuclear reactors is based on the release of energy coming from neutron-nucleus reactions. Existing power reactors exploit fission processes, while fusion-based reactors are nowadays in the R&D phase, the main project being the International Thermonuclear Experimental Reactor (ITER) that is under construction in France.

The main source of fuel for ordinary nuclear reactors is uranium, which natural abundance is 99.275% of ^{238}U, 0.720% of ^{235}U and traces of ^{234}U ($\sim$ 0.005%). Among them, ^{235}U is the most fissile isotope, and therefore most of the commercial nuclear power reactors operating or under construction require a fuel of uranium enriched in the ^{235}U isotope. Typically, the level of enrichment needed in thermal reactors is from the natural 0.720% to 3% or 5%. It is important to notice that uranium used for nuclear weapons would have to be enriched in plants specially designed to produce at least 90% of ^{235}U.

The worldwide output of uranium has been recently increased: the 2013 WEC World Energy Resources survey shows in fact that total identified uranium resources have grown by 12.5% since 2008 and they are sufficient for over 100 years of supply based on current requirements.

The total nuclear electricity production has been growing during the past two decades and has reached an annual output of about 2600 TWh by the mid-2000s, although the three major nuclear accidents of Chernobyl, Three Miles Island and Fukushima have slowed down or even reversed its growth in some countries. The nuclear share of total global electricity production reached its peak of 17% by the late 1980s, but since then it has been falling and dropped to 13.5% in 2012. In absolute terms, the nuclear output remains broadly at the same level as before, but its relative share in power generation has decreased, mainly due to Fukushima nuclear accident.

Japan used to be one of the countries with a high share of nuclear (30%) in its electricity mix and high production volumes. Today, Japan has only two of its 54 reactors in operation. The rising costs of nuclear installations and the lengthy approval times required for new construction have had an impact on the nuclear industry. It is important to notice that the slowdown has not been global, as new countries, primarily in the rapidly developing economies in the Middle East and Asia, are going ahead with their plans to establish a nuclear industry [5, 21].

In Figure 1.3 a comparison between the world installed capacity and actual generation of nuclear energy is shown between 1993 and 2011. At the end of 2013, there were 434 operating commercial nuclear reactors worldwide, with total installed capacity of 392

GW. Nuclear power plants today account for 11% of global electricity generation, down from a peak of almost 18% in 1996.

In the IEA BAU with new policies scenario [21], forecasts on the role of nuclear energy follow conflicting trends. Global nuclear power capacity increases by almost 60%, while its share in global electricity-production rises by just one percentage point to 12%. This pattern of growth reflects the challenges that all types of thermal-generation capacity have to face in a competitive energy market, and in particular the specific economic, technical and political issues that nuclear power has to overcome. It is worth noticing that of the predicted growth in nuclear generation to 2040, China, India, Korea and Russia see the most significant increases in installed nuclear capacity.

Despite the trend of countries members of the Organisation for Economic Co-operation and Development (usually referred to as OECD countries) to phase-out nuclear, the IEA World Energy Outlook 2014 [21] addresses nuclear as an energy source that can contribute to the reliability of the power system. Nuclear power has in fact a low vulnerability with respect to disruption in international fuel markets, and is a reliable source of baseload

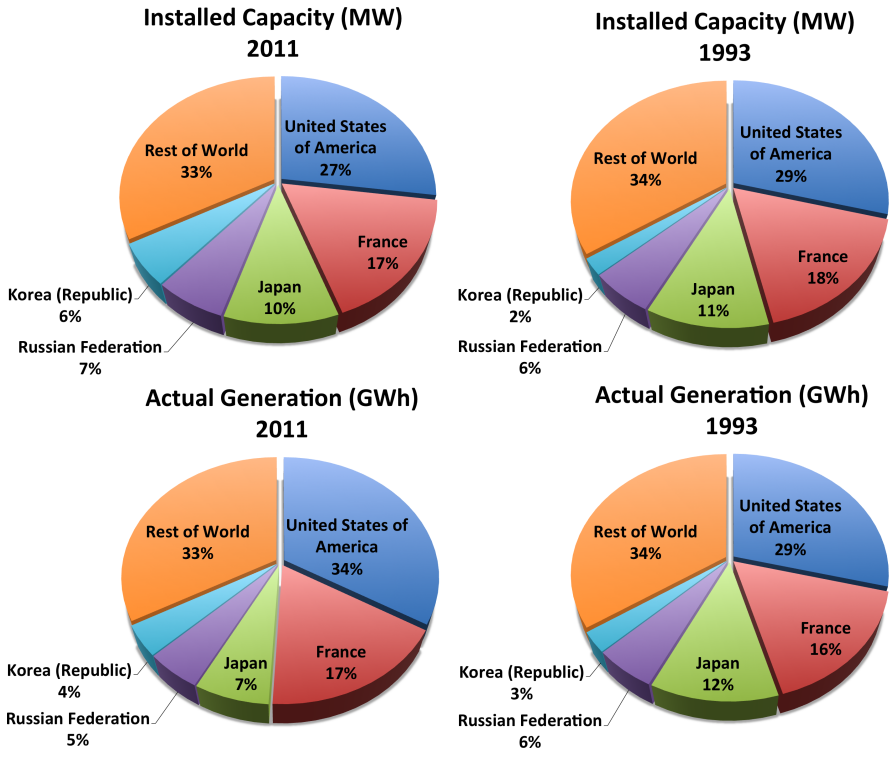

Fig. 1.3: Nuclear power top 5 countries in 2011, data from 2013 WEC World Energy Resources survey [5]. The global total installed capacity was about 364 GW in 2011 and 340 GW in 1993, while the global total actual generation was 2'385 TWh in 2011 and 2'106 TWh in 1993.

electricity[1]. For these reasons, nuclear power can enhance energy security and add stability to electricity costs: in a low nuclear-energy mix scenario, in which global nuclear share drops by 7% compared with today, indicators of energy security tend to deteriorate in countries that nowadays utilise nuclear power.

1.3 Nuclear reactors

The release of a significant amount of energy from nuclear fission reactions is at the basis of reactor technologies. To this purpose a chain reaction is required to happen, which means that neutrons produced by a fission reaction should be able to induce other fission events. In particular, to build up a chain reaction it is required that each generation has the same number of fission events than the preceding one [22, 23]. These chain reactions can be quantitatively described by the effective multiplication factor k_{eff}, which gives the net change in the number of neutrons from one generation to the next. For a reaction chain to continue it is necessary to have $k_{\text{eff}} \geqslant 1$, and to maintain a steady release of energy the criticality condition should occur (i.e. $k_{\text{eff}} = 1$). Situations of super ($k_{\text{eff}} > 1$) and sub ($k_{\text{eff}} < 1$) criticality are present in standard reactor systems only in transitions between steady states, while the new-concept of Accelerator Driven Systems (ADS) is based on a sub-critical reactor technology. In reactors which use ^{235}U as fuel, it is advantageous to moderate neutrons emitted in chain reactions down to thermal velocities, where the fission cross-section is very large ($\sigma_f \sim 580$ b). To this purpose, the best choice is to use light nuclei, i.e. pull alongside the uranium fuel a moderator-material such as graphite, water or cadmium.

Clearly the effective multiplication factor depends on the composition of the fuel and the structural material, that is it depends (*i*) on the relative number of nuclides of the different species that are present, (*ii*) on the neutron energy distribution and (*iii*) on the geometry configuration of the fuel and the moderator. These dependencies can be expressed by a five-factor formula [22]:

$$k_{\text{eff}} = \eta \varepsilon p f P_\ell . \tag{1.1}$$

Here the fast fission factor ε takes into account fast neutrons which undergo fission in ^{238}U, the resonance escape probability p indicates the number of neutrons not captured during the thermalisation process by ^{238}U (it is worth to recall that during slowing down, neutrons can be captured by large resonances in ^{238}U(n,γ)), and the thermal utilisation

[1] With baseload is intended a nuclear power-plant which can generate reliable power to consistently meet energy demand.

factor f gives the fraction of thermal neutron that are actually available to the fuel. Those three factors depend on the geometry, and they can be optimized by the design of the nuclear pile. The mean number of fission neutrons produced per thermal neutron absorbed in the fuel is given by $\eta = \nu \frac{\sigma_f}{\sigma_f + \sigma_\gamma}$, where ν is the average number of neutrons per fission events ($\nu \sim 2.5$ for thermal ^{235}U pile). The last factor of Eq. 1.1, P_ℓ, is the probability that a neutron does not leak out of the reactor, and can be split in two terms to isolate the contributions from fast and slow neutrons.

The first chain-reacting pile, constituted by a lattice of uranium blocks alternating with graphite, was constructed by Fermi and his collaborators in a squash court of the University of Chicago in 1942. Since then, nuclear power industries and engineering have been developing and improving reactor technology, and are starting to build the next generation of nuclear power reactors to fill new orders.

Four generations of reactors are commonly distinguished:

Generation I reactors. Developed in 1950-60s, and outside the UK none are still running today;

Generation II reactors. They characterize the present US and French fleets, and are the more numerous in operation elsewhere;

Generation III (and III+) reactors. They are usually referred to as Advanced Reactors, improving the Generation-II characteristics of safety, reliability of energy-dispatch, and duration of operating life. Their main characteristics are [24]:

- A standard design for each type of reactor, which expedites licensing bureaucracy and reduces capital cost and construction time;
- A simple and robust design, making them easy to operate and low vulnerable to operational upsets;
- High availability and long operating life (typically 60 years);
- Further reduced possibility of core melt accidents;
- Substantial grace period[2] so that after a shutdown the plant requires no active intervention for typically 72 hours;
- A good resistance to serious damage;
- High burn-up[3] to use fuel more fully and efficiently and to reduce the amount of waste;
- High use of burnable absorbers to extend fuel life.

[2] The term grace period is used to describe the ability of a plant to remain in a safe condition for a substantial period of time after an incident or accident, without need for any human intervention.

[3] Burn-up is a measure of the quantity of energy is extracted from a primary nuclear fuel source.

Generation IV reactors. Their designs are still under development, and will not be operational before 2030. A more detailed description will be given ahead.

Among all these types of reactors, an important parameters is the conversion (or breeding) ratio, defined as the ratio of final to initial fissile content at any given time. Because nuclear reactors cores are always evolving, the net breeding ratio is obtained integrating over the entire operating life of a reactor. In the case of U-fuelled thermal reactors the initial breeding ratio (before ^{239}Pu builds up) can be calculated as:

$$C = \frac{N\left(^{238}\mathrm{U}(n,\gamma)\right)}{N\left(^{235}\mathrm{U}(n,f)\right) + N\left(^{235}\mathrm{U}(n,\gamma)\right)}, \tag{1.2}$$

where $N\left(^{238}\mathrm{U}(n,\gamma)\right)$ is the number of capture events in ^{238}U producing ^{239}Pu, and $N\left(^{235}\mathrm{U}(n,f)\right) + N\left(^{235}\mathrm{U}(n,\gamma)\right)$ the number of absorption events that destroy ^{235}U. Reactors with $C < 1$ are called burners, that is they consume more fissile material (^{235}U, ^{239}Pu and minor actinides) than they produce (fissile ^{239}Pu). On the contrary, reactors with $C > 1$ or $C = 1$ are breeders (i.e. they are designed to produce more fissile material than they consume) or iso-breeders (i.e. they produce the same amount of fuel as they consume during operation) respectively.

Another important parameter of reactor physics is the ratio between the capture and the fission cross-section of a given isotope, being the two main reactions that can occur in rector fuels. It is defined as $\alpha(E_n) = \sigma_\gamma(E_n)/\sigma_f(E_n)$, and the convolution of this parameter for all the isotopes contained in the reactor fuel is a key parameter for assessing the neutron economy of a nuclear reactor core.

Physically, reactors could be distinguished by their neutron energy distribution: it is possible to design reactors to operate with thermal or fast neutrons. From a technological point of view, it is possible to distinguish several type of reactors from the type of fuel and the coolant and moderation material. Nuclear power plant in operation are listed in Table 1.2.

Thermal reactors

The neutron spectrum in a thermal reactor is defined essentially by the moderator material, which is usually coincident with the coolant. To this purpose, the most used material in electricity-producing reactors is light water, either pressurized (also referred to as Pressurized Water Reactors - PWR) or boiling (also referred to as Boiling Water Reactor - BWR).

Table 1.2: Nuclear power plants in commercial operation, data from the International Atomic Energy Agency (IAEA), end of 2013. The GWe units is 1 GW of electrical output.

Reactor type	**Main Countries**	**Number**	**GWe**	**Fuel**	**Coolant**	**Moderator**
Pressurised Water Reactor (PWR)	US, France, Japan, Russia, China	273	253	Enriched UO_2	Water	Water
Boiling Water Reactor (BWR)	US, Japan, Sweden	81	76	Enriched UO_2	Water	Water
Pressurised Heavy Water Reactor (PHWR)	Canada	48	24	Natural UO_2	Heavy Water	Heavy Water
Gas-cooled Reactor (AGR & Magnox)	UK	15	8	U (metal), Enriched UO_2	CO_2	Graphite
Light Water Graphite Reactor (RBMK & EGP)	Russia	15	10.2	Enriched UO_2	Water	Graphite
Fast Neutron Reactor (FBR)	Russia	2	0.6	PuO_2, UO_2	Liquid Sodium	None

PWR is the most common type, with over 230 in use for power generation and several hundred more employed for naval propulsion [24]. It uses ordinary water both as coolant and moderator: a primary cooling circuit flows into the reactor core and is kept under very high pressure, in order to prevent the boiling of water. The steam that will drive the turbine is generated afterwards in a secondary circuit.

The design of Boiling Water Reactors is similar to the PWRs one, except that there is only a single circuit in which the water is at low pressure. Therefore, a two-phase mixed fluid (water and steam) flows in the upper part of the reactor core.

Another common type of thermal reactor is the Pressurized Heavy Water Reactor (PHWR), developed since the 1950s in Canada as the CANDU reactor, which use heavy water (D_2O) as coolant and moderator. Because D_2O is a moderator that absorbs much less neutrons than ordinary water does (being the radiative capture cross section negligible compared to water), PHWRs use natural uranium oxide as fuel with no need of enrichment [25].

Different concept of thermal reactors can be obtained using gas as coolant, if a moderator such as graphite is employed. For instance, the Advanced Gas Reactors (AGR), cooled with CO_2, and the High-Temperature Gas Cooled reactors (HTGR), cooled with He.

Fast Neutron Reactors (FNR)

Fast neutron reactors (FNRs) rely on a chain reaction in which neutrons should not be thermalized, and therefore require no moderator at all. Fission reactions are induced at relatively high energy, thanks to inelastic collisions within the fuel that lead a significant fraction of the neutron spectrum to be in the energy range from keV to MeV. The advantage is that fertile materials as ^{238}U can be used as fuels, and therefore nuclear data in this relatively high-energy region, called Unresolved Resonance Region (URR), are extremely important. In the case of the so-called U/Pu cycle, the fertile ^{238}U material is used as a converter to produce the fissile ^{239}Pu through capture reactions and β decays:

$$^{238}\mathrm{U} + n \rightarrow {}^{239}\mathrm{U} \xrightarrow{23\ \mathrm{min}} {}^{239}\mathrm{Np} + \mathrm{e}^- + \bar{\nu} \tag{1.3}$$

$$^{239}\mathrm{Np} \xrightarrow{2.3\ \mathrm{d}} {}^{239}\mathrm{Pu} + \mathrm{e}^- + \bar{\nu} \tag{1.4}$$

Fast reactor technologies offer the prospect of a vastly more efficient use of uranium resources with respect to thermal ones, together with the ability to burn actinides, i.e. the long-lived component of high-level nuclear wastes. In the upper part of the neutron energy spectrum conditions for breeding are optimal, thanks to the predominance of ^{239}Pu neutron-induced fission over capture ($\alpha \sim 0.03$). For this reason, FNR can be designed to have a breeding ratio C (see Eq.1.2) larger than unity (Fast Breeder Reactors, FBRs), even if many new designs opt for a net consume of fissile material including Pu.

About 20 Fast Neutron Reactors have already been operating, some since the 1950s, and some supplying electricity commercially. However significant technical and materials problems were encountered, which nowadays technologies are starting to overcome [26, 27]. There are several hints from the scientific community that nuclear fission will continue to play an important role in meeting future energy needs, complying with the expectation for energy production with minimal impact on climate, environment and health. In this context, the development of innovative fast neutron systems and closed fuel cycles is regarded as a necessary step to ensure a long term sustainable energy supply [28]. Moreover, there is renewed interest in fast reactors due to their ability to fission actinides, including those which may be recovered from ordinary reactor used fuel. The fast neutron environment minimizes neutron capture reactions and maximizes fissions in actinides, which means less long-lived nuclides in radioactive waste.

In Europe, Phenix (France, 1973 to 2009) and Superphenix (France, 1985 to 1998) are two examples of operating fast breeder reactors, the second being a 1250 MWe commercial prototype.

Generation-IV reactors

The Generation IV International Forum (GIF) was initiated in 2000 and formally chartered in mid 2001 [29]. It is a co-operative international endeavour organised to carry out the research and development (R&D) needed to establish the feasibility and performance capabilities of the next generation nuclear energy systems. It counts 13 member countries[4], the majority of which is committed to participate in the development of the next generation of nuclear technology.

The goals adopted by GIF provided the basis to identify and selecting six nuclear energy systems for further development that, depending on their respective degrees of technical maturity, are expected to become available for commercial introduction around 2030-2040. The six selected systems employ a variety of reactors, energy conversion and fuel cycle technologies. Their designs exploit thermal and fast neutron spectra, closed and open fuel cycles and a wide range of reactor sizes from very small to very large.

Gas-Cooled Fast Reactor (GFR) [30]. The GFR system is a high-temperature fast neutron reactor cooled by helium, with a closed fuel cycle. It combines the advantages of fast-spectrum systems for long-term sustainability of uranium resources and waste minimisation (through fuel multiple reprocessing and fission of long-lived actinides), with those of high-temperature systems (high thermal cycle efficiency and industrial use of the generated heat).

Lead-Cooled Fast Reactor (LFR) [31]. This fast reactor operates at high temperature and is cooled by molten lead or lead-bismuth eutectic (LBE) liquids, characterized by low-pressure, no chemical interactions and very good thermodynamic properties. It would have multiple applications including production of electricity, hydrogen and process heat.

Molten Salt Reactor (MSR) [32]: The MSR is distinguished by its core in which the fuel is not solid but dissolved in molten fluoride salt. This technology, firstly studied more than 50 years ago, is now promising as a long term alternative to solid-fuelled fast neutrons reactors. Being a complete different concept of nuclear reactor, key feasibility issues focus on a dedicated safety approach and the development of molten salt technology and control tools in order to limit corrosion rate of structural materials.

[4] The nine founding members are those that signed the GIF Charter in July 2001: Argentina, Brazil, Canada, France, Japan, the Republic of Korea, the Republic of South Africa, the United Kingdom and the United States. Subsequently, the GIF Charter was signed by Switzerland in 2002, Euratom in 2003, and by the People's Republic of China and the Russian Federation in 2006.

Supercritical-Water-Cooled Reactor (SCWR) [33]. This is a very high-pressure water-cooled reactor, which operates above the thermodynamic critical point of water (374°C, 22 MPa). This results in a thermal efficiency about one third higher than today's light water reactors, from which this design can be developed incrementally step-by-step. The reactor core may have a thermal or a fast-neutron spectrum, depending on its design.

Sodium-Cooled Fast Reactor (SFR) [34]. The SFR uses liquid sodium as the reactor coolant, allowing high power density with low coolant volume fraction and operation at low pressure. The advantages of sodium-cooling is that the oxygen-free environment prevents corrosion. However, sodium reacts chemically with air and water and therefore requires a sealed coolant system.

Very-High-Temperature Reactor (VHTR) [35]. The Very High Temperature Reactor (VHTR) is primarily dedicated to the cogeneration of electricity and hydrogen, the latter being extracted from water by using thermo-chemical, electro-chemical or hybrid processes. These are graphite-moderated, helium-cooled reactors, and can be considered as the next development of high-temperature gas-cooled reactors.

The European Commission in 2010 launched the European Sustainable Nuclear Industrial Initiative (ESNII) [36], which will support three Generation IV fast reactor projects as part of the European Union's plan to promote low-carbon energy technologies: the Astrid sodium-cooled fast reactor (SFR) proposed by France, the Allegro gas-cooled fast reactor (GFR) supported by central and eastern Europe, and the Myrrha lead-cooled fast reactor (LFR) technology pilot proposed by Belgium.

1.3.1 Nuclear proliferation risks

The initial development of nuclear technology was related to military interests during World War II. Two nuclear bombs made from uranium-235 and plutonium-239 were dropped in August 1945 on Japan's Hiroshima and Nagasaki respectively. In this tremendous way the immense and previously unimaginable power of the atom had been demonstrated.

Afterwards, attention turned to civil applications. In the course of half a century nuclear technology has enabled access to a virtually unlimited source of energy at a time when constraints are arising on the use of fossil fuels. The fundamental question remains: to what extent and in what ways does nuclear power generation enhance or alleviate the risks from nuclear weapons?

This important concern leads to the Non-Proliferation Treaty (NPT), with the aim to prevent the spread of nuclear weapons and their technology, to promote the peaceful uses of nuclear energy, and to assists the goal of disarmament. The Treaty establishes a safeguards system under the responsibility of the International Atomic Energy Agency (IAEA), which also plays a central role under the Treaty in areas of technology transfer for peaceful purposes.

From a merely technological point of view, nuclear power reactors themselves are not a proliferation concern, while enrichment and reprocessing technologies have been the cause of proliferation through illicit or not-safeguarded use. In particular, the abundance of Pu in the spent fuel could be a source of nuclear weapon proliferations, together with the presence of ^{243}Am that in the long term would produce ^{239}Pu via α-decay and subsequent β-decay. For these reasons, the new technologies of fast neutron reactors are particularly interesting, in the sense that they can be used as burners of ex-military plutonium and that they allow the use of fuel cycle with less amount of Pu in nuclear waste.

1.3.2 Nuclear waste

As well as in all industrial processes, the thermal generation of electricity produces wastes. Radioactive wastes may occur either in gaseous form (ventilation exhaust), in liquid form (highly radioactive liquids from the reprocessing of spent fuel) or in solid form (vitrified waste from spent fuel reprocessing or used fuel when considered as a waste).

During the normal operation of a nuclear power plant, radioactive nuclear wastes are generated by unstable fission fragments from fission reactions, by neutron induced reactions such as (n,γ) or (n,α) on heavy nuclei (uranium or even higher atomic-mass elements) that produce transuranic elements, or by neutron activation of moderation and structural materials. Transuranic elements usually decay by α and β emission with relatively long half-life, activation products are mainly γ-ray emitters and fission fragments undergo β-decay.

Classification schemes for radioactive waste may be developed from different bases, according to its physical or chemical form, its radioactivity (specific activity, emitted radiation or radiotoxicity), safety issues, regulatory-related aspects or process engineering requirements.

Generally, radioactive waste was divided into three classes: high level waste (HLW), intermediate level waste (ILW) or low level waste (LLW), but in 2009 the IAEA extended the classification deriving six different classes of wastes [37]:

Exempt waste (EW): Waste that meets the criteria for clearance, exemption or exclusion from regulatory control for radiation protection purposes as described in Ref. [38].

Very short lived waste (VSLW): Waste that can be stored over a limited period of up to a few years to decay in less-radioactive products. This class includes waste containing primarily radionuclides with very short half-lives often used for research and medical purposes.

Very low level waste (VLLW): Waste that does not necessarily meet the criteria of EW, but that does not need a high level of containment and isolation and, therefore, is suitable for disposal in near surface landfill-type facilities with limited regulatory control. Such landfill-type facilities may also contain other hazardous waste. Typical waste in this class includes soil and rubble with low levels of activity concentration. Concentrations of longer lived radionuclides in VLLW are generally very limited.

Low level waste (LLW): Waste that is above clearance levels, but with limited amounts of long lived radionuclides. Such waste requires robust isolation and containment for periods of up to a few hundred years and is suitable for disposal in engineered near surface facilities. This class covers a very broad range of waste. LLW may include short lived radionuclides at higher levels of activity concentration, and also long lived radionuclides, but only at relatively low levels of activity concentration.

Intermediate level waste (ILW): Waste that, because of its content of long lived radionuclides, requires a greater degree of containment and isolation than that provided by near surface disposal. However, ILW needs no (or only limited) provision for heat dissipation during its storage and disposal. ILW may contain long lived radionuclides, in particular α-emitters, that will not decay to a level of activity concentration acceptable for near surface disposal during the time for which institutional controls can be relied upon. Therefore, waste in this class requires disposal at greater depths, of the order of tens to hundreds of metres.

High level waste (HLW): Waste with levels of activity concentration high enough to generate significant quantities of heat by the radioactive decay process, or waste with large amounts of long lived radionuclides that need to be considered in the design of a proper disposal facility. Disposal in deep, stable geological formations usually several hundred metres or more below the surface is the generally recognized option for disposal of HLW.

Transuranic elements (TRU) and fission fragments (FF) are the two main components of high-level nuclear waste, representing the 1.1% and the 4% respectively of the exhausted nuclear fuel [39]. The minimization of the radiotoxicity of these HLW before

Table 1.3: List of the principal nuclides present in spent fuel with their concentration expressed as weight percent (wt%), their half life and radiotoxicities. Transuranic concentrations come from a UOX PWR fuel with a final burn-up[5]of 52 GWd/MTU (data from [41]). Fission fragments concentrations come from the discharge isotopic composition of a Westinghouse Electric (WE) assembly with initial enrichment of 4.5 wt% that has accumulated 45 GWd/MTU burn-up (data from [42]).

Isotope	Concentration [wt%]	Half-life [years]	Radiotoxicity [40] [Sv/Bq]
Transuranic - TRU			
^{237}Np	6.21	2.14×10^{6}	2.3×10^{-5}
^{238}Pu	2.85	87.74	4.6×10^{-5}
^{239}Pu	44.50	2.411×10^{4}	5.0×10^{-5}
^{240}Pu	21.75	6.550×10^{3}	5.0×10^{-5}
^{241}Pu	13.94	14.4	9.0×10^{-7}
^{242}Pu	7.81	3.763×10^{5}	4.8×10^{-5}
^{241}Am	1.75	432.6	4.2×10^{-5}
^{243}Am	0.01	7.370×10^{3}	4.1×10^{-5}
^{244}Cm	1.08	18.11	2.7×10^{-5}
^{245}Am	0.08	8.532×10^{3}	3.9×10^{-5}
Fission Fragments - FF			
^{90}Sr	1.54	28.9	3.6×10^{-8}
^{99}Tc	1.93	2.111×10^{5}	8.9×10^{-10}
^{129}I	0.39	1.6×10^{7}	3.6×10^{-8}
^{137}Cs	3.85	30	4.6×10^{-9}

burying it in geological disposal can be considered the main issue to be addressed in a framework of nuclear energy sustainability. Radiotoxicity gives an indication of the potential capacity of a radioisotope to damage biological cells and tissues. This quantity is defined as the product of the activity and the effective dose coefficient $R = A \times F_d$, the latter being a measurement of the power of the radiation and of its effect on biological organism. The value, isotope per isotope, of the effective dose coefficient is determined by the International Commission on Radiological Protection (ICRP) and is given in Sv/Bq. In Table 1.3 the main TRU and FF isotopes are listed together with their radiotoxicities.

[5] Burn-up, also known as fuel utilization, is a measure of how much energy is extracted from a primary nuclear fuel source. It is measured both as the fraction of fuel atoms that underwent fission, in fissions per initial metal atom (%FIMA), and as the actual energy released per mass of initial fuel, in gigawatt-days per metric ton of uranium (GWd/MTU).

1.4 Nuclear waste transmutation

To reduce the radiotoxicity of nuclear waste, Partitioning and Transmutations (P&T) technologies have a great impact lowering significantly the risk and simplifying the conditions of the final storage. This prospects have been studied within the RED-IMPACT project [43] of the European Union. The main idea of P&T is to chemically process the HLW, isolating the different elements (partitioning) and to design a nuclear device capable of burning a minor actinide enriched fuel (transmutation) in such a way that the volume and radiotoxicity of the HLW is reduced. Transmutation of nuclear waste is therefore a fundamental step towards a safe and sustainable managing of nuclear waste, transforming the radioactive isotopes into stable or less radiotoxic ones via neutron-induced capture and neutron fission reactions.

A further available option is the reduction of the long-term radiotoxic inventory of nuclear waste by using different fuel cycles in existing or new concept reactors. A fuel cycle based on thorium, for example, will produce much less radiotoxic actinides with respect to fuel based on U-cycle and constitutes a promising alternative. Research activities exist on detailed studies of isotopic evolution in several deployment scenarios, but also on the basic nuclear data necessary for these applications [44, 45].

Transmutation can change the nuclear properties drastically. For transuranic elements, key processes of waste transmutation are fission reactions, as:

$$n + {}^{239}\mathrm{Pu}\ (2.44 \times 10^4\ \mathrm{y}) \xrightarrow{\text{fission}} {}^{134}\mathrm{Cs}\ (2\ \mathrm{y}) + {}^{104}\mathrm{Ru}\ (\text{stable}) + 2n + 200\ \mathrm{MeV}, \quad (1.5)$$

where the half-life of each isotope is given in parenthesis. These reactions require a nuclear device with a fast neutron spectrum as fast neutron reactors, in order to maximize the fission to capture ratio. On the other hand, for fission fragments the main transmutation processes are neutron capture reactions and beta decay, which can have a substantial rate at thermal energies. As an example, transmutation of the long-lived fission products ^{99}Tc and ^{129}I is feasible in a thermal reactor through neutron capture processes:

$$n + {}^{99}\mathrm{Tc}\ (2.11 \times 10^5\ \mathrm{y}) \xrightarrow{\text{capture}} {}^{100}\mathrm{Tc} \xrightarrow{\beta\ (16\ \mathrm{s})} {}^{100}\mathrm{Ru}\ (\text{stable}) \qquad \text{and} \quad (1.6)$$

$$n + {}^{129}\mathrm{I}\ (1.57 \times 10^7\ \mathrm{y}) \xrightarrow{\text{capture}} {}^{130}\mathrm{I} \xrightarrow{\beta\ (12.4\ \mathrm{h})} {}^{130}\mathrm{Xe}\ (\text{stable}). \quad (1.7)$$

In Figure 1.4 the evolution in time of the contribution of each transuranic isotope to the total radiotoxicity of the nuclear waste is given in mSv per initial ton of Uranium. The figure indicates how much the transmutation of the different isotopes is fundamental to reduce the radiotoxicity and simplify the storage of radioactive waste.

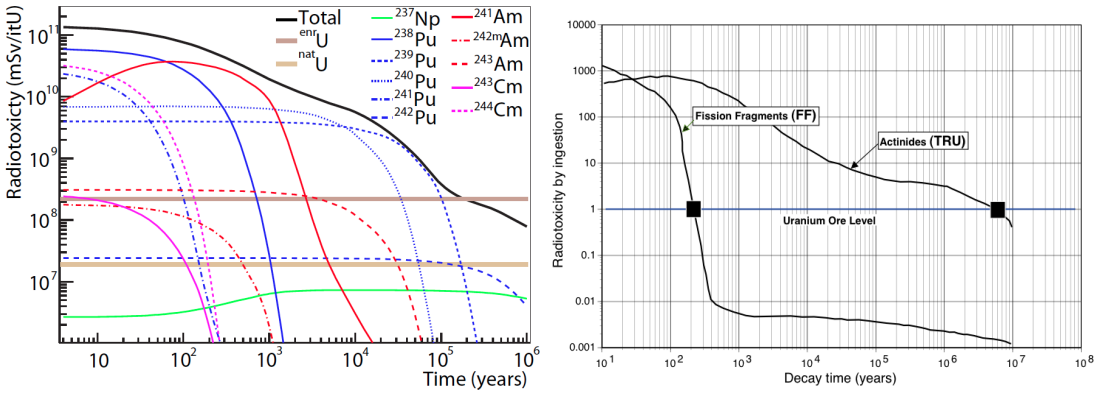

Fig. 1.4: Left panel: Contribution of different isotope to the radiotoxicity of the nuclear waste. Right panel: Evolution in time of the potential radiotoxicity of transuranic elements and fission fragments.

The transmutation process can take place in a high neutron flux environment. As outlined, for fission fragments the transmutation proceeds through capture reactions, so that the neutron flux present in thermal reactors can be used. For actinides (in particular Np, Am, Cm) the most effective process is fission, whose cross-section however may present a threshold around 1 MeV. For this reason fast reactor are needed. An alternative solution is to use an Accelerator Driven System (ADS), a subcritical nuclear device with a fast neutron spectrum. This new reactor concept will be briefly described in the next section.

As described, all the transmutation processes need neutron induced reactions, and therefore the design of an efficient transmutation requires extremely accurate and precise nuclear data. In particular, precise values of the cross sections of neutron-induced reactions are mandatory.

1.5 Accelerator Driven System (ADS)

The concept of Accelerator Driven Systems (ADS) refers to a nuclear device obtained combining a subcritical reactor ($k_{\text{eff}} < 1$) with a particle accelerator. Its basic concepts have been introduced by Rubbia *et al.* in the mid-1990's for the design of a nuclear reactor based on the Th-U fuel cycle, the so-called Energy Amplifier [46].

In a subcritical reactor the fission chain-reaction needs to be sustained by an external source of neutrons, which in the case of ADS consists in a proton accelerator coupled to a spallation target. The neutrons emitted through spallation reactions exit the target with an energy of few MeV (high-energy neutron spectrum) and reach the nuclear fuel,

which can be enriched in minor actinides. Depending on the spallation target, the average number of neutrons produced and the energy of the neutron spectrum can be varied, so tu fulfil the requirements of the chosen fuel and aim (e.g., nuclear waste transmutation or energy production).

The ADS leads to significative improvements both on safety (during the operating life of the reactor and related to radioactive waste) and technical point of view:

- The subcritical operation increases the flexibility of the system, allowing the use of fuel that can have a high concentration of MA compared to those of fast critical reactors (for nuclear waste transmutation purpose) or that does not have a self-sustained fission chain (for energy production), as the ^{232}Th$-^{233}$U cycle:

$$^{232}\mathrm{Th}(n,\gamma)^{233}\mathrm{Th} \xrightarrow{\beta^- \text{ (22 m)}} {}^{233}\mathrm{Pa} \xrightarrow{\beta^- \text{ (27 d)}} {}^{233}\mathrm{U}; \tag{1.8}$$

- The very high flux of fast neutrons promotes transmutation fission reactions on transuranic isotopes, and, as in fast neutron reactors, capture reactions to convert fertile isotopes (^{232}Th, ^{238}U) in fissile fuel (^{233}U, ^{239}Pu);
- Because the fission chain-reaction is sustained only with an additional source of neutrons external to the reactor, it can be considered intrinsically safe. In fact, whenever the neutron source is turned off, the chain-reaction ceases. In this way severe accidents like core melting can be avoided without any human intervention in the reactor core.
- The possibility to use different fuel from ^{235}U means that nuclear energy production could be independent from the availability of uranium resources[6]. Moreover, the use of elements with lower atomic number (e.g. ^{232}Th) as nuclear fuel decreases the abundance of plutonium and long lived minor actinides in radioactive waste, minimizing radiotoxicity, decay heat and proliferation issues.

Besides the advantages related to accelerator driven systems, there are several topics that need to be addressed before the industrial scale of ADS can be reached [47]. In particular, measurements of accurate nuclear data are needed to reduce the design uncertainties. Moreover, from a technical point of view, ADS have a less reliable power-production due to accelerator downtime, and a large amount of volatile radioactive isotopes is produced in the spallation target.

The conceptual design of the ADS has been largely discussed, and what was claimed to be the world's first ADS experiment was begun in March 2009 at the Kyoto University Research Reactor Institute (KURRI), utilizing the Kyoto University Critical Assembly (KUCA) [48]. Among the several ADS research reactors under study, the Indian Atomic

[6] As an example, thorium is three to four times more abundant than uranium in the earth crust and is widely distributed in nature as an easy mining resource in many countries.

Energy Commission is proceeding with design studies for a 200 MWe PHWR accelerator driven system fuelled by natural uranium and thorium [49]. In Europe, the Belgian Nuclear Research Centre (SCK.CEN) is planning to begin construction on the MYRRHA (Multipurpose Hybrid Research Reactor for High-tech Applications) [50] research reactor at Mol in 2015. Initially it will be a 57 MWt ADS, consisting of a proton accelerator delivering a 600 MeV, 2.5 mA (or 350 MeV, 5 mA) proton beam to a liquid lead-bismuth spallation target, that in turn couples to a Pb-Bi cooled subcritical fast nuclear core. Moreover, in mid-2014 the Swedish nuclear regulator issued a conditional licence for construction of the European Spallation Source (ESS) facility in Lund [51]. This research facility will feature the world's most powerful neutron source, and will be used for material research and life sciences. It is designed around a linear accelerator which produces intense pulses of neutrons from a heavy metal target, which are led through several beam-lines to experimental stations. Completion is scheduled by 2019, and the facility should be fully operational by 2025.

1.6 The role of Nuclear Data

As described in previous sections, the accurate knowledge of neutron cross-sections plays a major role in the design and exploitation of critical and subcritical nuclear systems. In particular, the prediction of the behaviour of the reactor cores depends strongly on capture and fission cross-sections data. Parameters such as the multiplication factor k_{eff}, the power peak (i.e. the ratio between the maximum and the average peak density), the reactivity coefficients ρ (i.e. the deflection of reactors from critical state, $\rho = \frac{k_{\text{eff}}-1}{k_{\text{eff}}}$), the nuclear density variation of isotopes due to transmutation and the decay heat strongly depend on the Nuclear Data (ND) used in calculations and projections. Because nuclear data govern several constraints that concerns safety and criticality, but also modelization and development, a standardized formats for storage and retrieval of evaluated nuclear data has been developed, with the compilation of nuclear-data libraries.

1.6.1 Nuclear data libraries

Published experimental and theoretical results on neutron-nuclear reactions are collected by several collaborating nuclear data agencies worldwide. In particular, the experimental nuclear reaction databases, such as EXFOR (Experimental Nuclear Reaction Data) [52],

make available nuclear reaction data from experimental measurements together with their bibliographic informations, as well as details on the experimental method used.

Furthermore, to be suitable for the application in nuclear reactor designs, an evaluated data set for a particular isotope needs to be completed. This means that evaluators have to combine experimentally measured cross section data with predictions of nuclear model calculations in order to obtain a single complete data-set. The evaluated data set is adopted in the library after extensive benchmarking and reviewing. An evaluated library, like JEFF (Europe) [53], JENDL (Japan) [54], ENDF/B (United States) [55], BROND (Russia) [56] or CENDL (China) [57], contains several sub-libraries, each one corresponding to a particular type of data. These nuclear reaction databases contain, in fact, evaluated (recommended) cross-sections, angular distributions, fission products yields, thermal neutron scattering, photo-atomic and other data, with emphasis on neutron-induced reactions. All the data are stored in the internationally adopted format ENDF-6 [58], originally developed for the ENDF library but now adopted for all other libraries.

New data needs or newly available experimental data may lead to new evaluations. An updated library can be released only when the full library has passed extensive testing, giving coherent results in benchmarks on a variety of applications like reactor criticality calculations. A recent project, CIELO (Collaborative International Evaluated Library Organization) [59], aims to produce an evaluated library common to Europe, North America and Asia. The focus of this latter project will initially be on a small number of the highest-priority isotopes, among which the ^{238}U is inserted due to its key relevance within the nuclear industry, as will be described in the following section.

1.7 Radiative capture on ^{238}U

The cross section for the ^{238}U(n,γ) reaction is an important quantity for the design and safe operation of nuclear reactors. In particular, the higher energy region is of special importance for innovative reactor systems, as previously described, because Generation-IV reactors as well as ADSs are designed to operate with a high-energy neutron spectrum.

In Table 1.4 the uncertainties on fast and thermal reactors design parameters are listed, all related to ^{238}U capture cross-section. Moreover, the ^{238}U capture cross section uncertainty affects the uncertainty on Pu isotope density at the end of the fuel cycle for the 1.1% for ^{239}Pu, the 0.2% for ^{240}Pu and the 0.1% for ^{241}Pu.

Despite the importance of this cross section, inconsistencies between experimental data published in the literature may reach 15%. Therefore, the capture cross section

Table 1.4: Fast and thermal reactor systems: uncertainties (%) due to ^{238}U capture cross section. With Void is intended the coolant void reactivity coefficient.

	Reactor	k_{eff}	Void	Power Peak
Fast Nuclear Reactors	**ABTR**	0.26		
	SFR	0.07	1.24	
	GFR	0.41		0.30
	LFR	0.25		
Thermal Nuclear Reactors	**PWR**	0.26		
	VHTR	0.19		

for ^{238}U in both the resolved (1 eV $< E_n <$ 20 keV) and unresolved ($E_n >$ 20 keV) resonance region is on the Nuclear Data High Priority Request List (HPRL) [1]. This list represents a compilation of the most important nuclear data requirements and is maintained by the Nuclear Energy Agency of the OECD. The cross section between 22 eV and 25 keV is requested with an uncertainty between 1% and 3%. Moreover, the ENDF/B-VII evaluation made some small modifications to the standards capture result motivated by the shape predicted by model calculations [60] as well as by improved MCNP simulation performance. As these modifications exceed the uncertainties of the standards evaluation, future work is needed to resolve these differences.

To both these purposes complementary experiments, one at the EC-JRC-IRMM laboratory GELINA [61] and two at the CERN n_TOF facility [62, 63], were scheduled within task 1.2 of the FP7 project ANDES of the European Commission [64]. The experimental techniques used are presented in Chapter 4. Combining results from two different detectors and independent experimental principles, the overall systematic uncertainty is reduced, so that the measurements would help to solve the existing open problems.

The focus of this work is the ^{238}U(n,γ) measurement performed at the n_TOF CERN facility by means of C_6D_6 scintillation detectors. This experiment allowed us to provide capture cross section data for incident neutron energy between 1 eV and 480 keV.

1.7.1 Previous measurements and evaluations

As previously outlined, the importance of the radiative capture reaction on ^{238}U brought to a lot of experimental measurements of its cross section, mainly at the Oak Ridge Elec-

tron Linear Accelerator (ORELA) [65] and at the Geel Linear Accelerator (GELINA) [66] facilities. Here the most significative results are briefly described.

Linenberger, 1944 [67]. The ratio measurement of the radiative capture cross section of ^{238}U to the fission cross section of ^{235}U was performed at the Los Alamos National Laboratory. The activation method was used, detecting the beta-emission of ^{239}U deriving from the irradiation of a U_3O_8 sample by ^{6}Li(p,n) neutrons.

Fricke, 1970 [68]. Absolute neutron capture cross section for several isotopes were measured using the time-of-flight technique at the Gulf General Atomic Linear Accelerator in California. The measurements were performed at a 230 m flight-path in a neutron energy range from 1 keV to 1 MeV using a 2400 l liquid scintillator. The capture data are normalized with the saturated resonance technique, and the overall uncertainty in the cross section is about $10 - 15\%$ at all energies. The sample used was a high purity metal disk 5.5 at/b thick.

Panitkin, 1972 [69]. Measurement of the ^{238}U radiative capture cross section through the activation method at an electrostatic accelerator.

Poenitz, 1975 [70]. Ratio measurement of the capture cross section of ^{238}U to ^{197}Au were performed for neutron energy from 20 keV to 1.2 MeV at the Argonne National Laboratory in Illinois. The time of flight technique was used with a 2.5 m flight-path and the γ rays of the capture cascade were measured with a 1300 l liquid scintillator. The sample is composed of 2 or 4 high purity metallic disk of 0.02 cm thickness. The overall uncertainty was estimate to be $\sim 7\%$ at all energies.

Sowerby, 1994 [71]. To solve the initial inconsistencies both in the neutron resonance parameters and in the measured capture cross sections of ^{238}U a task force was organized by the Nuclear Energy Agency (NEA) of the Organization for Economic Cooperation and Development (OECD). The results obtained, published by M. G. Sowerby in 1994, led to a set of resonance parameters in the energy range thermal to 10 keV which were adopted in the most important nuclear data libraries. These parameters were based on previous evaluations by G. de Saussure in 1979 [72] and by M. Moxon and M. G. Sowerby in 1982 [73].

Derrien, 2005 [75]. More recently, analysis of various thermal reactor benchmarks showed that the values of k_{eff} were still underestimated [74], and therefore a new evaluation of ^{238}U resonance parameters have been performed by H. Derrien *et al.* in 2005. The results of this new evaluation have been adopted by the three main neutron cross section libraries ENDF/B-VII.1, JEFF-3.2 and JENDL-4.0. The experimental data sets used are listed in Table 1.5, and includes data not used in the Sowerby and

Table 1.5: Experimental database used in evaluation by H. Derrien *et al.* All the details of the measurements analysis can e found in Ref. [75] and reference therein. A description of the measurement types can be found in Chapter 4.

Energy range of analysis	**Reference**	**Measurement type**	**Sample thickness**	**Flight path length**
0.0253 eV	Poenitz et al. [76] ANL (1981)	Activation		
Thermal range	Corvi et al. [77] GELINA (1997)	Capture TOF	U and UO_2 0.001 at/b	8.7 m
6 eV to 38 keV	Meister et al. [78] GELINA (1997)	Transmission TOF	U and UO_2 0.000046 at/b 0.00010 at/b	26.5 m
6 eV to 10 keV	de Saussure et al. [79] ORELA (1973)	Capture TOF	2 samples 0.00283 at/b 0.00040 at/b	40.0 m
0.5 eV to 1 keV	Olsen et al. [80] ORELA (1977)	Transmission TOF	7 samples 0.0002 to 0.175 at/b	42.0 m
0.3 keV to 10 keV	Olsen et al. [81] ORELA (1979)	Transmission TOF	4 samples 0.0038 to 0.175 at/b	150.0 m
0.25 keV to 20 keV	Macklin et al. [82] ORELA (1988)	Capture TOF	2 samples 0.0031 at/b 0.0124 at/b	150.0 m
1 keV to 20 keV	Harvey et al. [83] ORELA (1988)	Transmission TOF	3 samples 0.0124 to 0.175 at/b	200.0 m

Moxon analysis. In particular, the use of Macklin capture measurement and Harvey transmission measurement extends the Resolved Resonance Region up to 20 keV.

The experimental transmission data of Harvey *et al.* were published in 1988 [83]. These measurements were performed at a 201.6 m flight-path in the neutron energy range 1 keV to 100 keV at room temperature for sample thicknesses of 0.1748, 0.0396, and 0.01235 at/barn. The nominal resolution was about 0.01 ns/m in the neutron energy range above 5 keV, and the analysis of these data allowed the resolved energy range to be extended up to 20 keV.

The high resolution measurement of Macklin *et al.* were measured for incident neutron energies between 1 keV and 100 keV at the ORELA 150 m flight-path, with a nominal resolution of about 0.03 ns/m comparable to Harvey transmission resolution, with

sample thicknesses of 0.0031 and 0.0124 at/b. The cross sections were normalized on the area of very small resonances with an accuracy of 6 to 8%.

In the evaluation the RRR (1 eV $< E_n >$ 20 keV) capture data were analyzed with the SAMMY code simultaneously with the transmission data. For both the de Saussure *et al.* and Macklin *et al.* capture data sets a correction factor was needed to agree with the transmission data.

Moxon, 2006 [84] In 2006 M. C. Moxon reviewed the data obtained in 1968 at Harwell, UK. The data have not been published but they are obtainable through the EXFOR database [52].

Ullmann, 2011 [86, 87]. Recently, a new measurement of ^{238}U(nγ) cross section in the energy range from 10 eV to 100 keV has been performed at the Los Alamos Neutron Science Center (LANSCE) facility with the DANCE calorimeter. These data have been released in march 2014, and therefore they are not yet available in the EXFOR database.

1.8 Summary

Nuclear reactions induced by neutrons are of fundamental importance for Nuclear Astrophysics, fundamental Nuclear Physics and Nuclear Technologies. In this chapter we focused the attention on this latter field, which is related to the energy-production via nuclear reactors.

An outlook on the global energy issue has been given, describing the situation of the present energy resources and giving different possible scenarios for the future. Among them, nuclear energy seems to be a necessary option to reduce greenhouse-gas emissions, with the further advantage of being considered a source of energy that improves energy security and adds stability to electricity costs.

Despite the tendency of OEDC countries to phase-out nuclear, enhanced after the Fukushima accident in Japan, the R&D of new nuclear reactors is ongoing, and is leading towards new generations of reactors intrinsically safe and with the capacity of burn radioactive waste. These new technologies have been briefly presented, paying particular attention to fast neutron reactors, Generation-IV reactors and accelerator driven systems. All these new concepts need accurate and precise nuclear data to be efficiently designed. To this purpose, the different nuclear data libraries have been presented, together with the experimental databases.

After this general introduction, the role of the ^{238}U(n,γ) reaction cross section has been investigated. It enters in the calculations of fast and thermal reactor parameters as

the effective multiplication factor or the reactivity coefficient, which govern the behaviour of the reactor core. Moreover, from the capture cross section on ^{238}U depends the density of Pu isotopes at the end of fuel cycles.

The importance of this cross section led to several measurements in literature, the most significtive of which have been presented. Nevertheless, inconsistencies are still present in the high energy region, while the Nuclear Energy Agency addressed as priority the reduction on the cross-section uncertainty down to 1-3% for the resolved resonance region. To this purpose, three independent measurements were scheduled within task 1.2 of the EU ANDES project at the GELINA (JRC-EU-IRMM laboratory, Belgium) and n_TOF (CERN, Switzerland) facilities.

The aim of this work is to analyze the data collected at n_TOF with C_6D_6 scintillators, with the result of providing the ^{238}U radiative capture cross section in an energy region between 1 eV and 480 keV.

Chapter 2
Neutron induced reactions

The occurrence of sharp resonance peaks in the reaction cross-sections observed at low incident neutron energies is one of the most visible and distinctive feature of neutron-nucleus reactions. Since the neutron is electrically neutral, it has no Coulomb barrier to overcome and can directly interact with the atomic nucleus even at very low kinetic energies. The cross section can therefore display variations of several orders of magnitude on an energy scale of few electron-volts. In this chapter the concept of neutron-nucleus cross sections will be introduced with particular attention paid to the case of the compound nucleus mechanism for nuclear reactions. The R-matrix theory and its practically useful approximations for the description of neutron-induced reactions will be discussed as well.

2.1 Nuclear reactions induced by neutrons

In typical nuclear reactions an accelerated projectile a impinges on a target X (usually at rest in the laboratory frame reference) generating the reaction products b and Y, and this is usually written with the compact notation X(a,b)Y. In neutron-induced reaction the projectile is the neutron itself (a=n), while the products depend on the reaction occurred (radiative capture ($b = \gamma$), elastic scattering ($b = n$), fission ($b = f$), ...). The reaction cross section σ is a physical quantity that represents a measurement of the relative probability for a reaction to occur. As an example, a detector placed to record particle b emitted in a direction (θ, ϕ) with respect tho the incident beam direction is considered. Let the current of incident particles be I_n neutrons per unit time, and let the target show to the incident beam N target nuclei per unit area. If the outgoing particle b are detected with a rate R_b the reaction cross section is

$$\sigma = \frac{R_b}{I_n N}, \tag{2.1}$$

and has the dimension of an area. Indeed, if neutrons were classical point particles and nuclei were solid spheres the cross section would simply be the target geometrical area seen by the incident neutrons. Actually, σ can be very much smaller or larger than this cross-sectional area, and can be though of as a quantity which has the dimension of an area and is proportional to the reaction probability.

Usually, more than one process occurs at a time when a neutron interacts with a given nuclide. These variety of nuclear reactions give rise to different cross-sections, referred to as reaction cross-sections, being the total cross-section defined as the sum of all:

$$\sigma_{\text{tot}} = \sigma_{\text{elastic scattering}} + \sigma_{\text{radiative capture}} + \sigma_{\text{fission}} + \dots \tag{2.2}$$

The neutron-capture processes can be divided in resonant and non-resonant interaction. The resonant capture reaction can be described as a series of two-body interactions [89] within Fermi's description of excitations of particle-hole configurations. The entrance channel is composed by a one-particle-zero-hole state (1p-0h with respect to the target nucleus), which is excited to the so-called doorway states (2p-1h or collective modes) and, through an extremely complex configuration of a many-particle-many-hole state, is led to a statistical equilibrium involving many nucleons and forming the compound nucleus (see Section 2.1.1). In non-resonant direct reactions, as the opposite reaction mechanism to compound nucleus reactions, the incident neutron interacts directly with one or few nucleons without perturbing the core. This process is also indicated as a 1p-0h interaction. The contribution of direct neutron reactions on heavy nuclei become important at neutron energies above 10 MeV, where the De Broglie wavelength of the neutron is of the order of the nucleons size.

Cross sections of neutron-induced reactions are completely different from one isotope to another because they are related to the nuclear structure of the nucleus. Furthermore, reaction cross-sections strongly differ each other and depend on the energy of the incident neutrons. For instance, neutron cross-sections on ^{238}U isotope for radiative capture, fission and elastic scattering are shown in Figure 2.1 on an energy scale spanning more than ten decades. From the figure, up to four energy regions can be identified attending to the shape of the neutron cross-sections:

Thermal and epithermal regions. Between 0.0253 eV (thermal point) and the first resonant structure in the eV region cross sections are found to be smooth and inversely proportional to the square root of the energy ($\sigma \sim 1/\sqrt{E} \sim 1/v$), that is proportional to the time that the incident neutrons spend in the vicinity of the target nucleus.

Resolved Resonance Region (RRR). Between a few eV and several keV, depending on the specific isotope, cross sections show large peak to valley variations. The structures that can be identified are called resonances, and in this energy range are well separated with a mean distance between them (called level distance D) large compared to their natural width Γ and the instrumental resolution Δ_R. The nature of these resonant structures is related to the existence of quasi-stationary levels of the compound nucleus which will be discussed in Section 2.1.1.

Unresolved Resonance Region (URR). With increasing neutron energy the resonances start to overlap, because although the resonant structures still exist ($D > \Gamma$), resonances can no longer be resolved due to the limited instrumental resolution ($D < \Delta_R$) with the result of a smooth cross section.

High energy region. As the neutron energy increases, many more reaction channels corresponding to threshold reactions open up. The distance between resonances is much smaller than their intrinsic widths ($D < \Gamma$) and resonant structures can not be observed any more.

All these neutron-induced reactions, whose importance was pointed out in the previous chapter, need to be investigated with high accuracy and precision. However, because of the extreme complexity of the nuclear system in the RRR, no nuclear model is accurate enough to calculate the cross sections from basic principles, and therefore experimental measurements are fundamental to complement theoretical predictions. Nevertheless,

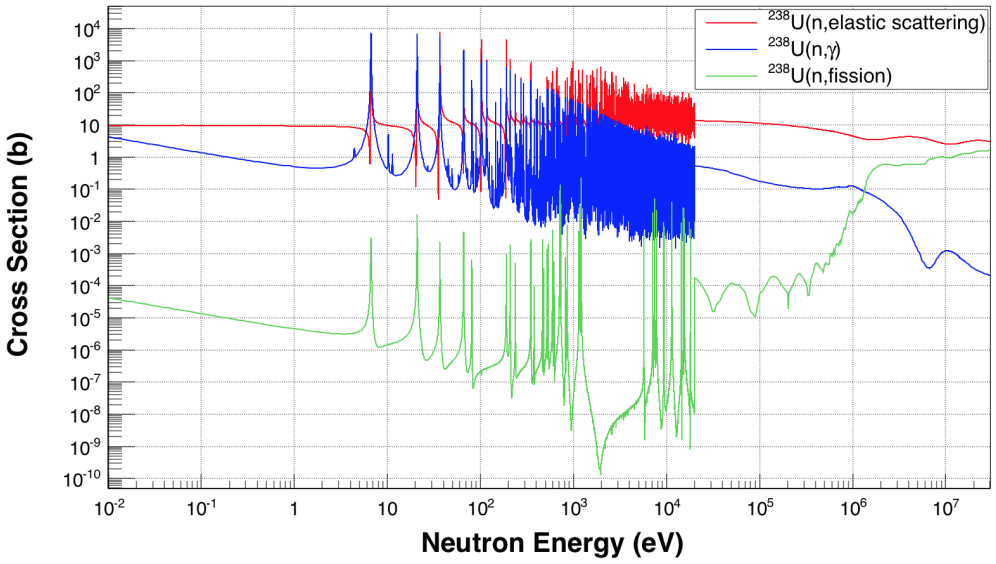

Fig. 2.1: Neutron capture, fission and elastic scattering cross sections on ^{238}U. Data from JEFF-3.2 library.

to establish a reliable database of reaction cross-sections, experimental data should be parametrized by theoretical reaction models. In particular, in order of increasing energy, the following theories and models are employed [90, 91]:

R-matrix theory. Used to describe thermal and RRR, its basic feature is the development of a complete set of formal states defined in a volume of nuclear size. The development is done by the imposition of some fixed boundary condition on the surface of this volume (parameters: level energies, level spin, partial widths) [90, 92–94]. See Section 2.2.

Level-statistical (Hauser-Feshbach) theory. In the URR the properties of the nuclear levels become apparent as values averaged over many resonances, and can be predicted by nuclear models (parameters: level density, strength functions and average partial widths, or the equivalent channel transmission coefficient) [95–97]. See Section 2.3.

Optical model. It is introduced to access neutron cross-sections at very high neutron energies, where cross-section measurements become extremely difficult (parameters: radius depth, diffuseness and deformation of the real and imaginary potential well). For more details see [22, 98].

These parametrizations are needed in view of the fact that in practical applications, like nuclear reactor calculations or stellar nucleosynthesis models, neutron cross-sections are used in terms of resonance parameters. The use of parameters instead of high-resolution data from measured cross-sections ensures consistency between partial and total cross-sections, permits inter- and extrapolation into region where no experimental data are available, and guarantees the consistency with physical limits[1]. Furthermore, experimental data are affected by resolution, Doppler broadening and multiple scattering (see Chapter 4) and the most effective way to calculate the correction factors is through a resonance parameter analysis of the data.

2.1.1 Compound nucleus

The compound nucleus mechanism was initially suggested by Niels Bohr [99] to explain the resonant structures observed in neutron-nucleus reactions. The basic idea of this mechanism is that a collision between a neutron and a nucleus will pass through the formation of a compound system of remarkable stability. Typical resonance widths Γ are

[1] A typical physical constraint is the unitary limits for the total cross-section in each reaction channel: $0 \leqslant \sigma_c \leqslant 4\pi\lambda\!\!\!^{-2}_c g_c$. The upper limit depends on the characteristics of the compound nucleus formed in the reaction, all the details will be presented in the further discussion.

measured to be in the order of the eV, with a corresponding life time of the compound nucleus in the order of $\tau = \hbar/\Gamma \simeq 10^{-15}$ s. Considering that the typical time interval used by a neutron to cross a nucleus without interacting is in the order of 10^{-21} s, it is clear that the duration of the encounter between the neutron and the nucleus is much larger than it would be considering direct interactions. Within this scenario, the excess energy brought by the incident neutron will be rapidly divided among all the nucleons with the result that for a subsequent time interval (i.e. the mean life of the compound nucleus) no single particle will possess sufficient kinetic energy to leave the nucleus. This complex configuration corresponds to a well defined nuclear state with defined energy, spin and parity. Symbolically, a nuclear reaction induced by neutron could be expressed as:

$$n + {}^{\mathrm{A}}_{\mathrm{Z}}\mathrm{X} \quad \longrightarrow \quad {}^{\mathrm{A+1}}_{\mathrm{Z}}\mathrm{X}^{*} \quad \longrightarrow \quad \mathrm{Y} + b. \tag{2.3}$$

Usually, $n + {}^{\mathrm{A}}_{\mathrm{Z}}\mathrm{X}$ is referred to as the entrance channel while $\mathrm{Y} + b$ as the decay or exit channel. As previously outlined, a reaction proceeding through the intermediate state of the compound nucleus could be considered as a two-step process: the formation and the subsequent decay of the compound nucleus itself. In Figure 2.2 a diagram of such a reaction is shown. A given compound nucleus ${}^{\mathrm{A+1}}_{\mathrm{Z}}\mathrm{X}^{*}$ has various possible way to decay, which must be considered as separate competing processes and independent of the way how the compound nucleus was formed, always respecting conservation of energy and angular momentum. The decay probability depends only on the total energy given to the system, which is the sum of the neutron binding energy S_n and the neutron kinetic energy in the center of mass frame system E_n^{cm}. Providing that the kinetic energy in the lab frame of the target nucleus is negligible comparing to the neutron one[2], the relationship $E_n^{cm} = [A/(A+1)]E_n$ holds, where E_n is the neutron kinetic energy in the lab frame. Therefore, the energy given to the compound nucleus can be expressed as:

$$E^{*} = S_n + \frac{A}{A+1}E_n. \tag{2.4}$$

After the formation of the highly excited state by an incident neutron, the compound nucleus can decay by emission of gamma radiation, referred to as radiative neutron-capture process, or by an emission of a neutron, which is elastic scattering. If the incident neutron kinetic energy is high enough threshold reactions are possible, like inelastic scattering in which a neutron is emitted with lower energy with respect to the elastic scattering, leaving the target nucleus in an excited state. Furthermore, if the excitation

[2] This assumption is always true for neutron energy in the lab frame higher than 10 eV. For lower energies, anyway, E_n is completely negligible with respect to the neutron binding energy S_n and so the approximation remains valid.

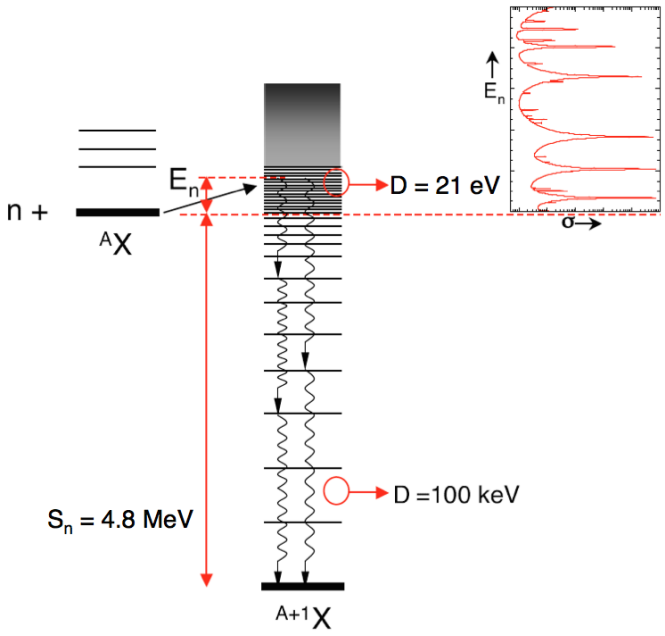

Fig. 2.2: Schematic view of formation and decay of a compound nucleus with ^{239}U values of level spacing and neutron separation energy. The resonances observed in the reaction cross section correspond to the excitation of the nuclear levels. Figure from [100].

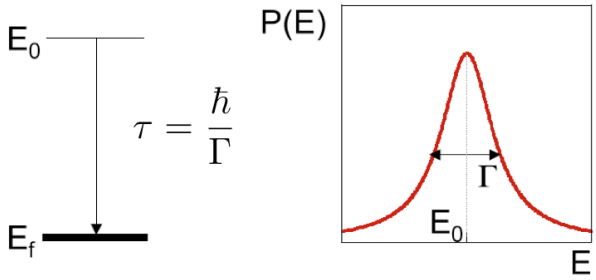

Fig. 2.3: Breit-Wigner shape of the energy profile (right) of a quantum state with a finite lifetime τ (left). Figure from [100].

energy E^* is higher than the fission threshold, fission as decay channel is energetically allowed.

All these reactions show resonant structures in the cross sections, with resonance energies corresponding to the excitation of the nuclear levels in the compound nucleus. The shape of a resonance is a peculiar characteristic of the reaction and is related to the involved widths. As previously pointed out, the total width of a given resonance Γ is correlated to its lifetime τ by the Heisenberg uncertainty principle $\Gamma\tau \sim \hbar$. This equivalence in the time and energy domain is illustrated in Figure 2.3.

Because each exit channel is to be considered independent according to Bohr's compound nucleus mechanism, to each exit channel would correspond one reaction width Γ_r (where r stands for the type of reaction occurred, i.e. γ for radiative capture, n for elastic scattering, f for fission, etc.). The total width Γ of the level is therefore the sum of the reaction widths of all the possible decay modes. The probability to decay via a channel r is given by:

$$P_r = P_{CN}\frac{\Gamma_r}{\Gamma}, \tag{2.5}$$

where P_{CN} corresponds to the probability of formation of the compound nucleus.

The shape of isolated resonances in reaction cross-sections is fitted with good approximation by the Breit-Wigner formula, obtained with a perturbative treatment of nuclear forces [101] adapted from the Weisskopf-Wigner theory of atomic reactions [102] as:

$$P(E) = \frac{\Gamma/2\pi}{(E - E_R)^2 + \Gamma^2/4}, \tag{2.6}$$

where E_R is the energy of the resonance. Problems arise when trying to interpret the values of the parameters obtained from such a fit, which can give absurd results because of the inexact bases of the formulation. In the Breit-Wigner approach the resonance shape, in fact, depends only on the condition that the reaction proceeds through an isolated, long-lived, intermediate state, ignoring the reasons behind the long lifetime. For this reason, it can be perfectly reproduced by a perturbative formula. However, it is worth noticing that in atomic reactions the excitation energy is concentrated on a single electron and the long lifetime is due to the weakness of the coupling of this e^- with the radiation field, justifying the perturbative approach and leading to correct results. On the contrary, in nuclear reaction the strength of the nuclear force leads to a sharing of the available energy among many nucleons, being the long lifetime related to the small probability of the energy to be concentrated in a mode such to open (i.e. made energetically allowed) a decay channel. The approach with a perturbative theory is therefore unsatisfactory and was removed with the introduction by Wigner and Eisenbund [92] of a rigorous theory of reaction, not dependent upon any particular physical picture or mathematical approximations: the R-matrix theory.

2.2 R-matrix formalism

An extensive and detailed overview of the R-matrix theory was given by Lane and Thomas [93] in 1958 and more recently by Fröhner [90]. The idea behind the R-matrix

formalism is to express the cross section in terms of the properties of the eigenstates of the compound nucleus such as energy, spin, parity and a set of reaction widths related to the different decay modes of the compound nucleus itself. To find these parameters the incoming and outgoing wave functions of the nuclear system (i.e. the wave functions before and after the reaction) must be matched to the internal wave function, which represents the nuclear system of two particle so close to form a compound nucleus. In this case the potential is extremely complicated, but it is always possible to expand the wave function in its eigenstate to extract the needed properties without providing any information on the forces inside the nucleus.

A basic assumption of the theory is the existence of some finite radial distance a_c, called interaction or channel radius, which can be considered as the separation between two geometrical regions in which the neutron-nucleus system is split. When the distance between the neutron and the nucleus is smaller than a_c all the nucleons interact with each other and form the compound nucleus. For distances higher than the interaction radius, on the contrary, the interaction between the neutron and the nucleus is negligible because of the short range of nuclear forces. To give a_c a physical significance, the idea is to choose it equal to the sum of the radii of the colliding particles. Considering a neutron-nucleus system the interaction radius can be written as [103]:

$$a_c \simeq 1.35\ A^{\frac{1}{3}} \quad \text{fm}, \tag{2.7}$$

where A is the mass number of the target nucleus.

In describing nuclear reactions it is customary to use the concept of channels, which in the framework of R-matrix theory will include only two particles. A channel is fully specified by

α, the partition of the compound system into reaction partners (as an example, ^{238}U + n or ^{239}U + γ are both involving the same compound nucleus),
$\mathbf{J}$, the total angular momentum in units of $\hbar$,
ℓ, the orbital angular momentum in units of $\hbar$,
$\mathbf{s}$, the channel spin in units of $\hbar$.

Being $\mathbf{I}$ the spin of the target nucleus and $\mathbf{i}$ the spin of the incident neutron in a neutron-nucleus reaction, the channel spin and the total angular momentum are given respectively by:

$$\mathbf{s} = \mathbf{I} + \mathbf{i} \qquad \text{i.e.} \qquad |I - i| \leqslant s \leqslant I + i, \tag{2.8}$$

$$\mathbf{J} = \boldsymbol{\ell} + \mathbf{I} + \mathbf{i} = \boldsymbol{\ell} + \mathbf{s} \qquad \text{i.e.} \qquad |\ell - s| \leqslant J \leqslant \ell + s, \tag{2.9}$$

where bold letters stand for vectors. Total energy, total angular momentum and parity (for all practical purposes) are conserved in nuclear reactions. Considering neutron-induced reactions, the resonance parity π is given by the product of the parity of the target nucleus $\pi_{\mathcal{N}}$ and the factor (-1)$^{\ell}$

$$\pi = (-1)^{\ell}\pi_{\mathcal{N}}. \tag{2.10}$$

The so-called statistical spin factor g_J is related to the probability of getting a total angular momentum J from the intrinsic spins of the colliding partners, i.e. the spins I of the target nucleus and i of the incident neutron:

$$g_J = \frac{2J+1}{(2i+1)(2I+1)}. \tag{2.11}$$

In other words, g_J is the ratio between the $2J+1$ substates of the compound system and the number of substates of the initial system consisting of a free neutron, with $2i+1=2$ substates (the spin of the neutron is 1/2), and the target nucleus, with $2I+1$ substates.

For a given ingoing wave in the channel c, leading to an outgoing wave in the channel c', the partial neutron cross-section $\sigma_{cc'}$ for total spin J may be expressed in terms of the collision matrix **U**:

$$\sigma_{cc'} = \pi\ \lambda\!\!\!^{-2}_{c}\ g_J\ |\delta_{cc'} - U_{cc'}|^2, \tag{2.12}$$

with

$$U_{cc'} = U^{J}_{\alpha\ell s,\alpha'\ell's'} \quad \text{and} \quad \delta_{cc'} = \delta_{\alpha\alpha'}\delta_{\ell\ell'}\delta_{ss'}. \tag{2.13}$$

The elements $U_{cc'}$ of the collision matrix describe the modification of the ℓ-th outgoing partial wave relative to the case without interaction, and the amplitude $|U_{cc'}|^2$ represents the probability of a transition from channel c to channel c'. The kinematic factor $\pi\lambda\!\!\!^{-2}$ relates the probability and the cross section (for further details see [22, 93]). The Kronecker symbol $\delta_{cc'}$ arises from the fact that incoming and outgoing particles could not be distinguished if $c = c'$.

In practice, channel to channel cross sections are not useful. The reason is that experimentally one can measure only the partitions α summing over all the values of ℓ and s, not the specific channel c. Therefore, what one is interested in is the cross section of the transition $\alpha \rightarrow \alpha'$ for the component of a given total angular momentum J. The reaction cross section is thus obtained by:

$$\sigma_{\alpha\alpha'}(j) = \pi\ \lambda\!\!\!^{-2}_{\alpha}\ g_J \sum_{\ell,\ell',s,s'} |\delta_{\ell\ell',ss'} - U_{\ell s,\ell's'}|^2. \tag{2.14}$$

Because of the Kronecker symbol, the expressions obtained for the cross section are thus simplest for total and most complex for elastic scattering cross-sections. Reaction cross-sections with $\alpha \neq \alpha'$ quadratically depends on the $U_{cc'}$:

$$\sigma_{\alpha\alpha'} = \pi \, \lambda\!\!\!^{-2}_{\alpha} \, g_J \sum_{\ell,\ell',s,s'} |U_{\ell s,\ell' s'}|^2. \tag{2.15}$$

Total cross sections can be derived from Eq. 2.14 by summing over all α'. From the unitarity of the collision matrix $\mathbf{U}$, $\sum_{c'} |U_{cc'}|^2 = 1$, follows that the total cross-section for an entrance channel c is a linear function of U_{cc}:

$$\sigma_c \equiv \sigma_\alpha(j) = 2\pi \, \lambda\!\!\!^{-2}_{\alpha} \, g_J \sum_{\ell,s} (1 - \mathrm{Re}\, U_{\ell s,\ell s}). \tag{2.16}$$

For elastic scattering cross-section, Eq. 2.14 leads to a tangled expression:

$$\sigma_{\alpha\alpha} = \pi \, \lambda\!\!\!^{-2}_{\alpha} \, g_J \sum_{\ell,s} \left(|1 - U_{\ell s,\ell s}|^2 + \sum_{\ell',s' \neq \ell,s} |U_{\ell s,\ell' s'}|^2 \right). \tag{2.17}$$

Therefore, it is more convenient to calculate $\sigma_{\alpha\alpha}$ as the difference between the total cross-section (given by Eq. 2.16) and the other partial cross-sections (given by Eq. 2.15), rather than directly from Eq. 2.14.

These equations are quite general to describe two body reaction cross-sections. The R-matrix theory allows to express the collision matrix $\mathbf{U}$ in terms of the matrix $\mathbf{R}$ as follows (see Lane and Thomas [93] for detailed calculations):

$$U_{cc'} = \mathrm{e}^{-i(\varphi_c + \varphi'_c)} \left\{ \delta_{cc'} + 2iP_c^{1/2} \left[(\mathbf{1} - \mathbf{RL^o})^{-1} \mathbf{R} \right]_{cc'} P_{c'}^{1/2} \right\}, \tag{2.18}$$

$$R_{cc'} = \sum_{\lambda} \frac{\gamma_{\lambda c} \, \gamma_{\lambda c'}}{E_\lambda - E}, \tag{2.19}$$

$$L^o_{cc'} \equiv L_{cc'} - B_{cc'} = (S_c + iP_c - B_c) \, \delta_{cc'}, \tag{2.20}$$

where bold letters stand for matrices.

Within the description via the R-matrix formalism three groups of physical quantities appears in Eq. 2.18 for the collision matrix:

Resonance parameters. The eigenvalues of the problem can be identified with the formal level energies E_λ, while the square of so-called reduced width amplitude $\gamma^2_{\lambda c}$ is related to the probability for decay (or formation) of the compound state λ via exit (or entrance) channels c. According to the R-matrix theory, the $\gamma_{\lambda c}$ are real, independent, and have normal distribution with zero mean [104]. All these parameters are folded in the R-matrix formulation as in Eq. 2.19, each level contributing as one sum term.

Hard-sphere phases φ_c and logarithmic derivatives L_c. They depend only on the known incoming and outgoing radial wave functions I_c and O_c at the channel radius a_c. The hard-sphere scattering $\varphi_c = \tan^{-1}\left(\text{Im } O_c(a_c)/\text{Re } O_c(a_c)\right)$ is associated to the elastic-scattering processes in which incoming neutrons are scattered by nucleus potential without forming any compound state (for further details see Lane and Thomas [93]).

Defining L_c as the logarithmic derivative of the outgoing wave function at the channel radius a_c, $L_{cc'} = \left[r_c\ \partial \ln O_c/\partial r_c\right]_{r_c=a_c}$, one can obtain the shift factor $S_c \equiv \text{Re } L_c$ and the penetrability $P_c \equiv \text{Im } L_c$. It is worth noticing that for neutron-induced reactions the penetrability is defined by the centrifugal-barrier penetrabilities only.

Boundary conditions B_c at the channel radius a_c. They define the eigenvalue problem with eigenvalues E_λ, and their choice is largely a matter of convenience. The channel radius is defined as in Eq. 2.7, while for neutral projectiles a good choice for the boundary condition is $B_c = -\ell$ [90]. In fact, being the hard-sphere phase factor and the logarithmic derivative for incident neutrons

$$L_0 = ik_c a_c = iP_0, \qquad L_\ell = -\ell - \frac{(k_c a_c)^2}{L_{\ell-1} - \ell}, \tag{2.21}$$

$$\varphi_0 = k_c a_c, \qquad \varphi_\ell = \varphi_{\ell-1} + \arg(\ell - L_{\ell-1}), \tag{2.22}$$

the choice of $B_c = -\ell$ simplifies the R-matrix expressions and eliminates rigorously the shift factor S_c for s waves ($\ell = 0$).

In practical analyses of neutron cross-sections, the collision matrix is usually expressed in terms of the level matrix $\mathbf{A}$:

$$U_{cc'} = \mathrm{e}^{-i(\varphi_c+\varphi'_c)}\left(\delta_{cc'} + i\sum_{\mu,\lambda}\Gamma^{1/2}_{\lambda c}\ A_{\lambda\mu}\ \Gamma^{1/2}_{\mu c'}\right), \tag{2.23}$$

$$\Gamma^{1/2}_{\lambda c} = \gamma_{\lambda c}\sqrt{2P_c}, \tag{2.24}$$

$$(\mathbf{A}^{-1})_{\lambda\mu} = (E_\lambda - E)\ \delta_{\lambda\mu} - \sum_c \gamma_{\lambda c}\ L^o_c\ \gamma_{\mu c}, \tag{2.25}$$

where Roman subscripts refer to reaction channel and Greek subscripts to compound-nucleus levels. The basic resonance parameters E_λ and $\gamma_{\lambda c}$ depend on the unknown nuclear interaction, and therefore can only be obtained as fit parameters adjustable to experimental cross-section data. For this reason, the cross-section formulae are usually written in terms of experimental observables such as the channel width $\Gamma_{\lambda c}$ rather than in terms of decay amplitudes. The channel width is related to the square of the reduced width amplitude (referred to as reduced level width) via the penetrability P_c, as can be inferred from Eq. 2.24:

$$\Gamma_{\lambda c} = 2\,\gamma_{\lambda c}^2 P_c. \tag{2.26}$$

Inverting this equation one can find the reduced width amplitude and therefore the R-matrix elements as in Eq. 2.19.

The practically important variants of the R-matrix formalism are the the Single and Multi Level Breit-Wigner formalism, usually referred to SLBW and MLBW approximations [101], and the Reich-Moore approximation [105].

2.2.1 Approximation to the R-matrix formalism

As previously introduced, resonance parameters could be only obtained through a comparison between experimental data and calculated cross sections. However, in the calculation of total and partial cross-sections the inversion of the level matrix **A** required by the R-matrix formalism is, if not impossible, extremely complicated. Therefore some assumptions are needed, each one corresponding to a different approximation of the theory, being the Reich-Moore the most and the SLBW the least accurate.

2.2.1.1 Single Level Breit-Wigner approximation

Before the R-matrix theory was introduced, the Breit-Wigner one-level resonance formula was used to parametrize cross-section data in the resonance region. Afterwards, the SLBW may be seen as an approximation of the R-matrix formalism if only one level is considered, that is with the condition that the level width Γ is much smaller than the level spacings D. Neglecting all levels apart from one, the inverse level matrix **A** from Eq. 2.25 can be expressed as [90]:

$$(\mathbf{A}^{-1})_{\lambda\mu} \rightarrow E_\lambda - E - \sum_c L_c^o\ \gamma_c^2 \equiv E_\lambda + \Delta - E - \frac{i\Gamma}{2}, \tag{2.27}$$

where the level shift Δ is the difference between the resonance energy E and level energy E_λ, $\Delta = E - E_\lambda$. The single level collision matrix **U** for s-wave ($\ell = 0$) neutrons may be therefore defined as follows:

$$U_{cc'} = \mathrm{e}^{-i(\varphi_c + \varphi_c')} \left(\delta_{cc'} + \frac{i\ \sqrt{\Gamma_c\ \Gamma_c'}}{E_\lambda + \Delta - E + i\Gamma/2} \right), \tag{2.28}$$

with $\Gamma = \sum\ \Gamma_c$ representing the total width. Considering nuclear reactions induced by neutrons ($c = n$) passing through the formation of a compound nucleus with an effective radius $R = a_c$, and choosing the boundary conditions in such a way that the level energy

is the same as the resonance energy (i.e. $\Delta = 0$), the collision matrix becomes

$$U_{nc'} = \mathrm{e}^{-ikR}\left(\delta_{cc'} + \frac{i\ \sqrt{\Gamma_n\ \Gamma'_c}}{E_\lambda - E + i\Gamma/2}\right)\mathrm{e}^{-i\varphi'_c}. \tag{2.29}$$

The resulting total and reaction cross-sections for a given spin J in the case of $kR = R/\lambda\!\!\!^{-} \ll 1$ are expressed as follows:

$$\sigma_n = 4\pi g_J R^2 + 4\pi\lambda\!\!\!^{-2}\frac{g_J\Gamma_n\Gamma}{\Gamma^2 + 4(E_\lambda - E)^2} - 16\pi\lambda\!\!\!^{-}R\frac{g_J\Gamma_n(E_\lambda - E))}{\Gamma^2 + 4(E_\lambda - E)^2}, \tag{2.30}$$

$$\sigma_{nc'} = 4\pi\lambda\!\!\!^{-2}\frac{g_J\Gamma_n\Gamma_{c'}}{\Gamma^2 + 4(E_\lambda - E)^2}. \tag{2.31}$$

As can be seen from Eq. 2.30 the total cross-section is a sum of three terms:

1. the potential or hard-sphere scattering cross-section $\sigma_P = 4\pi g_J R^2$, where R is the effective radius of the compound nucleus;
2. a symmetric resonance term;
3. an asymmetric term arising from interference between potential and resonance scattering.

Reaction cross-sections as expressed by Eq. 2.31 are intended for all the exit channels different from the elastic scattering, i.e. $c' \neq n$. As pointed out before, for elastic scattering the expression for the cross section becomes too complicated and it is convenient to use $\sigma_{nn} = \sigma_n - \sum_{c'}\sigma_{nc'}$.

It is suitable to make the energy dependence of the reduced neutron wavelength $\lambda\!\!\!^{-}$ and the neutron width Γ_n explicit. For the former, this dependence can be expressed through the value of the reduce neutron wavelength $\lambda\!\!\!^{-}$ at the resonance energy $\lambda\!\!\!^{-}_r = \lambda\!\!\!^{-}(E_\lambda)$ as:

$$\lambda\!\!\!^{-2} = \lambda\!\!\!^{-2}_r\frac{E_\lambda}{E}. \tag{2.32}$$

For the neutron channel widths Γ_n, instead, the energy dependence can be described through the definition of the reduced channel widths for a given value of the orbital angular momentum ℓ:

$$\Gamma^\ell_n(E_\lambda) = \frac{P_0(E_\lambda)}{P_\ell(E)}\frac{\Gamma_n(E)}{\sqrt{E}}, \tag{2.33}$$

expressing E in eV. The penetrabilities P_ℓ are given as the imaginary part of the logarithmic derivative defined in Eq. 2.21. For s-waves ($\ell = 0$) resonances this results in

$$\Gamma_n(E) = \Gamma^0_n(E_\lambda)\sqrt{E}. \tag{2.34}$$

This energy dependence, together with Eq. 2.31, explains the 1/v behaviour on the low energy side of s-wave resonance. The contribution from s-wave resonances to the radiative capture cross section is approximately given by the following equation:

$$\sigma_\gamma(E) = \frac{\pi\hbar^2}{2mE} g_J \sqrt{E}\ \frac{\Gamma_n^0 \Gamma_\gamma}{E_\lambda^2}, \tag{2.35}$$

providing that the resonance is located at an energy E_λ much larger than E and Γ, i.e. the cross section is calculated in an energy region distant, and below, the energy of the first resonances. At thermal neutron energy this expression gives

$$\sigma_\gamma(E = 0.0253\ eV) = 4.099 \times 10^6\ g_J \frac{\Gamma_n^0 \Gamma_\gamma}{E_\lambda^2} \tag{2.36}$$

By setting $E = E_\lambda$ in Eq. 2.30 and 2.31 the total and the radiative capture macroscopic peak cross section for a given spin J can be determined as:

$$\sigma_{\text{tot}}(E = E_\lambda) = 4\pi g_J R^2 + 4\pi \lambda\!\!\!^{-2} \frac{g_J \Gamma_n}{\Gamma}, \tag{2.37}$$

$$\sigma_\gamma(E = E_\lambda) = 4\pi \lambda\!\!\!^{-2} \frac{g_J \Gamma_n \Gamma_\gamma}{\Gamma^2}. \tag{2.38}$$

2.2.1.2 Multi-Level Breit-Wigner approximation

Several resonances can be taken into account as a sum of Breit-Wigner single level cross sections. This is the most simple treatment of cross sections of many resonances, and it neglects any possible interference between channels and levels. The Breit-Wigner multi-level (MLBW) approach sums over the levels in the collision matrix. In the inverse of the level matrix $\mathbf{A}$ all off-diagonal elements $(\mathbf{A}^{-1})_{\lambda\mu}$ are neglected, which means neglecting all interference terms between channels, but not between levels. Therefore the inverse level matrix could be expressed as:

$$(\mathbf{A}^{-1})_{\lambda\mu} = (E_\lambda - E + \Delta_\lambda - \frac{i\Gamma_\lambda}{2})\delta_{\lambda\mu}, \tag{2.39}$$

and the multi-level collision matrix $\mathbf{U}$ becomes:

$$U_{cc'} = \mathrm{e}^{-i(\phi_c + \phi_{c'})} \left(\delta_{cc'} + \sum_\lambda \frac{i\sqrt{\Gamma_{\lambda c}\Gamma_{\mu c'}}}{E_\lambda + \Delta_\lambda - E - i\Gamma_\lambda/2} \right). \tag{2.40}$$

2.2.1.3 Reich-Moore approximation

This approximation was developed by C. W. Reich and M. S. Moore in 1958 [105] to overcome the problems encountered in fitting the shape of some asymmetric fission cross section resonances with the single-level Breit-Wigner formula. Their formalism is valid in regions where the level widths are of the same order of magnitude as their spacing, in which the multi-level Breit-Wigner approximation does not yield to an accurate description of the cross sections.

The Reich-Moore approximation neglects the off-diagonal contribution of photon channel only in the level matrix $\mathbf{A}$. Photon channels are those having as exit channel the decay via γ rays emission, i.e. $c' = \gamma$. Providing that the number of photon channels is very large, each channel having a decay amplitude comparable to that of the others and random sign [104], the expectation value of the product of two decay amplitudes tends to cancel for $\lambda \neq \mu$, i.e. $\langle \gamma_{\lambda c}\gamma_{\mu c}\rangle = \gamma^2_{\lambda c}\delta_{\lambda\mu}$. Summing over all the photon channels ($c \in \gamma$) and neglecting all off-diagonal contributions from photon channels:

$$\sum_{c\in\gamma} \gamma_{\lambda c}\gamma_{\mu c} = \sum_{c\in\gamma} \gamma^2_{\lambda c}\delta_{\lambda\mu} = \Gamma_{\lambda\gamma}\delta_{\lambda\mu}. \tag{2.41}$$

The inverse level matrix could therefore be simplified as:

$$(\mathbf{A}^{-1})_{\lambda\mu} = (E_\lambda - E)\delta_{\lambda\mu} - \sum_{c\in\gamma} \gamma_{\lambda c}L^o_c\gamma_{\mu c} - \sum_{c\notin\gamma} \gamma_{\lambda c}L^o_c\gamma_{\mu c} \tag{2.42}$$

$$= (E_\lambda - E)\delta_{\lambda\mu} - \Gamma_{\lambda\gamma}L^o_\gamma\delta_{\lambda\mu} - \sum_{c\notin\gamma} \gamma_{\lambda c}L^o_c\gamma_{\mu c} \tag{2.43}$$

$$= \left(E_\lambda + \Delta_{\lambda\gamma} - E - \frac{i\Gamma_{\lambda\gamma}}{2}\right)\delta_{\lambda\mu} - \sum_{c\notin\gamma} \gamma_{\lambda c}L^o_c\gamma_{\mu c}, \tag{2.44}$$

with L^o defined as in Eq. 2.20. The level shift $\Delta_{\lambda\gamma}$ from photon channels is usually absorbed within the radiation width $\Gamma_{\lambda\gamma}$, which is taken as constant considering a constant E_λ.

Comparing this result to the general expression for the inverse level matrix as in Eq. 2.25 it is clear that the approximation belongs to an eigenvalue problem with E_λ replaced by $E_\lambda - i\Gamma_{\lambda\gamma}/2$, and yields to the Reich-Moore R-matrix

$$R_{cc'} = \sum_\lambda \frac{\gamma_{\lambda c}\gamma_{\lambda c'}}{E_\lambda - E - i\Gamma_{\lambda\gamma}/2} \qquad (c, c' \notin \gamma). \tag{2.45}$$

This could be considered as a reduced R-matrix in the sense that it is defined over the non-photonic channels only. The only traces of the eliminated photon channels are the total radiation widths $\Gamma_{\lambda\gamma}$ in the denominators.

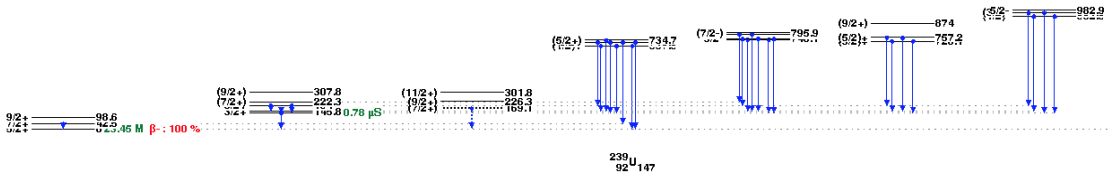

Fig. 2.4: Scheme of the first γ levels of ^{239}U.

The collision matrix is easily obtained inserting this reduced R-matrix in Eq. 2.18. It is worth noticing that the reduced R-matrices customarily used in neutron resonance analysis are of low rank, so that the inversion of $(\mathbf{1} - \mathbf{RL^o})$ is easy. The dimension for fissile target nuclei is usually 3×3 (1 elastic and 2 fission channels) while for non-fissile nuclei, for which the only energetically allowed process is the elastic scattering ($c' = n$), the 1-channel Reich-Moore expression is sufficient. It is important to recall that radiative capture ($c' = \gamma$) is always present but is averaged in the approximation and therefore not included in the collision matrix elements. In most cases R-functions

$$R_{nn} = \sum_{\lambda} \frac{\gamma^2}{E_\lambda - E - i\Gamma_{\lambda\gamma}/2}, \tag{2.46}$$

are used instead of R-matrices, so that for an s-wave the collision matrix is given by:

$$U_{nn} = \mathrm{e}^{-2i\varphi} \frac{1 + ika_n R_{nn}}{1 - ika_n R_{nn}}. \tag{2.47}$$

Elastic (σ_n) and total (σ_{tot}) cross sections are obtained from Eqs. 2.12 and 2.16. Radiative capture cross section σ_γ can be afterwards obtained as the difference

$$\sigma_\gamma = \sigma_{\mathrm{tot}} - \sigma_n. \tag{2.48}$$

The Reich-Moore approximation to the R-matrix theory is adopted in this work within the analysis of n+^{238}U in the resolved resonance region. The validity of the approximation is ensured by the extremely high number of photon levels present in the compound nucleus, namely ^{239}U. Only above the neutron separation energy 9269 non-bound states have been identified from experimental measurements of ^{238}U(d,p) and ^{238}U(n,γ) reaction, and from ^{239}Pu β-decay cross-sections. In Figure 2.4 a scheme of the first unbound levels is shown. A complete description of the adopted γ-ray levels for ^{239}U could be found in Refs. [106–108] and references therein. For the ^{238}U(n,γ) reaction at low energy 1 elastic scattering, 1 neutron capture and 2 fission channels are open. Therefore the number of channel in the R-matrix is three, the photon channel being excluded explicitly.

2.3 Average cross sections

The formalisms introduced so far to describe nuclear reactions induced by neutrons are valid for the low energy region. With the increase of incident neutron energy, the level widths become larger than the level spacing, and resonances start to overlap. The reasons for this behaviour lie in the statistical properties of resonance parameters, which will be described in Appendix A. In particular, the increase of the level density with increasing excitation energy results in a smaller level spacing, while the average neutron widths gets bigger with energy. Moreover, there are experimental effects that broaden resonance widths such as the Doppler broadening and the resolution of the apparatus.

The net result is that at a certain energy, different for each nucleus, cross sections cannot be described by measurable resonance parameters anymore, but can instead be characterized by average parameters, resulting in average cross-sections. The theory developed by Hauser and Feshbach [95] expresses resonance-averaged cross-sections for all reaction channels in terms of few physical meaningful average parameters, such as neutron and photon strength functions, defined as the ratio of the average reduced width over the level spacing, and level densities. These quantities are determined within a statistical description of the properties of resonance parameters that is called statistical model (see Appendix A).

The average total cross-section could be expressed, by analogy with Eq. 2.16, as:

$$\langle \sigma_c \rangle = 2\pi \lambda\!\!\!^{-2}_c \; g_J (1 - \mathrm{Re}\langle U_{cc} \rangle) \tag{2.49}$$

where the average collision matrix elements $\langle U_{cc} \rangle$ is derived from Eq. 2.18 with $c = c'$

$$\langle U_{cc} \rangle = \mathrm{e}^{-2i\varphi_c} \frac{1 - \langle R_{cc} \rangle L_c^{o*}}{1 - \langle R_{cc} \rangle L_c^{o}}, \tag{2.50}$$

and the channel average R-matrix elements can be written in the form

$$\langle R_{cc} \rangle = R_c^{\infty} + i\pi \; s_c. \tag{2.51}$$

The parameters can be defined as follows:

$\boldsymbol{\varphi_c}$: hard-sphere scattering phase shift;
$\mathbf{L_c^o}$: logarithmic derivative (see Eq. 2.20);
$\mathbf{R_c^\infty}$: distant-level parameter, which includes the effects of external levels;
$\mathbf{s_c}$: pole strength, defined in terms of the strength function S_c and the interaction radius a_c as $s_c = S_c \sqrt{E}/2k_c a_c$, being $k_c = 1/\lambda\!\!\!^{-}_c$.

The average parameters introduced in the formalism are the penetrabilities or transmission coefficients T_c, corresponding to the formation of the compound nucleus through the channel c:

$$T_c = 1 - |\langle U_{cc'} \rangle|^2 = \frac{4\pi P_c \ s_c}{|1 - \langle R_{cc} \rangle L_c^o|^2}. \tag{2.52}$$

For photon and fission channels, transmission coefficient for a given spin J are defined by:

$$T_\gamma = 2\pi \frac{\langle \Gamma_\gamma \rangle}{D_J}, \tag{2.53}$$

$$T_f = 2\pi \frac{\langle \Gamma_f \rangle}{D_J}, \tag{2.54}$$

being D_J the level spacing for levels with spin J.

For the partial widths a generalised Porter-Thomas distribution is assumed, i.e. a χ^2-distribution with ν degree of freedom:

$$p\left(\gamma_x^2 | \langle \gamma_x^2 \rangle\right) \mathrm{d}\gamma_x^2 = \frac{\mathrm{e}^{-y} y^{\nu/2}}{G\left(\frac{\nu}{2}\right)} \frac{\mathrm{d}y}{y}, \qquad 0 < y \equiv \frac{\nu}{2} \frac{\gamma_x^2}{\langle \gamma_x^2 \rangle} < \infty, \tag{2.55}$$

where $G\left(\frac{\nu}{2}\right)$ is a Gamma function and

$$\gamma_x^2 \equiv \sum_{c \in x} \gamma_c^2, \tag{2.56}$$

$$\langle \gamma_x^2 \rangle = \nu \langle \gamma_c^2 \rangle. \tag{2.57}$$

Therefore, the non-elastic reaction cross-sections can be expressed in terms of transmission coefficient T_c:

$$\langle \sigma_{ab} \rangle = \pi \lambda\!\!\!^{-2}_a g_J \frac{T_a T_b}{T} \int_0^\infty \mathrm{e}^{-iT_\gamma/T} \prod_{c \notin \gamma} \left(1 + \frac{2T_c}{\nu_c T} y\right)^{-\nu_c/2 - \delta_{ac} - \delta_{bc}} \mathrm{d}y, \tag{2.58}$$

where the quantities to the left of the integral sign are the Hauser-Feshbach expression, and the integrand is the Moldauer prescription [109] for the width-fluctuation correction factor. (A derivation of this expression, including the assumptions under which it is derived, is provided in Ref. [110]). Here a represents the incident channel and b the exit channel, while ν_c and T_c represent the number of degrees of freedom (multiplicity) and transmission coefficient, respectively, for a given channel c. Subscript γ refers to photon channels. The total transmission coefficient T is defined as the sum over all channels, $T = \sum_c T_c$.

Measured average cross sections are reported in the evaluated libraries as point-wise data. The importance of these data is that from them the level densities and strength functions can be derived, and they serve also as a validation for optical model cross section calculations.

2.4 Doppler broadening

In experiments at non-zero temperature the natural shape of a resonance does not correspond to the observed one, and to take into account the temperature effects the cross section needs to be convolved with Doppler broadening. The cause for Doppler broadening in nuclear reactions is the thermal motion of target nuclei in their atomic structure, with a distribution of the velocity depending on the material and its temperature. This movement of the target nucleus leads to a spread in the velocity in the center of mass frame of a neutron approaching the nucleus with a constant velocity in the lab frame.

There are several models that describe the mechanisms that give rise to the Doppler broadening [90], but for metallic samples the simple free gas model with a Maxwell-Boltzmann distribution of the target nuclei velocities constitutes a good approximation. Among these models, the non-zero temperature effect yields to a Gaussian broadening of the resonances with a standard deviation at a resonance energy E_0 given by:

$$\Delta\theta = \sqrt{\frac{4\ k_b T}{M/m} E_0} \tag{2.59}$$

where M/m is the ratio of the masses of the target nucleus and the incident particle, and $k_b T$ is the gas temperature in energy units (being k_b the Boltzmann constant).

For cubic crystals the temperature T has to be substituted by the effective temperature T_{eff} defined as [111]:

$$T_{\text{eff}} = \frac{3}{8} T_D \coth\left(\frac{3}{8}\frac{T_D}{T}\right). \tag{2.60}$$

Here T_D represent the Debye temperature, which is a measure of the binding force holding the atoms at their positions in the lattice, high for tightly bound and low for weakly bound atoms.

Doppler broadening is often larger than the natural width of a resonance. Therefore, for high precision cross-section measurements it can be advantageous to cool the target sample, so that T_{eff} approaches 3/8 T_D. In any case, to be compared with experimental data, the theoretical shape of a resonance must be modified by the Doppler broadening.

2.5 Analysis of the experimental data

From the analysis of the observable quantities in total or partial (n,x) cross-section measurements, the resonance parameters of the R-matrix formalism can be extracted. Each resonance can therefore be totally described by means of these parameters, which are for instance the potential scattering radius, the resonance energy E_0, the neutron Γ_n and radiation Γ_γ widths, and the spin and parity of the resonance (which determine the resonance statistical-factor). A full set of resonance parameters can be determined by a combination of different types of measurement [90, 112], such as:

Transmission measurements, in which the measured quantity is called transmission T and represents the fraction of an incident neutron beam crossing a given sample that does not interact with the sample itself (see Section 4.1). This type of measurement allows to determine the total cross-section and, through a comparison with the R-matrix theory, the parameters

$$E_0,\ \Gamma_n,\ \Gamma,\ g \qquad \text{for } \ell = 0, \tag{2.61}$$

$$E_0,\ g\Gamma_n \qquad \text{for } \ell \geqslant 0. \tag{2.62}$$

Capture measurements, in which neutrons are captured in the sample with the subsequent emission of γ-rays, which are detected to determine the capture yield Y_c, i.e. the fraction of incident neutrons that undergoes an interaction with the sample itself (see Section 4.2). From this measurement one can obtain

$$E_0,\ \Gamma_\gamma \qquad \text{if } \Gamma_n \text{ and } g \text{ are known and } \Gamma_n \gg \Gamma_\gamma, \tag{2.63}$$

$$E_0,\ \Gamma_n \qquad \text{if } g \text{ is known and } \Gamma_\gamma \gg \Gamma_n. \tag{2.64}$$

Self-indication measurements, which combine transmission and capture measurements: the neutrons pass trough a filter and then reach the capture detection setup containing the same material of the filter as a sample.

To extract the resonance parameters from the experimental data it is very important to understand the relation between the experimental observables and the resonance parameters and, in the long run, to identify a combination of complementary measurements that should be performed.

2.5.1 Resonance Area Analysis and capture kernel

The idea at the basis of the area analysis method is that the area of a given resonance, observed in experimental cross-sections as a function of energy, represents the number of events coming from the observed process and, therefore, is independent of the experimental resolution. Consequently, in the case of isolated resonances the simplest method to extract resonance parameters from measured data is the area analysis [113], calculating the resonance area from the experimental observables (e.g. capture yield Y_γ and transmission coefficient T) as the number of counts times the energy bin width. Considering a well isolated resonance, the transmission ($A_{\rm tot}$), capture (A_γ) and elastic scattering (A_n) areas are expressed as:

$$A_{\rm tot} = \int \left(1 - \mathrm{e}^{-n\sigma_{\rm tot}}\right) \mathrm{d}E, \tag{2.65}$$

$$A_\gamma = \int \left(1 - \mathrm{e}^{-n\sigma_{\rm tot}}\right) \frac{\sigma_\gamma}{\sigma_{\rm tot}} \mathrm{d}E, \tag{2.66}$$

$$A_n = \int \left(1 - \mathrm{e}^{-n\sigma_{\rm tot}}\right) \frac{\sigma_n}{\sigma_{\rm tot}} \mathrm{d}E, \tag{2.67}$$

where the integration are performed over the energy range of the resonance. $\sigma_{\rm tot}$, σ_γ and σ_n indicates the total, capture and elastic scattering cross sections respectively, and the sample thickness n is expressed in atoms per unit area.

To solve the integrals the Doppler broadening effects are neglected, and only the resonant part of the Single Level Breit-Wigner (SLBW) formalism is considered for the parametrization of the total and capture cross-sections. Under these conditions, the following asymptotic relations in the limit of a very thin ($n\sigma_{\rm tot} \ll 1$) and very thick ($n\sigma_{\rm tot} \gg 1$) sample can be found:

$$A_{\rm tot}(\text{thin}) = \frac{1}{2}\pi n\sigma_0\Gamma = 2n\pi^2 \lambda\!\!\!^{-2}_0 g_J \Gamma_n, \tag{2.68}$$

$$A_{\rm tot}(\text{thick}) = \sqrt{\pi n\sigma_0}\Gamma = 2\pi \lambda\!\!\!^{-}_0 \sqrt{n g_J \Gamma_n \Gamma}, \tag{2.69}$$

$$A_\gamma(\text{thin}) = \frac{1}{2}\pi n\sigma_0\Gamma_\gamma = 2n\pi^2 \lambda\!\!\!^{-2}_0 g_J \frac{\Gamma_n\Gamma_\gamma}{\Gamma}, \tag{2.70}$$

$$A_n(\text{thin}) = \frac{1}{2}\pi n\sigma_0\Gamma_n = 2n\pi^2 \lambda\!\!\!^{-2}_0 g_J \frac{\Gamma_n\Gamma_n}{\Gamma}. \tag{2.71}$$

Here $\sigma_0 = 4\pi \lambda\!\!\!^{-2}_0 g_J \Gamma_n/\Gamma$ is the total peak cross-section of the resonance, as defined in Eq. 2.37 without the potential scattering term, and $\lambda\!\!\!^{-}_0$ is the reduced neutron wavelength

at the resonance energy E_0. The immediacy of this analysis method lays on the fact that, for well isolated resonances, the left part of Eqs. 2.68 to 2.71 can be simply calculated as the area subtended by the experimental data.

It is important to notice that the capture area A_γ is connected to the quantity

$$\kappa = g_J \frac{\Gamma_\gamma \Gamma_n}{\Gamma_\gamma + \Gamma_n} \approx \begin{cases} g_J \Gamma_n \text{ when } \Gamma_\gamma \gg \Gamma_n \\ g_J \Gamma_\gamma \text{ when } \Gamma_\gamma \ll \Gamma_n \end{cases} \tag{2.72}$$

by the relationship $A_\gamma = 2n\pi^2 \lambda\!\!\!^{-2}_0 \kappa$. κ is called capture kernel and is the quantity usually used to characterize the resonances in capture experiments.

As can be inferred from these relations, the reaction cross-section data resulting from elastic scattering, capture and transmission measurements are complementary for the area analysis method, and at least two among them are needed to determine the partial widths.

In addition, combining capture and transmission measurements it is possible to verify if the correct spin has been assigned to a given resonance. In fact, nuclear data libraries classify resonances depending on the corresponding angular momentum ℓ. As an example, spin-parity and statistical spin factor values for ^{238}U+n reactions are listed in Table 2.1. A theoretical kernel-function $\kappa(\Gamma_n)$ can be therefore obtained by fixing the radiative partial width Γ_γ to the mean of the Gaussian which best fits the experimental values (for ^{238}U, $\Gamma_\gamma = 23$ meV) and using different values for the statistical spin factor g_J.

To compare theoretical functions to experimental kernels, we plotted resonance kernels as a function of elastic partial width Γ_n in the left panel of Figure 2.5. Values are taken from ENDF/B-VII.1 evaluation [114]. From the figure it is visible that a group of resonances identified as p-waves follows the $g = 3$ kernel-function, possible only for d-waves ($\ell = 2$). The presence of these d-waves is confirmed also by the behaviour of $\Gamma_n/\sqrt{E_R}$ as a function of the resonance energy, which is shown in the right panel of Figure 2.5. From the plot three different groups of resonances can be clearly distinguished, corresponding to three different angular momenta.

Table 2.1: Spin-parity and statistical spin factor values for ^{238}U+n reactions.

ℓ	s	J^π	g_J	Wave
0	$\frac{1}{2}$	$\pm\frac{1}{2}^+$	1	s
1	$\frac{1}{2}$	$\pm\frac{1}{2}^-$, $\pm\frac{3}{2}^-$	1, 2	p
2	$\frac{1}{2}$	$\pm\frac{1}{2}^+$, $\pm\frac{3}{2}^+$, $\pm\frac{5}{2}^+$	1, 2, 3	d

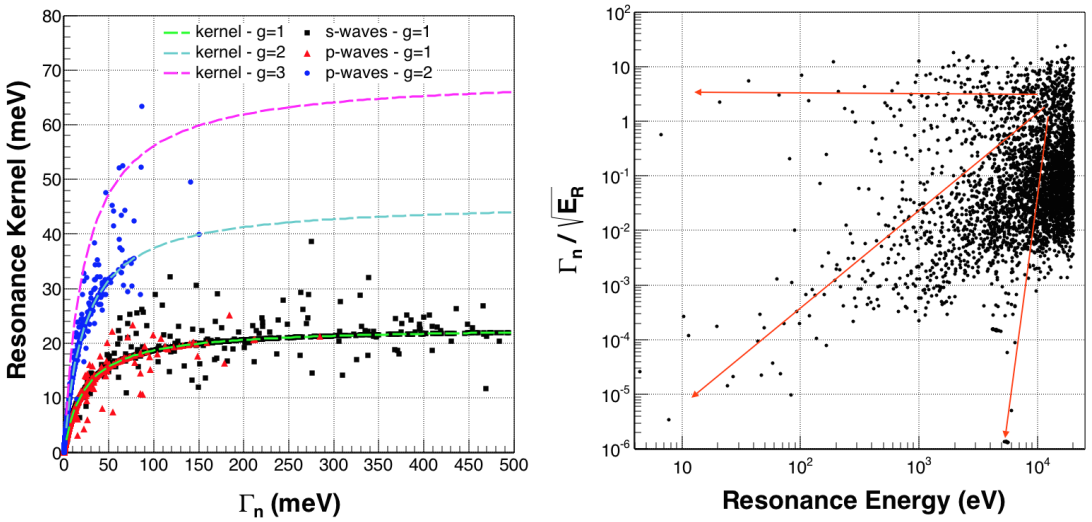

Fig. 2.5: Check on the correct assignment of resonance spins in ENDF/B-VII.1 file. The resonance parameters have been used to calculate experimental kernels for s-waves ($g = 1$: black points) and p-waves ($g = 1$: red points, $g = 2$: blue points). Dotted lines indicated theoretical kernel functions for $g = 1$ (green), $g = 2$ cyan and $g = 3$ magenta. It is visible that a group of resonances identified as p-waves follows the $g = 3$ distribution, possible only for d-waves.

The identified resonances with an incorrect spin assignment are in the energy range $10 < E_R < 20$ keV, where only the measurement by Harvey [83] is available. In this work the Resolved Resonance Region extends only up to incident neutron energy of 3 keV, and therefore can not help to clarify the issue. However, a revision of the resonance-spin assignment in evaluated files is strongly suggested from this check.

2.5.2 Resonance Shape Analysis (RSA)

Despite the simple principles of the area analysis method, several difficulties arise once it is applied to extract the parameters from experimental data. In fact, experimental observables can be inserted in Eqs. 2.68 to 2.71 only after corrections for experimental effects such as Doppler broadening, energy resolution of the spectrometer and, in the case of capture measurement, multiple scattering. Therefore, when experimental measurements have suitable energy resolution and statistics it is preferable to include these effects by performing a full Resonance Shape Analysis (RSA). With this method resonance parameters (E_0, J, Γ_n, Γ_γ, ...) are extracted through a fit of the resonance shape starting from experimental transmission and reaction yields. Applying the resonance

shape analysis, the scattering radius can also be determined from the resonances, and interferences between multiple resonances can be taken into account.

Providing a good knowledge of the resolution of the spectrometer, RSA is superior to area analysis method since it utilizes all the information containing in the data. In an ideal case without any additional broadening related to Doppler effects and experimental resolution, it is possible to determine from only one data-set the resonance energy, the total resonance width and the peak cross-section. Adding to these quantities the knowledge of the resonance spin all resonance parameters can be extracted. However, the presence of additional broadening effects in real experimental measurements do not allow an accurate determination of the total width. For this reason, even with RSA additional complementary data, such as the ones from transmission measurements, are required for the determination of the complete set of resonance parameters.

A further difficulty arises from the approximation to the R-matrix theory used for the resonance shape analysis. Even exploiting the most accurate Reich-Moore approximation, the R-function used (expressed in Eq. 2.46) can not describe completely the experimental data. The complete R-matrix theory shows in fact that the cross section in a limited energy range depends not only on the internal levels in that range, but also on the external levels below and above. Within the approximations, however, levels of the compound nucleus below the neutron threshold (bound state at $E_n < 0$) are omitted. Although they are unobservable and therefore unknown, problems arise in practical resonance fitting if they are not introduced in the R-matrix formalism used. Since the number of resonances per isotope is very large, a statistical treatment of the more distant levels seems to be appropriate if a cross section is to be calculated at a given energy [90, 115]. Parameters of the negative resonances are adjusted in order to reproduce both the energy dependence of total and capture cross-section data at thermal energy. In order to include the contribution of external levels the Reich-Moore R-matrix is split into a sum over the unknown external levels j and a sum over the known internal ones i:

$$R_{nn} = \sum_{i=0}^{i_{int}} \frac{\gamma_{i\ n}^2}{E_i - E - 1\Gamma_{i\gamma}/2} + \sum_{j=0}^{j_{ext}} \frac{\gamma_{j\ n}^2}{E_j - E - 1\Gamma_{j\gamma}/2}. \tag{2.73}$$

The second term of the obtained R-matrix is the distant level parameter R_n^∞, previously seen in Eq. 2.51. It is practically defined through the effective potential scattering length R' for s-waves channel [116] as:

$$R' = a_n(1 - R_n^\infty). \tag{2.74}$$

Even though the effective radius R' is theoretically connected to the potential scattering cross section ($\sigma_P = 4\pi R'$) and the scattering cross section at low energies, in the R-matrix shape analysis programs it is determined from the interference between the resonance part and the potential scattering for s-wave resonances.

2.6 Summary

Nuclear reactions induced by neutrons have been here described in the mechanism of the compound nucleus, and different energy regions have been identified where the behaviour of the cross section is significantly different. The two energy region of interest in this work are the Resolved resonance Region (RRR), between few eV and several keV, where resonance can be clearly identified because the level distance is large compared to resonance widths, and the Unresolved Resonance Region (URR), at higher energies, where the resonance structures overlap and the cross section needs to be averaged.

Neutron-nucleus reactions could be quantified in terms of the R-matrix theory, a rigorous formalism of nuclear reactions that expresses the cross section as a function of the eigenstates of the compound nucleus such as energy, spin, parity and reaction widths. For practical applications, assumptions are needed to simplify the solutions of R-matrix theory equations, each one leading to a different approximation of the theory.

Different methods to analyze experimental data have been described, namely the area analysis and the resonance shape analysis (RSA) methods. From the former a significative quantity, called resonance kernel, can be identified. A practical application of the resonance area analysis is presented to determine the correctness of ^{238}U resonance-spin assignment in ENDF/B-VII evaluation, from which shows up that for high-energy resonances a revision of the spin assignment is strongly suggested.

Moreover, it is shown that exploiting the RSA a data analysis in terms of the Reich-Moore approximation of R-matrix formalism gives precise and reliable results for n+heavy-nuclei reactions. Therefore, in these cases (e.g. in the case of ^{238}U(n,γ) reaction) cross-sections of reactions induced by neutrons can be investigated both in the resolved and unresolved energy regions. Particularly, physical parameters (resonance energy, reaction and total resonance widths, strength functions, level densities, ...) can be extracted from experimental data to calculate total and reaction cross-sections, both point wise and through extrapolation and interpolation.

Chapter 3
The n_TOF facility

To study the resonant structures of neutron-induced reaction cross-sections, neutron spectroscopic measurements are required, which determine with high accuracy the energy of the neutron interacting with the material under study. All the different methods exploitable require a neutron source, which can be of completely different nature and characterizes the different facilities. Moreover, cross sections can be measured either at specific energies using mono-energetic neutron beams, or in the form of point-wise cross sections exploiting pulsed beams, or as average values using a continuous energy neutron beam. Among all the experimental techniques, point-wise cross-section measurements, in the widest possible energy range, give the most complete experimental data-sets. These measurements can be performed only by means of the time of flight (TOF) method. In this chapter the different experimental conditions adopted in time-of-flight facilities will be described. Among them we will focus on the n_TOF facility at CERN, the characteristics of which make it particularly suited for high accuracy and precision measurements.

3.1 Experimental facilities for neutron beam production

The different experimental time-of-flight facilities can be classified depending on the neutron production mechanism exploited and the length of their flight-path [117]. The former one determines the characteristics of the neutron beam, such as the energy distribution, the integrated and instantaneous neutron flux and the in-beam background. The latter one determines the energy resolution of the spectrometer, which is an extremely important parameter for a reliable data analysis and depends also on parameters related to the neutron source, as will be described in Section 3.2.1.

Neutron cross-section measurements can be carried out at a continuous source using a chopper [118] or at an accelerator-driven white neutron source operating in pulsed mode.

Table 3.1: Characteristics of the time-of-flight facilities used for cross-section measurements.

Facility	Ref.	Type	Particle Energy (MeV)	Target	Pulse width (ns)	Frequency (Hz)	Flight path length (m)
GELINA (EC-JRC-IRMM, Belgium)	[66]	e^-	80 - 140	U	1	40 - 800	10 - 400
ORELA (ORNL, USA)	[65]	e^-	140	Ta	2 - 30	1 - 1000	10 - 200
RPI (Troy, NY, USA)	[119]	e^-	60	Ta	7 - 5000	500	10 - 250
J-PARC/MLF-ANNRI (Tokai, Japan)	[120]	p	800	W	135	20	7 - 60
LANSCE - Lujan center (LANL, USA)	[121]	p	800	W	135	20	7 - 60
LANSCE - WNR (LANL, USA)	[121]	p	800	W	0.2	13.9×10^3	8 - 90
n_TOF (CERN, Switzerland)	[122,123]	p	20×10^3	Pb	6	0.4	20 - 185

Choppers are mostly used in measurements at a reactor and are limited to the low energy region. Nevertheless, their role is fundamental to produce consistent cross sections in the thermal energy ragion, necessary to adjust the contribution of bound states ($E < 0$). Moreover, thanks to the high neutron flux of nuclear reactors, a very small amount of material (in the order of micrograms or less) is sufficient, letting this method be suitable to measure cross sections of highly radioactive materials.

For high-resolution neutron spectroscopy, a neutron source covering a broad energy range is mostly used. To select incident neutron energies the time of flight technique is needed (described in Section 3.2), which could only be applied with pulsed neutron sources. They can be realized at electron- and proton-based accelerators, and the originally fast neutron spectrum produced could be moderated by means of hydrogen-rich materials in order to increase the amount of low energy neutrons. The result is that such machines could provide a neutron energy spectrum from tens of meV up to GeV.

In electron-based accelerators, high-energy electrons produce Bremsstrahlung radiation in a target made out of material with a high mass number like Ta, Hg or U. Neutrons are produced via photonuclear (γ,n) and (γ,2n) and photofission (γ,f) reactions. On the other hand, high-energy proton accelerators produce neutrons as secondary particles in spallation reactions, with a very high yield of neutrons per proton striking a target of heavy nuclei. In Table 3.1 the most significative TOF facilities are listed together with their main characteristics. It is worth noticing that some facilities have several measurement stations at different flight-paths so that experiments can be performed in parallel.

Another possible neutron source is constituted of charged-particle reactions, such as ^{7}Li(p,n)^{7}Be or ^{9}Be(α,n)^{12}C, combined with a pulsed charged-particle source. In this way beams of either nearly monochromatic neutrons or with a broader energy spectrum are

produced. This method results in cross-section measurements at specific neutron energies or averaged over the customized incident neutron spectrum, providing accurate total and capture cross-section data in the unresolved resonance region.

3.2 The time of flight method

As outlined before, in order to perform neutron time-of-flight measurements a pulsed neutron source is required. In a relatively short time, corresponding to the pulse width, neutrons with a broad energy spectrum are created. At a given distance, ranging from a few meters to several hundred meters for high-resolution experiments, a target is placed in the neutron beam and the detection setups are implemented.

The TOF technique can be applied to determine the velocity v of a neutron from the time t it needs to travel the distance L. Experimentally, this time interval is derived from the difference between a stop and a start signal, T_s and T_0 respectively. The stop signal T_s is determined from the detection of the reaction products emitted in the neutron-induced reaction. The start signal T_0 is provided by beam monitors. For instance, at the n_TOF facility T_0 is given when the proton beam pass through a monitor placed just in front of the entrance of the production target, composed by a lead cylinder placed in a moderation pool. This signal represents the time the neutron is produced. The observed time of flight t_m becomes

$$t_m = T_s - (T_0 - t_o), \tag{3.1}$$

where t_o is a time offset mostly due to differences in cable lengths. This offset can be deduced from a measurement of the so-called γ-flash, constituted of the γ rays originated in the neutron-producing target and travelling along the beam. These γ rays are of very high energy and produce a large signal in the detectors, usually saturating them as can be seen in Figure 3.1.

The time of flight t_m as defined in Eq. 3.1 is related to the velocity v the neutron has at the moment it leaves the target and enters the beam pipe by:

$$v = \frac{L}{t} = \frac{L}{t_m - (t_t + t_d)}. \tag{3.2}$$

Here L is the distance between the outer surface of the neutron-producing target and the front face of the sample, and it is called flight-path. The additional term appearing in the denominator is related to the uncertainties in determining T_0 and T_s: t_t is the time difference between the moment the neutron leaves the target and the moment it is

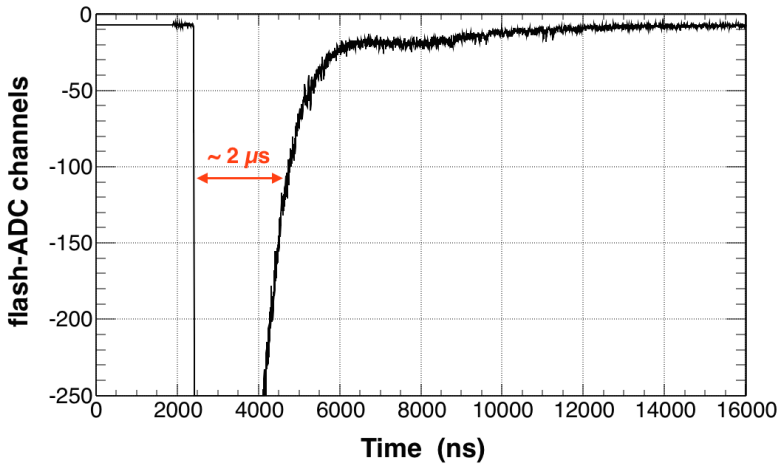

Fig. 3.1: Signal induced by the γ-flash in one of the scintillator detectors used for capture cross-section measurements at the n_TOF facility. The signals saturate the detector blinding it for about 2 μs, meaning that the highest energy reachable is $E_n \sim 1$ MeV.

created in it, while t_d is the difference between the time of detection and the moment the neutron enters the sample. The kinetic energy E_n of the neutron can be expressed relativistically as:

$$E_n = mc^2 (\gamma - 1), \tag{3.3}$$

where m is the rest mass of the neutron, γ represents the Lorentz factor

$$\gamma = \frac{1}{\sqrt{1 - (v/c)^2}}, \tag{3.4}$$

and c is the speed of light. The first term of the series expansion gives the classical expression for the neutron kinetic energy:

$$E_n = \frac{1}{2} m v^2 = \left(\alpha \frac{L}{t} \right)^2. \tag{3.5}$$

Taking the value of the speed of light $c = 2.99792458 \times 10^8$ m/s and $m = 939.6$ MeV/c^2 for the neutron mass, it results $\alpha \approx 722.983$ when L is expressed in centimeters, t in nanoseconds and E_n in eV [124].

From Eq. 3.3 the expression for the energy resolution ΔE of a TOF spectrometer can be given as a function of the velocity resolution Δv as:

$$\frac{\Delta E_n}{E_n} = (\gamma + 1)\, \gamma \frac{\Delta v}{v}. \tag{3.6}$$

In the case of low neutron energy, where $\gamma \approx 1$, the relative energy resolution is twice the relative velocity resolution. The latter can be obtained as a combination of the resolution broadening due to the TOF t and the flight-path L represented by Δt and ΔL, respectively:

$$\frac{\Delta v}{v} = \sqrt{\left(\frac{\Delta t}{t}\right)^2 + \left(\frac{\Delta L}{L}\right)^2}. \tag{3.7}$$

The flight-path L can be determined by metric measurements with an uncertainty of less than 1 mm ($\Delta L < 1$ mm at full width half maximum (FWHM)). The TOF t corresponding to the distance L depends on t_m, t_t and t_d as outlined in Eq. 3.2. As can be seen from Eq. 3.7 the longer the flight-path, the better is the accuracy on the measured velocity, and therefore the energy resolution of the spectrometer. A long flight-path, however, leads to a drop in the neutron flux that goes as L^2. For this reason the baselines of the facilities are always a compromise between a good resolution and a high neutron flux, depending on the requirements. More details on the n_TOF spectrometer are given in Section 3.3.

3.2.1 Resolution function of a Time Of Flight spectrometer

The resolution function of a TOF spectrometer $R(t, E_n)$ is the probability that a neutron with energy E_n is detected with a corresponding time of flight t. It can be considered as a convolution of different components:

- Finite duration of the accelerator burst of primary particles as e^- or protons (which affects T_0).
- Time resolution of the detector and electronics (which affects T_s).
- Neutron transport in the neutron source (t_t).
- Neutron transport in the sample (t_d).

The first two components can both be represented by a simple analytical function, like a normal distribution with a width independent of neutron energy.

In case of a moderated neutron beam, the broadening in time is dominated by the neutron transport in the target-moderator assembly, i.e. the time component t_t. Consequently, resolution functions will strongly depend on the physics properties of the target-moderator assembly (dimensions and materials). The distribution of this component can be deduced from Monte Carlo simulations or approximated by analytical expressions. Top panel of Figure 3.2 shows resolution functions due to the neutron transport in the

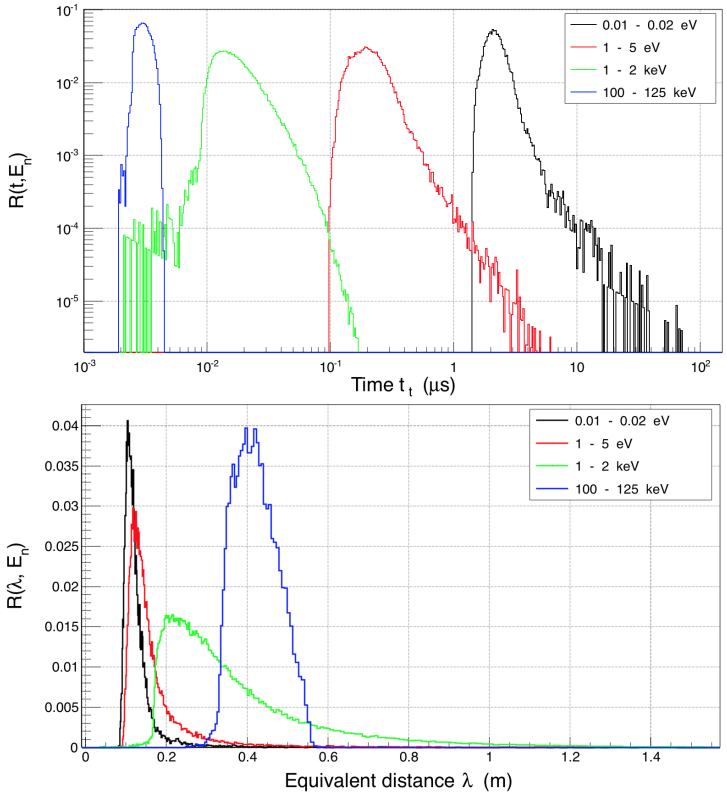

Fig. 3.2: Top panel: Probability distribution of the time t_t that a neutron spends travelling in the target-moderator system of n_TOF. Bottom panel: Probability distribution of the equivalent distance λ that a neutron travels in the target-moderator assembly of n_TOF. Both distributions are obtained from FLUKA simulations of the n_TOF facility and are given in arbitrary units.

target-moderator assembly for the n_TOF facility obtained from FLUKA simulations. As can be seen, these distributions strongly depend on the neutron energy. Response functions of a TOF spectrometer can be more conveniently represented by introducing an equivalent distance λ travelled by the neutron in the target-moderator assembly. The equivalent distance is defined as $\lambda = vt_t$, where v is the velocity of the neutron at the moment it escapes from the target-moderator assembly. This transformation of variables results in probability distributions of λ which are less dependent on the neutron energy, as shown in the bottom panel of Figure 3.2. Together with MC simulations, several examples of analytical expressions reflecting the neutron transport in the target-moderator system have been proposed [125,126]. They all have two common features: an exponential decay accounting for the primary neutron production in the target and a χ^2 distribution describing the probability distribution of the equivalent distance.

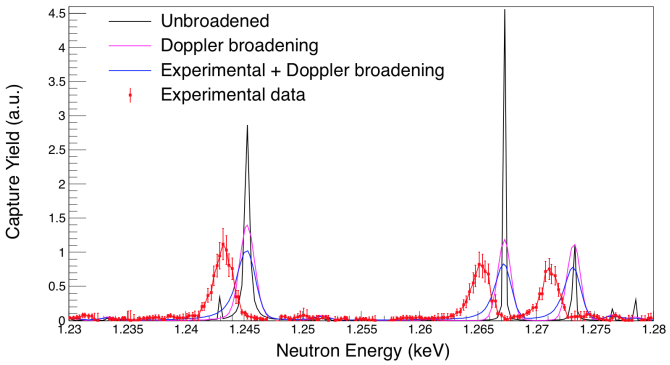

Fig. 3.3: Neutron capture on ^{238}U reaction yield calculated from ENDF/B-VII.1 parameters, comparing different broadening: no broadening at a temperature T=0 K (black curve), only Doppler broadening at T=300 K (magenta curve) and Doppler + experimental broadening (blue curve). Experimental data are shown in red. The n_TOF resolution function has been used for calculation, which, as can be seen, results in an energy shift of the measured data together with their broadening.

Reaction cross-section measurements are mostly carried out on relatively thin samples and therefore the impact of the time t_d can be neglected. However, in case of transmission measurements the finite size of the detector needs to be addes to the final response. This contribution is again best expressed in terms of an equivalent distance λ_d defined by $\lambda_d = vt_d$. As the neutron transport, also this contribution can be estimated by Monte Carlo calculations or approximated by analytical expressions.

The components of the resolution function are considered to be independent distributions, therefore they can be convoluted with each other to obtain the total shape of the resolution function of the TOF spectrometer.

The effect of this spread in time (or equivalently in distance) is dual: first of all, it broadens together with the Doppler effect the observed widths of the resonances. Secondly, experimental data result with an energy shift with respect to the expected energy as calculated via R-matrix formalism. The reason is that in the time to energy conversion as in Eq. 3.5, the time interval at the denominator is the observed time of flight obtained as described in Eq. 3.1, not taking into account the time (or the equivalent distance) that a neutron travels within the target. Applying the resolution function to experimental data results therefore in a shift to higher energies of the energy axis. The two effects of the resolution function are shown in Figure 3.3.

Because of its crucial role in resonance shape analysis (see Section 2.5.2), R-matrix codes like SAMMY [110] and REFIT [127] need a complete description of the resolution function. It can be obtained with both an analytical description of all the different components of the resolution function, and with a numerical input file obtained by MC simulations. It is also worth mentioning that a facility based on spallation source, as

n_TOF, has a more broaden resolution with respect to a white neutron source resulting from photonuclear reactions such as GELINA and ORELA. This difference is mainly due to the geometry of the target-moderator assembly, which is more compact for a neutron source based on photonuclear reaction (size of the target ~ 0.1 m) compared to a spallation-based one (size of the target ~ 0.5 m).

3.3 The n_TOF facility at CERN

The time-of-flight facility of CERN, called n_TOF, became operative in 2001, based on an idea by Rubbia et al. [128], and since then it occupies a major role in the field of neutron cross-section measurements. The facility ran from 2001 to 2004 (n_TOF Phase-1) and, after a four years halt due to technical problem related to the neutron-producing target, it resumed operation at the end of 2008 till the end of 2012 (n_TOF Phase-2). During the Long shutdown 1 (LS1) of CERN [129] a second short flight-path [130, 131], complementing the existing 185 m one, has been constructed from May 2013 and completed on the 25th of July 2014, starting the n_TOF Phase-3.

The pulsed neutron beam at n_TOF is produced by spallation of 20 GeV/c protons from the CERN Proton Synchrotron accelerator on a water-cooled Pb target [122]. The pulsed neutron source is used together with a moderation system, so that the n_TOF neutron beam covers about eleven orders of magnitude in energy from thermal to GeV. A scheme of the facility is given in Figure 3.4.

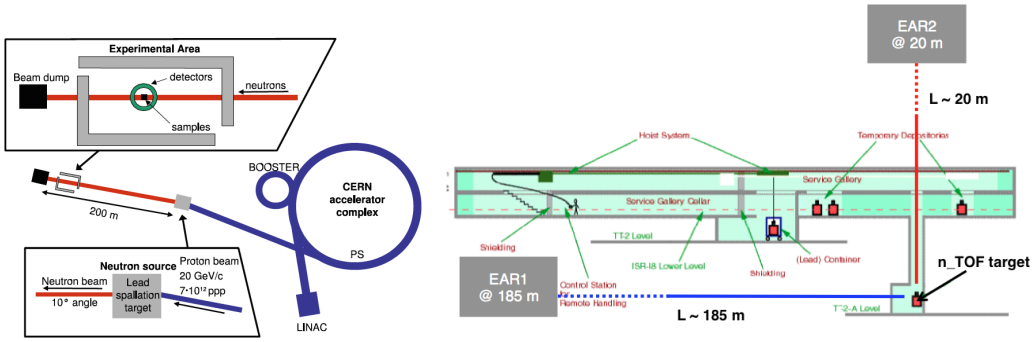

Fig. 3.4: Left: Layout of the n_TOF facility within the CERN accelerator complex [132]. The LINAC feeds the PS-Booster, which provides the PS with protons of 1.4 GeV/c for acceleration up to 20 GeV/c. This beam is extracted and sent to the n_TOF lead spallation target in bunches of 7×10^{12} protons. The experimental hall is located near the end of the 200 m long neutron beam line. Right: Schematic of the two different beam line of the n_TOF facility. The first experimental area (EAR1) is located horizontally at a distance of 185 m from the neutron source, while the new experimental area (EAR2) is located at 90° with respect to the proton beam direction with a flight-path of about 20 m.

The spallation mechanism is a remarkably powerful source of neutrons, and at the proton energy of 20 GeV of the CERN proton synchrotron about 300 neutrons per proton are produced in the n_TOF spallation target. The instantaneous intensity of the n_TOF neutron output is therefore one of the highest among the TOF facilities.

3.3.1 n_TOF neutron beam

Two different spallation targets have been used at n_TOF as neutron-producing targets. The first one, cooled by a 5 cm water layer acting also as the moderator of the neutron spectrum, had to be replaced after four years of operation due to damage caused in some spots by inefficient cooling. The second target, installed in 2008, was equipped with a more efficient cooling system based on water recirculating, and with a separate moderator circuit to permit the use of different moderating materials. This target is made of a monolithic cylindrical block of lead, with length of 40 cm and diameter of 60 cm. On the neutron exit face of the target opposite to the proton entrance one, cooling is ensured by a water layer of 1 cm thickness, while moderation of the neutron spectrum is performed with a 4 cm thick layer of either normal, heavy or borated water. Borated water is now mostly being used to minimize the production of 2.2 MeV in-beam γ rays from $n + \mathrm{H} \rightarrow {}^{2}\mathrm{H} + \gamma$, that constitutes the main source of background in measurements of capture cross-sections in the keV neutron-energy region.

The innovative features of the n_TOF neutron beam derive from the characteristic of the primary proton beam coming from the CERN Proton-Synchrotron (PS):

- a high momentum of 20 GeV/c, corresponding to the maximum attainable energy within a magnetic cycle of 1.2 s of the PS;
- a high peak current of 7×10^{12} protons per bunch, with a width of 7 ns (rms);
- a low duty cycle of 0.5 Hz, which corresponds to up to six bunches per supercycle (typically 16.8 s long).

These characteristics are at the origin of the very high intensity of the n_TOF neutron source, of the order of 2×10^{15} neutrons/pulse.

The beam is extracted from the PS and sent onto the spallation target by using a fast extraction system. In terms of peak intensity, the proton beam for n_TOF can be considered among the highest for the PS, thanks to a special compression procedure that allows to reduce the original pulse width of 14 ns to 7 ns. A more detailed technical description of the facility can be found in [133,134]. The proton beam could be delivered on target in two different operational modes:

Dedicated mode. In this mode the nominal 7×10^{12} protons bunch at 20 GeV/c is sent to the target during a 1.2 s PS cycle fully dedicated to n_TOF. The bunch time distribution has a Gaussian shape with 7 ns rms.

Parasitic mode. During the ramping of a slow ejection cycle for the East Hall, before reaching the 24 GeV flat top, at an energy of 19 GeV a $\sim 3.5 \times 10^{12}$ p bunch is extracted from the PS and sent to n_TOF. The advantages of running in parasitic mode are in an easier scheduling, as the slow extraction cycles are present almost all the time.

The proton intensity sent onto the target is measured pulse by pulse through a Beam Current Transformer, BCT, located about 6 meters upstream with respect to the spallation target in the proton beam line. As all the other transformers in the PS complex, the value of the proton intensity is normalized by making periodical calibration procedures. In order to detect any drift of this detector the signal given by a resistive Wall Current Monitor, WCM or pick-up, is recorded [122]. This monitor, which is mounted immediately after the BCT, provides a pulse in the n_TOF control room proportional to the instantaneous proton beam intensity that is used both for normalization purpose and to calibrate the time of flight.

3.3.1.1 Beam related background

At n_TOF one can distinguish three main sources of beam-related background:

1. neutron beam halo,
2. charged particles,
3. in-beam γ rays.

Thanks to the design of beam collimators and shielding, which will be briefly described in the next Section, the neutron flux outside the beam is strongly suppressed. Moreover, one can get rid of charged particles by placing magnets along the beam line.

On the other hand, the presence of neutral particles and γ rays can be only minimized by geometrical consideration, but when present in the beam line they can reach the measuring station. Photons are produced both in spallation reactions and during neutron moderation, and can be separated into two groups: a prompt component resulting from the spallation process itself, observed in the measuring station at 1 μs or less, and a delayed component, mainly due to thermal neutron capture in the moderator and the lead target, with arrival times between 1 and a few hundreds of μs. The prompt component is the γ-flash previously outlined, and is used to determine the t_o of each pulse (see Eq. 3.1). On the other hand, the γ rays of the delayed component arrive at the measuring station

miming neutrons of a few keV energies. From MC simulations it was verified that the strongest contribution is due to the neutron capture on hydrogen, which produces 2.2 MeV γ-rays, and therefore the use of moderator materials different than normal water leads to a significative reduction of this background level. Other minors contribution are due to photons with energies around 7 MeV resulting from the capture on lead, on the Alluminum alloy container and on the iron target support.

3.3.2 The first experimental area (EAR1)

The first beam line operative at n_TOF is about 200 m long and is designed to clean as much as possible the neutron beam from the secondary particles profusely produced in spallation reactions. First of all, the beam line is shifted of an angle of 10° with respect to the incident proton beam direction. With this solution the number of undesired secondary particles is minimized, such as γ rays and charged particles, which are mainly produced in the forward direction. Along the beam line a sweeping magnet is placed at 145 m from the spallation target to deflect all the remaining charged particle in the beam, and the tube has to cross iron and concrete shielding that stop particles travelling around the beam. Two collimators are also present to shape the neutron beam: the diameter of the beam tube is progressively reduced from 800 mm at the exit of the spallation target to 400 mm before the first collimator, and at 175 m from the exit of the target a reduction to a 200 mm diameter is placed before the second collimator and the entrance of the experimental area. The first experimental area (EAR1), where the samples and detection systems are placed, is a 7.9 m long room starting at 182.3 m downstream of the spallation target. The beam line extends 10 m beyond the end of the experimental area and ends in a beam dump consisting of a $49 \times 49 \times 47$ cm^3 polyethylene block containing three radiation monitors. In Figure 3.5 a scheme of the beam line is shown.

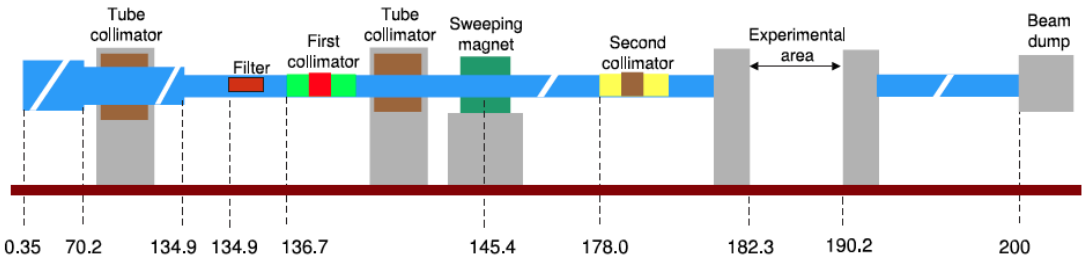

Fig. 3.5: n_TOF beam line from the exit of the target to the end of the tunnel (about 200 m long).

At the beginning of the second experimental campaign (n_TOF Phase-2), the experimental area was upgraded to a *Work Sector Type A*, with a series of safety and monitoring systems, in order to allow measurements of high-activity samples without certified sealing. This key modification was essential to exploit the full potential of the facility.

3.3.2.1 Detection and data acquisition systems

The neutron beam of the n_TOF facility is constantly monitored by two independent low mass devices, placed in-beam during experimental measurements without effecting the neutron beam:

Silicon Monitor (SiMON). This small-mass system is based on a thin Mylar foil with a ^{6}Li deposit, placed in the neutron beam, and an array of silicon detectors, placed outside the beam to detect the products of the ^{6}Li(n,α)^{3}H reaction [135]. The small amount of material in the beam ensures a minimal perturbation of the flux and minimizes the background related to scattered neutrons. Moreover, a further reduction of the γ-ray background has been obtained by constructing the scattering chamber hosting the device in carbon fiber. As the ^{6}Li(n,α)^{3}H reaction cross-section is known with high accuracy with this system is possible to monitor the neutron beam from thermal to about 150 keV.

MicroMegas. MicroMegas [136] are gaseous detectors based on simple geometry with planar electrodes developed by Nobel Laureate G. Charpak. The gas volume is separated in two regions by a so-called micromesh, a thin metallic foil (several μm) which surface is composed of holes having a 35 μm of diameter and spaced on 100 μm. A low electric field ($\sim$ 1 kV/cm) is applied to the first region where the conversion and drift of the ionization electrons occur. In the amplification region, a high field (40 to 70 kV/cm) is created by applying a voltage of a few hundred volts between the micromesh and the anode plane, which collects the charge produced by the avalanche process. The anode can be segmented into strips or pads. These detectors are very fast and therefore well suited for high counting rates [137]. In order to operate MicroMegas as a neutron detector, an appropriate neutron-to-charged particle converter must be employed. For the n_TOF flux-monitor two solid converters have been chosen: ^{10}B(n,α) for neutron energy up to 1 MeV and ^{235}U(n,f) for higher neutron energies [138]. The cross sections of these two reactions are very well known in the cited energy intervals.

For capture measurements, two different detection systems have been set up: an array of deuterated liquid scintillator detectors (C_6D_6), and a 4π BaF_2 Total Absorption

Calorimeter (TAC). The first apparatus is characterized by a low sensitivity to background signals induced by scattered neutrons, further minimized at n_TOF by the use of carbon fiber for detector housing and support. For highly radioactive and fissile isotopes, in particular for minor actinides, capture measurements are performed with the TAC, which permits the identification of capture events from competing reactions by reconstructing the total energy of the γ-ray cascade. The relatively large neutron sensitivity of the apparatus is reduced by hardware expedients. Both these detection systems are discussed in detail in Chapter 4.

Different detection systems are exploited also for fission cross-section measurements. A multi-stack Fission Ionization Chamber (FIC), used in the first campaign, has been replaced in Phase-2 by a high-performance MicroMegas detector [136,139], characterized by a better signal-to-noise ratio. A second method used at n_TOF relies on the detection of both fission fragments in coincidence. To this purpose, a stack of position-sensitive Parallel Plate Avalanche Counters (PPACs) is used, which also determines the angular distribution of fission fragments [140,141]. In all fission measurements, the ratio method is used, which consists in determining the cross section of a given isotope relative to that of ^{235}U, being a well established standard. To this purpose, reference samples of ^{235}U are always mounted in the detector in use and measured simultaneously.

The Data Acquisition System (DAQ) of the n_TOF facility, presented in detail in Ref. [142], is fully digital, flexible and almost dead time free. The main advantage of such a system is that it allows the offline analysis of the recorded pulses, using dedicated pulse shape analysis (PSA) algorithms optimized for each detector type [143, 144]. For each detected event the PSA routine records the useful information of the detector signal. As an example, for capture measurements the energy deposited in the detector by γ-rays, the time of flight of the event and the number of protons that hit the spallation target are recorded for further offline analysis.

A scalable and versatile data acquisition system has been designed based on 8-bit flash-ADCs with sampling rates up to 2GHz and 8 Mbyte memory buffer. For the ^{238}U(n,γ) reaction cross-section measurement two channels of Acqiris-DC270 digitizers working at 500 MSamples/s are used per detector. This system corresponds to 16 ms long data buffers containing digitized signals of the C_6D_6 detectors for neutron energies between 0.3 eV and 20 GeV. A reduction in the sampling rate down to 100 MSamples/s extends the measurable range of neutron cross-sections in the $1/v$ energy region down to 0.028 eV.

A fast zero-suppression algorithm selects only those data with an amplitude above an user-defined threshold for each flas-ADC channel, reducing in this way the amount of data to be stored. After the zero suppression, the raw data are sent to a temporary

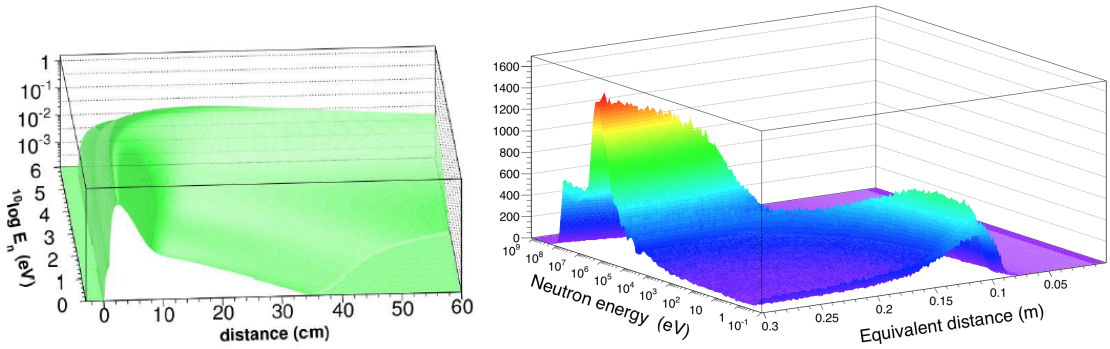

Fig. 3.6: Resolution function at the EAR1 sample position (185 m) of the n_TOF facility obtained from FLUKA simulations. It is given as a distribution of the equivalent distance as a function of the neutron energy. Left: For n_TOF Phase-1, in the range from 1 eV and 1 MeV neutron energy (picture from [150]). Right: For the n_TOF Phase-2, in the range from 0.1 eV and 1 GeV neutron energy.

disk pool close to the measurement station and, once closed, to the CERN Advanced STORage manager (CASTOR) [145].

3.3.2.2 Resolution Function

The resolution function (RF) of the first experimental area of the n_TOF facility has been simulated in the start-up phase by two different codes, FLUKA [146] and CAMOT [147], giving similar results within the available statistics. In n_TOF Phase-1, the simulated resolution function results were used to derive an analytical description in the range from 1 eV to 1 MeV [148], given the RF as a function of six energy-dependent parameters. The form of the resolution function is known as the modified RPI function and is present in the resonance shape analysis codes SAMMY and REFIT.

In the second phase of n_TOF, the new spallation target-moderator assembly has been simulated again with FLUKA and MCNP [149] Monte Carlo codes for both the configuration with normal and borated water as moderator material. A numerical description of the n_TOF resolution broadening has been made available in SAMMY and REFIT R-matrix codes, which results in a very accurate description of the overall broadening and provides more flexibility at the stage of data analysis. The two resolution functions for Phase-1 and Phase-2 are shown in Figure 3.6.

Studying the simulations, it has been noticed that the effects of the different moderators are significative only at very low neutron energy, where however broadening effects are dominated by Doppler broadening [123, 148]. At higher energies, in the keV region, there are essentially no differences between the configurations with normal or borated

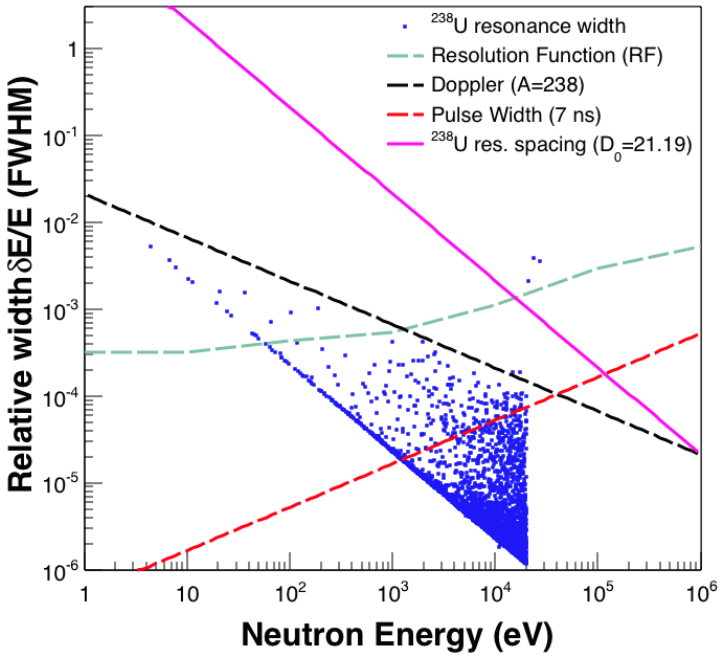

Fig. 3.7: Illustration of the various component contributing to the observed resonance widths as function of neutron energy. Top: study of the ^{232}Th isotope, Figure from [148]. Bottom: study of ^{238}U isotope for this work.

water as moderator of n_TOF Phase-2, but sizeable differences have been noticed with respect to Phase-1 resolution function.

To further illustrate the impact of the resolution function, a number of relative widths are displayed in Figure 3.7 for the case of ^{238}U. They all correspond to the relative widths at one half maximum ($\delta E/E$ (FWHM)), except for the resonance spacing where D_0/E is displayed. In the figure, the individual broadening components (Doppler, resolution function and proton pulse width) are displayed as dashed lines. The overall resonance broadening is to be compared with the intrinsic widths (blue points) and resonance spacing (pink solid line) of the ^{238}U resonances (values are taken from the evaluated library ENDF/B-VII.1 [114]). The comparison shows that the observed width for all the resonances will be dominated by the experimental broadening, but also that the broadening remains lower than the resonance spacing up to $E_n \sim 20$ keV, allowing in this way the differentiation of neighbouring resonances below this energy limit.

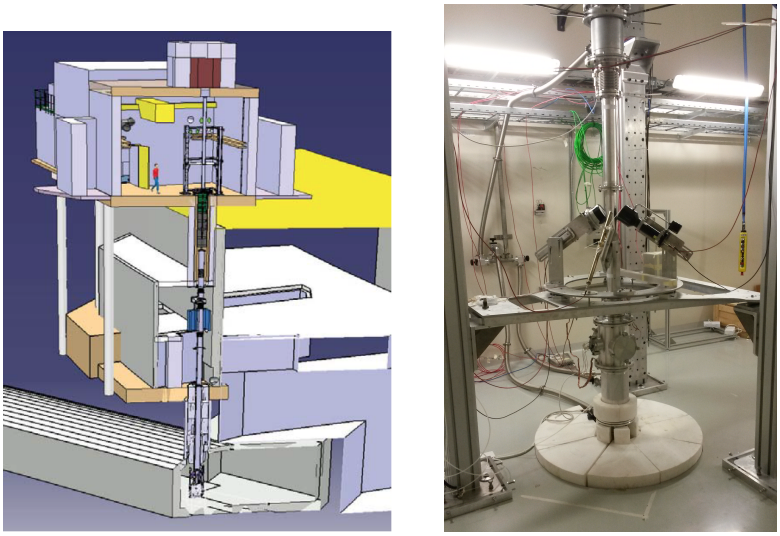

Fig. 3.8: Left: Schematic drawing of the 20 m vertical flight-path and of the second experimental area that is operative since the 25th of July 2014 at _TOF. A permanent magnet (in blue), a collimator just below the experimental area, and a beam dump on top of the building will be used to shape the beam and minimize the background in the measuring station. Right: First experimental setup in EAR2 with four C_6D_6 scintillators.

3.3.3 The second experimental area (EAR2)

As previously outlined, a second experimental area (EAR2) has been just built at the vertical of the spallation target, at the much shorter distance of 20 m than the first measuring station. A schematic view of the new beam line is presented in Figure 3.8 together with the first measurement setup with C_6D_6 scintillators.

The present target-moderator assembly is designed to have a dedicated pool for moderation materials only in the target face opposite to the one where the proton beam impinges. For this reason, with a vertical beam-line only normal water can be used as moderator, with the results of a consistent background due to in-beam γ rays. Following the same idea of the first beam line, also along the second one a permanent magnet is placed to deviate all the undesirable charged particle. Two collimators are present to shape the neutron beam, the second of which is placed just below the floor of the experimental area and contains a Pb shielding for in-beam γ rays.The polyethylene beam dump is covered with a B_4C layer to reduce the back-scattering neutron background.

The extremely high neutron flux available in EAR2, approximately a factor of 25 higher than in EAR1, and the still reasonable energy resolution, will open the way to a complete set of new measurements, currently not feasible at n_TOF (or at any other facility around the world). In particular, the second experimental area will make feasible

measurements of isotopes with very low cross section or available in very small quantity (<1 mg). Moreover, the combination of the much higher flux and shorter time of flight will make possible the measurement of neutron cross-sections of unstable isotopes with very high specific activity, i.e. with half-life as short as a few years, thanks to a drastic improvement of the signal-to-background ratio, being in this case the main background related to the natural radioactivity of the sample.

The range of possible measurements, of interest for Nuclear Astrophysics and nuclear technology, is rather vast, with the limitation related mostly to the availability of samples. In this regard, samples of short lived isotopes of interest for Nuclear Astrophysics could be produced by implantation of radioactive beams at the RIB facility ISOLDE at CERN.

Examples of measurable reactions are the (n,cp), very challenging measurements related to nuclear astrophysics and medicine, together with the studies of capture and fission cross-sections on various unstable Pu and U isotopes of great importance for the design of new nuclear systems.

3.4 Neutron flux

A fundamental piece of the puzzle of high precision and accuracy measurements of reaction cross-sections is the point-wise knowledge of the incident neutron flux as a function of energy. The knowledge of its energy dependence is as much important as knowing its absolute value, considering that often cross sections are measured relative to some well known quantity in a particular energy range as, for example, a standard cross section, the cross section value at thermal energies or the capture yield at the top of a well isolated saturated resonance.

At n_TOF the neutron flux was experimentally determined using several detection systems based on different principles and reactions. A large effort has been devoted to minimize all the possible sources of uncertainties, both systematic and statistical, in particular on the energy dependence of the neutron flux. The measurements, their analysis and their combination for the determination of the so-called evaluated neutron flux are briefly presented here. All the details could be found in [151].

The neutron flux $\Phi(E_n)$ is defined as the number of neutrons per incident proton pulse (neutrons per bunch) and integrated over the full spatial beam-profile arriving at the experimental hall with a given energy. It is extracted through measurements of standard (i.e. extremely well known) reaction cross-sections of materials called neutron converters, according to the relation [151]

$$\Phi(E_n) = \frac{C(E_n) - B(E_n)}{\varepsilon(E_n) \cdot \left(\mathrm{e}^{-n\sigma_{\mathrm{tot}}(E_n)}\right) \frac{\sigma_r(E_n)}{\sigma_{\mathrm{tot}}(E_n)}}. \tag{3.8}$$

Here, C is the number of counts detected per bunch, B the background contribution and n the areal density in atoms per barn of the deposit used for neutron conversion. The quantities σ_r and σ_{tot} are, respectively, the reaction and total cross-section for the isotope used as neutron converter. To determine the n_TOF flux evaluated cross-sections from the ENDF/B-VII.1 library were used for ^{6}Li, ^{10}B and ^{235}U. Finally, ε is the efficiency for detecting the product of the neutron interaction. All these quantities, apart from n, are function of the neutron energy E_n. For this reason, the uncertainty on the energy dependence of the flux depends, for each detector, on the uncertainty on the reaction cross-sections as well as on the variation with energy of the efficiency correction.

The materials used as neutron converters have a neutron cross-section which is standard in a specific energy range [152]. For this reason, a combination of independent measurements performed with different detectors is used to cover the entire energy range of the n_TOF neutron beam. The detectors for charged particles SiMON [135] and MGAS [138, 139], described in Section 3.3.2.1, have been used to measure ^{6}Li(n,α) and ^{10}B(n,α) reactions, which feature standard cross sections from 25 meV to 1 MeV. In addition, the detectors H19 from PTB [153], MGAS [138, 139] and PPAC [140] have all been used to measure ^{235}U(n,f) reactions, whose cross section is standard at 25 meV and in the interval between 150 keV and 200 MeV. This latter reaction has also been used as reference above 200 MeV, due to the absence of any standard cross section at such high energies.

Apart from the uncertainties in the cross sections, the data each detector could provide are limited in energy by experimental conditions. For instance, the uncertainty in the angular distribution of reaction products in the ^{6}Li(n,α) reaction prevents the use of SiMON detector for $E_n \geqslant 150$ keV. Moreover, the effects of the γ-flash limit the use of the H19 (PTB) and MGAS with ^{235}U fission chambers beyond $\sim$ 3 and $\sim$ 10 MeV respectively. In the case of MGAS (^{10}B), the background caused by proton recoils from elastic n-p collisions in the gas limits the high energy range up to only few hundreds of keV.

In Table 3.2 all the detectors used to determine the n_TOF evaluated flux are listed with the energy regions in which each of them provides reliable data.

Table 3.2: Summary of the detectors used to determine the n_TOF neutron flux including the reaction of interest, the energy range in which the react is considered a standard, the sample thickness and the approximate upper energy limit below which each detector gives reliable results.

Detector	Sample and reaction	Area density (μg/cm^2)	E_n where σ_r is standard	Upper E_n limit for reliable data
PTB	^{235}U(n,f)	500 (10 samples)	25 meV, 0.15 to 200 MeV	3 MeV
SiMON	^{6}Li(n,α)	300	25 meV to 1 MeV	150 keV
MGAS	^{10}B(n,α)	55	25 meV to 1 MeV	150 keV
MGAS	^{235}U(n,f)	470	25 meV, 0.15 to 200 MeV	10 MeV
PPAC	^{235}U(n,f)	279	25 meV, 0.15 to 200 MeV	1 GeV

3.4.1 Neutron beam at EAR1

During the n_TOF Phase-2 the measurements outlined above, with all the five different detectors, have been repeated at the beginning of each year in 2009, 2010 and 2011. Figure 3.9 shows the evaluated flux for each one of the three years. In 2009 normal water was used as moderator, while starting in 2010 it has been substituted by borated water. The effect of the different moderator materials is a strong reduction of the thermal peak. The small difference in the thermal region between 2010 and 2011 is related to a slight modification of the moderator circuit, which implies a controlled change of the ^{10}B concentration in the borated water. Above a few keV, the flux does not depend on the moderator liquid used anymore and is therefore equal for all the three years.

In Table 3.3 the overall estimated systematic uncertainties for different energy ranges are summarized. For neutron energies from thermal to 100 keV, the systematic uncertainty was estimated on the basis of the comparison between the various experimental results, while at higher energy, where only the PTB or the PPAC systems were used, the reported values are the combination of the uncertainty of the reference cross sections ($\sim 1\%$) and of the corrections for dead time and angular distribution effects. More details can be found in Ref. [151].

The spatial profile of the neutron beam at the sample position is mainly shaped by the characteristics of the second collimator. At n_TOF there are two possible collimation modes, namely fission and capture, which corresponds to two different collimators providing neutron beams of different size. Moreover, the beam profile varies with neutron energies, because neutrons are produced at different position in the target and emitted at different angles depending on their energy. The knowledge of this spatial profile is of particular importance when the sample being measured is smaller than the neutron beam,

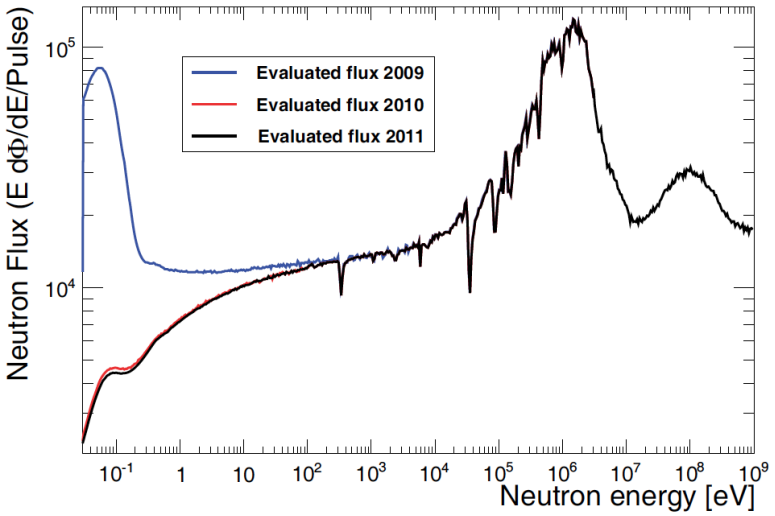

Fig. 3.9: Neutron flux at EAR1 for the n_TOF Phase-2 campaigns in 2009, 2010 and 2011 from thermal to 1GeV neutron energy. Figure from [151].

Table 3.3: Summary of the overall systematic uncertainties for different energy regions of the n_TOF neutron flux.

Energy range	Uncertainty
0.025 eV to 100 eV	1%
100 eV to 10 keV	2%
10 keV to 100 keV	4-5%
100 keV to 10 MeV	$\sim$ 2%
10 MeV to 1 GeV	$\sim$ 3%

intercepting therefore only a fraction of it that is referred to as the Beam Interception Factor (BIF).

During the n_TOF Phase-2 campaigns the spatial profile of the neutron beam and its energy dependence in the capture collimator configuration has been investigated in detail by means of a new 2D pixelated MicroMegas (pixel-MGAS) detector [154]. An illustration of the n_TOF beam profile at 183.2 m flight-path is given in Figure 3.10, where the beam projection in the vertical direction for neutron energies between 0.1 and 1 eV is shown for both capture and fission collimation modes. The capture mode includes both the measurement with the pixel-MGAS and simulations, while in the fission collimation mode only the simulations are available. It is observed that the full size of the beam is $\sim$ 3.5 cm and $\sim$ 10 cm in diameter in the capture and fission collimation modes, respectively.

3.4.2 Neutron beam at EAR2

In the recently built second experimental area, only very preliminary measurements of the neutron flux have been carried out. A new Silicon Monitor (SiMON2) has been developed following the same principles of the Silicon Monitor used in EAR1, but with a more compact geometry and a LiF deposit (instead of the pure ^{6}Li one of SiMON). In Figure 3.11 the preliminary flux at EAR2 obtained with this new detector is presented in comparison with the result of FLUKA simulations, which are in very good agreement, and together with the EAR1 flux. It is apparent that the flux in EAR2 is a factor between 20 and 35 higher than the EAR1 one, fulfilling the expectations.

The resolution function of the second experimental area at n_TOF is currently under study. Together with all the factors described in Section 3.2.1, additional broadening is expected due to the angle between the moderator face and the flight-path (which in the EAR1 are perpendicular). This fact, together with the different traversal planes of the lead target crossed by neutrons, makes the derivation of the EAR2 resolution function much more complicated than a trivial extension at 90° of the EAR1 one.

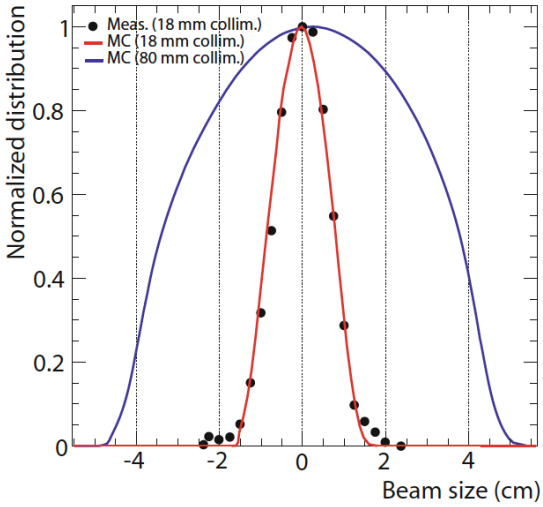

Fig. 3.10: Neutron beam profile at 183.2 m from the spallation target in the vertical direction as measured with the pixel-MGAS detector at low neutron energy (0.1−1 eV). Figure from [123]

3.5 Summary

Experimental facilities to obtain a neutron beam have been here introduced, and among them the time of flight (TOF) technique and facilities have been described. In particular, the n_TOF facility at CERN has been presented in detail, in order to comprehend how high precision measurements such as the ^{238}U(n,γ) could be carried out. The neutron beam-line and the Data Acquisition system have been studied together with the resolution function of the n_TOF spectrometer, which is a fundamental input for RSA codes in order to correctly analyze resonance parameters. The experimental apparatus for fission and capture measurement is here briefly presented, which will be further developed in the next chapter. Moreover, the incident neutron flux in the first experimental area (EAR-1), where the measurement of this work has been performed, is presented as evaluated in Ref. [151] with the help of five different detection system.

The brand-new second experimental area (EAR-2) has been introduced, where a complete new set of experimental measurements could be performed, currently not feasible at n_TOF or at any other facility around the world.

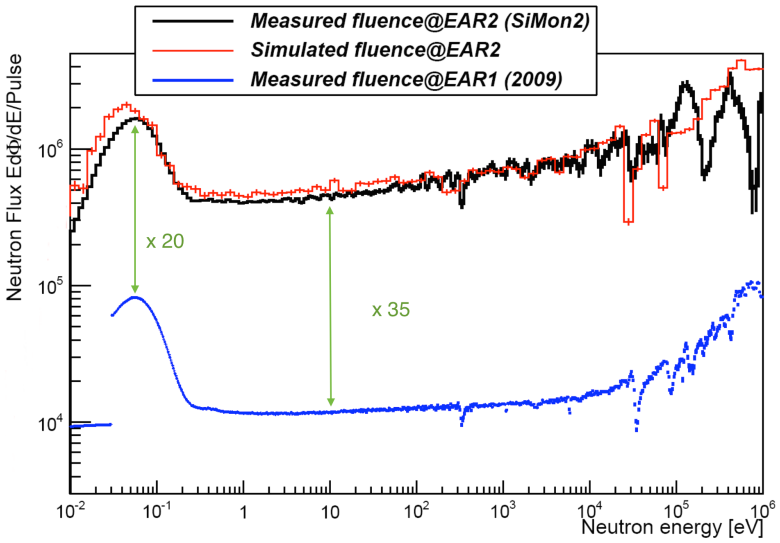

Fig. 3.11: Preliminary neutron flux at the n_TOF EAR2 (black) in comparison with simulations (red) and 2009 EAR1 evaluated flux (blue).

Chapter 4
Neutron cross sections measurements

The aim of this chapter is to examine the methods to measure the reaction cross-sections induced by neutrons. Among the several existing experimental methods, here the principles and the detection technique for both transmission and capture measurements will be described. In particular, the two detection techniques used at the n_TOF facility for capture experiments will be analyzed in detail together with their two major background issue: the correction for the multiple scattering and the sensitivity of the capture setups to neutron scattering.

4.1 Total cross-section measurements

Total cross-sections σ_{tot} are generally measured through the so-called transmission experiments. In these measurements, neutron detectors are placed at the end of the neutron beam-line, and the number of neutrons are counted both with, C_{in}, and without, C_{out} a given sample in the beam. The experimental observed quantity, called neutron transmission, is simply the ratio between the two counting rate corrected for dead time and background and depends on the neutron energy E_n. This neutron transmission is related to the total cross section by [117]:

$$T_{exp}(E_n) = N\frac{C_{in}(E_n) - B_{in}(E_n)}{C_{out}(E_n) - B_{out}(E_n)} \simeq e^{-n\sigma_{tot}}. \tag{4.1}$$

Here, B_{in} and B_{out} indicate the contribution of the background, while N is a normalization factor which takes into account the different numbers of neutrons devoted for the *sample-in* and *sample-out* measurements. Since the detector efficiency cancels out using the same detector in sample-in and sample-out measurements, the uncertainty left is only related to the monitoring of the number of incident neutrons.

It is important to notice that the relation between experimental transmission and total cross-section expressed in Eq. 4.1 is valid only under the conditions that (*i*) the target is perpendicular with respect to the incoming neutron beam, and (*ii*) that all the detected neutrons have crossed the sample, avoiding to detect neutrons scattered by the sample. For this reason, a good transmission geometry should be implemented properly collimating the neutron beam at the sample position and selecting a small solid angle between the sample and the detector. Furthermore, the choice of a suitable sample is fundamental, which should be homogeneous and with an optimized density for the ongoing measurement.

4.2 Capture cross-section measurements

4.2.1 Principles

In capture experiments the measurement of the capture cross-section σ_γ is performed indirectly detecting the particles emitted in the process, i.e. the γ-rays coming from the de-excitation of the compound nucleus. The observable quantity is the fraction of incident neutrons which undergo a reaction in the sample and generated a signal in the detection system, and it is referred to as capture yield. The experimental yield is related to the detected counting rate C_c by [117]:

$$Y_{exp}(E_n) = \frac{C_c(E_n) - B(E_n)}{A\varepsilon\phi_n(E_n)}, \tag{4.2}$$

where $B(E_n)$ indicates the contribution of the background, ε is the efficiency of the detection system, A is the effective area of the sample intercepted by neutron beam and ϕ_n is the incident neutron flux. The systematic uncertainties related to a capture measurement are therefore due to the accuracy in the characterization of the background and the neutron fluence[1], and in the determination of the detector efficiency.

For non fissionable samples and energies below the first inelastic scattering level, the theoretical value of the yield is a function of total (σ_{tot}) and reaction (σ_γ for capture and σ_n for elastic) cross-sections, and of the areal density n of the sample expressed in atoms per barn. The theoretical yields can be expressed as:

$$Y_c(E_n) = \left(1 - e^{-n\sigma_{tot}(E_n)}\right) \frac{\sigma_\gamma(E_n)}{\sigma_{tot}(E_n)} + Y_M \tag{4.3}$$

[1] With neutron flux ϕ_n is intended the number of neutrons per unit of time and area, i.e. n s^{-1} m^{-2}. The neutron fluence Φ_n (usually referred to as neutron flux as well) is instead the flux integrated over time, i.e. n m^{-2}.

for radiative capture and

$$Y_n(E_n) = \left(1 - e^{-n\sigma_{tot}(E_n)}\right) \frac{\sigma_n(E_n)}{\sigma_{tot} E_n} - Y_M \tag{4.4}$$

for elastic scattering [117]. Here, Y_M accounts for the contribution due to capture events following at least one neutron scattering in the sample, which is called multiple scattering. The term in brackets is related to the neutron self-shielding.

In a capture measurement the expectation value of the yield is not a pure theoretical capture yield, but a weighted sum of both elastic and capture yield:

$$Y = \varepsilon_\gamma Y_c + \varepsilon_n Y_n. \tag{4.5}$$

The weights can be identified as the efficiencies to detect the signal due to a capture event (ε_γ) or to a γ-ray related to a subsequent capture, in the detector material itself or in the experimental hall, of a neutron scattered by the sample (ε_n). The ratio between the two efficiencies, i.e. $\varepsilon_n/\varepsilon_\gamma$, is called neutron sensitivity and will be examined in detail in Section 4.4.

To compare the experimental yield to its expected value, the geometry of the whole system (including the effective area of the sample) and the absolute value of the neutron fluence should be precisely known. Since in most cases this is not possible with a satisfying accuracy, all these factors are usually included into a single and energy-independent normalization factor N. This factor could be derived with two distinguished procedure:

- From measurements based on standard cross-sections. Usually, capture cross-section at thermal energy or standard cross-sections for higher energy region are used as reference cross-sections;
- From measurements independent of any reference cross-sections, based on a resonance for which the neutron width is much smaller than the radiative one ($Gamma_n \ll \Gamma_\gamma$). To this purpose, two type of resonances could be suitable: (i) resonances for which the total cross-section at the peak energy is much less than unity ($n\sigma_{tot} \ll 1$), so that the capture area is almost proportional to the neutron width and can be determined very accurately from independent transmission measurements, and (ii) saturated resonances. A saturated resonance has a cross section at peak energy much larger than one ($n\sigma_{tot} \gg 1$), and all the incident neutrons with energies close to the resonance one would interact with the sample. If in addition the capture width is larger than the neutron width, the theoretical capture yield for this resonance is close to unity, value that has to be compared with the one obtained experimentally. It was demonstrated [165] that this method is extremely convenient. Appropriate resonances that can be exploited to apply the saturated resonance method are the 4.9

eV resonance of ^{197}Au, the 5.2 eV resonance of ^{109}Ag and the 6.67 eV resonance of ^{238}U. The normalization procedure used for this work will be explained in Section 5.5.

Multiple scattering

Considering thin samples, for which $n\sigma_{tot} \ll 1$, the theoretical capture yield Y_c could be approximated so to make its dependence on the capture cross-section linear (this procedure is usually referred to as thin-sample approximation):

$$Y_c(E_n) \approx n\sigma_\gamma(E_n). \tag{4.6}$$

On the contrary, for thick samples with large $n\sigma_{tot}$, a non negligible probability exists that a neutron before being captured would be scattered one or more times inside the sample itself. In these cases it is therefore convenient to write the total capture yield as a sum of three different terms:

$$Y_c = Y_0 + Y_1 + Y_{\geqslant 2}, \tag{4.7}$$

where the Y_0 term is the primary capture yield and is given by the first part of Eq. 4.3. The second part of Eq. 4.3, i.e. Y_M, is here split between Y_1, that indicates the contribution due to capture events after one elastic scattering in the target, and $Y_{\geqslant 2}$, that refers to neutron capture events after more than one neutron scattering. These higher order terms are increasingly complicated functional of the cross section, and can be calculated by means of dedicated Monte Carlo simulations.

4.3 Detection techniques

As theoretically described in Chapter 2, a neutron capture event is followed by the prompt emission of a γ-rays cascade from the de-excitation of the compound nucleus. The total amount of energy available in this process is the sum of the neutron binding energy and the incident neutron kinetic energy. The former one could vary from few MeV to tens of MeV, depending on the target nucleus. The latter one depends on the characteristics of both the neutron source and the sample, being the energy in the center of mass frame as in Eq. 2.4 dependent on the mass number of the target isotope. At the n_TOF facility the incident-neutron energies spread over a wide range from thermal energy to GeV.

The ideal (n,γ) detector has to fulfil three different requirements:

i. A detection efficiency independent of the multiplicity of the capture gamma cascade;

ii. A low sensitivity to scattered neutrons (see Section 4.4 for further details);
iii. An extremely good time resolution.

The first requirement could be achieved with two completely different techniques, which divide the various detectors into two well-separated classes: Total Absorption Detectors and Total Energy Detectors. At the n_TOF facility both detection systems are present.

4.3.1 Total Absorption detection system

The general idea of the Total Absorption technique is to detect the entire γ-ray cascade. To reach this aim, γ-ray detectors should subtend a solid angle approaching 4π, and their thickness should be such that the interaction probability with any photon crossing them is close to the unity. The efficiency of such a detection system approaches 100% and, therefore, is independent of the multiplicity of the γ-ray cascade spectrum. With this technique the entire detected event is reconstructed in terms of total energy released and, if the detectors is segmented in enough independent modules, of multiplicity of the event itself. This possibility leads to a clear signature of capture events, with the consequence of an excellent discrimination from background signals due to single γ-ray or fission events.

Thanks to its characteristics, the Total Absorption technique is best suited for measuring radioactive as well as small mass samples, and therefore large arrays of inorganic scintillators have been built following the requirements of the technique. What distinguish different detection systems is the choice of the scintillators. Since the detector volume has to be large to absorb the whole γ-ray cascade, it is important to pay attention at the chemical composition of the scintillators: to lower the neutron sensitivity related background, in fact, elements with high (n,γ) cross section must be excluded. For example, NaI and CsI are to be avoided because of the large capture cross-section of Iodine. Out of the remaining suitable scintillator the final choice is a compromise between energy resolution, time resolution and sensitivity to scattered neutrons. A detailed comparison of suitable scintillators can be found in [155].

The n_TOF Total Absorption Calorimeter (TAC) [156] consists of 40 BaF_2 crystals, 12 pentagonal and 28 hexagonal, which cover 95% of the 4π solid angle. Each individual module is mounted on an Al honey-comb structure that is holding the complete detector. The detector assembly is divided into two hemispheres, one of which can be moved to access the interior of the detector, and in particular the centre of the TAC where the sample is placed. To lower the neutron sensitivity the sample is surrounded by a spherical neutron moderator/absorber made of an inert non flammable lithium salt

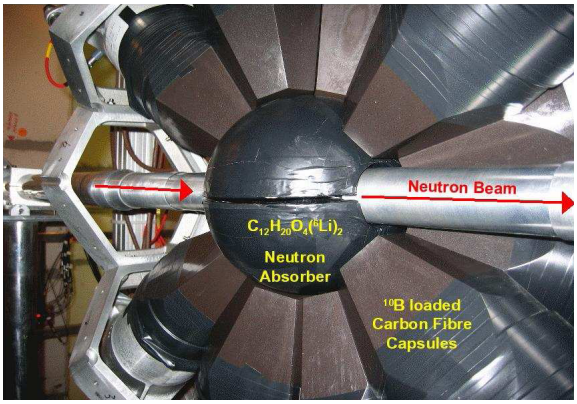

Fig. 4.1: View of one of the hemisphere of the TAC with the neutron absorber placed in the centre and the neutron beam line passing through the detector assembly.

($C_{12}H_{20}O_4(^6Li)_2$), while each crystal is encapsulated in a ^{10}B loaded (16% in mass) carbon fiber shield. Figure 4.1 shows a picture of one of the hemispheres with the neutron absorber placed in the centre of the assembly.

4.3.2 Total Energy detection system

The second technique used to measure capture event, the Total Energy technique, requires that the efficiency of the detection system is directly proportional to the total radiative energy emitted by the capture event (i.e. the sum of the neutron separation energy S_n and the kinetic energy of the incident neutron E_n [2]). To achieve this feature low efficiency detectors should be used, with a γ-ray detection efficiency proportional to the γ-ray energy. An exploitable procedure to achieve this proportionality is the use of a proper geometry of the detectors with the so-called Moxon-Rae detectors [157]. However, the use of this type of detectors has been abandoned due to the non-proportionality of their efficiency below 0.5 MeV and their excessively low detection efficiency [158].

An alternative solution is to achieve the required proportionality through the *pulse-height weighting method*. This technique is based on an original suggestion by Maier-Leibnitz, that one can always find a function $W(E)$ of the pulse height such that its convolution with the pulse height distribution of the capture spectrum is proportional to the total energy released. This technique was initially applied by Macklin and Gibbons [159]

[2] For sake of completeness in the lab frame system the recoil energy of the target nucleus should be subtracted to obtain the actual energy available for radiative emission. However, in most cases this energy is several order of magnitude lower than the sum of the neutron separation and kinetic energy, and could be safely neglected.

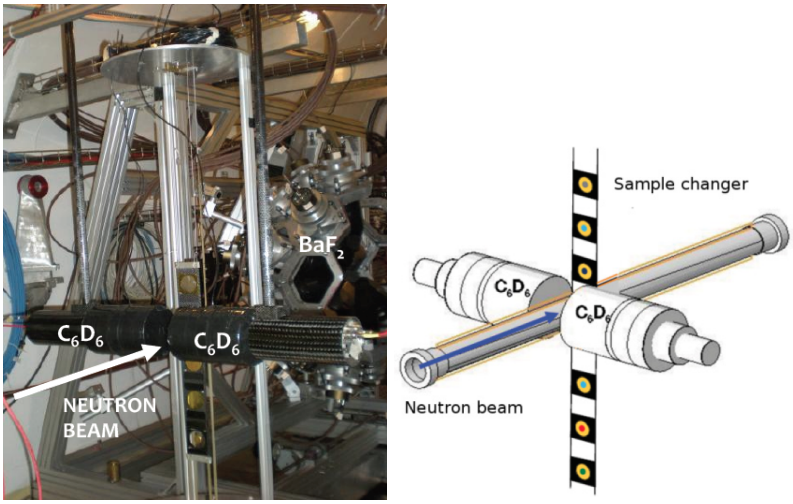

Fig. 4.2: View of the Total Energy system experimental setup at the n_TOF facility. The two C_6D_6 detectors are placed at 90° with respect to the beam direction. The detectors support is made in carbon finer in order to minimise the scattered neutrons background.

using C_6F_6 detectors, but nowadays the use of the C_6D_6 scintillators is preferred due to their lower neutron sensitivity [158]. At the n_TOF facility the detection setup to exploit the Total Energy system consists of two C_6D_6 scintillation detectors placed one head on the other at 90° from the beam direction (see Figure 4.2). For the measurement of this work, one commercial Bicron detector was used together with a custom made one developed at the Forschungszentrums Karlsruhe (from now on it will be referred to as FZK) [160]. Both detectors are optimized to have a very low neutron sensitivity. To this purpose the amount of material constituting the detectors has been minimized, and the chosen materials have a low neutron capture cross-section. As an example, for both detectors the window of the photomultiplier is a custom quartz window, and the housing of the FZK detector is made of carbon fiber.

The principle of the detection system is that at most one γ-ray out of the capture cascade is detected at a time. As a consequence, the efficiency to detect a capture event ε_c could be approximated by:

$$\varepsilon_c = 1 - \prod_i (1 - \varepsilon_{\gamma i}) \approx \sum_i \varepsilon_{\gamma i}. \tag{4.8}$$

If the efficiency to detect a γ-ray is proportional to the energy of the γ-ray itself, i.e. $\varepsilon_\gamma = kE_\gamma$, the detection efficiency for a neutron capture event becomes directly proportional to the sum of the γ-rays energies, $E_{\gamma i}$, emitted in the capture event. Neglecting the internal conversion process, the detection efficiency attains the direct proportionality

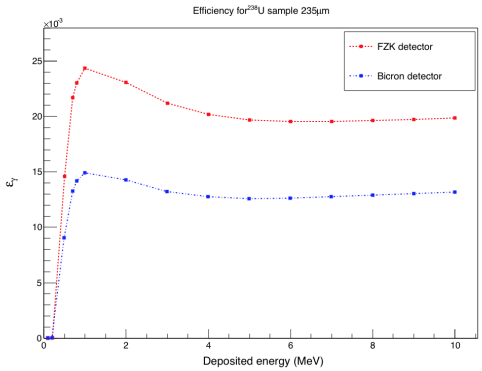

Fig. 4.3: Simulated γ-ray detection efficiency for a γ-ray homogeneous emission within the ^{238}U target (rectangular in shape, 235μm thick). The detection system is the one used for this measurement, consisting of 2 C6D6 detectors placed at 90° with respect to the direction of the incoming neutron beam.

to the total excitation energy E_x, which is the sum of the neutron separation energy S_n and the incident neutron energy in the center of mass system $E_{n,c}$:

$$\varepsilon_c \approx k \sum_i E_{\gamma i} \approx k(B_n + E_{n,c}) = kE_x. \tag{4.9}$$

Such an efficiency results to be independent of the capture cascade energy and multiplicity as required.

Differently to the TAC, the C_6D_6 setup is optimized for cases in which the total cross-section is dominated by the elastic channel. These detectors are in fact characterized by a very low neutron sensitivity, two orders of magnitude smaller than that of the TAC, and therefore allow us to obtain reliable results even for extremely small Γ_γ/Γ_n ratios. Moreover, a drawback of the TAC is that the γ-flash blinds the detectors for energies above tens of keV, and therefore the C_6D_6 setup is the only available experimental method at the n_TOF facility to measure radiative capture cross-sections at high neutron energies.

Pulse Height Weighting Technique (PHWT)

From Figure 4.3 it is clear that the γ-ray detector efficiency for the two C_6D_6 detectors is low but not directly proportional to the energy of the detected γ-ray. As mentioned before, this proportionality is achievable through a mathematical manipulation of the response function of the detection system. To this purpose a weighting function $W(E_d)$ is defined such that it follows the relationship:

$$\int_0^\infty R_d(E_d, E_\gamma)\, W(E_d)\ \mathrm{d}E_d = kE_\gamma, \tag{4.10}$$

where the proportionality constant k is usually taken equal to 1 MeV^{-1} when deriving the weighting functions. With $R_d(E_d, E_\gamma)$ the response of the detection system is indicated, defined as the probability that the detected energy E_d is deposited by a γ-ray with an energy E_γ. The total efficiency to detect a γ-ray with an energy E_γ is therefore given by the integral of the response over all the possible deposited energies:

$$\int_0^\infty R_d(E_d, E_\gamma)\ \mathrm{d}E_d = \varepsilon(E_\gamma). \tag{4.11}$$

Considering an experiment in a time of flight facility, the TOF information is recorded together with the deposited energy. The $C(T_n, E_d)$ distribution of the observed time of flight is the measured quantity, where an event occurred at the TOF T_n has deposited an energy E_d in the detectors. Once defined the weighting functions as in Eq. 4.10, they can be convoluted to the count distribution $C(T_n, E_d)$, and the weighted TOF spectra is obtained integrating over the γ-ray deposited energy as:

$$C_w(T_n) = \int C(T_n, E_d)\, W(E_d)\ \mathrm{d}E_d. \tag{4.12}$$

In practice, weighting functions $W(E_d)$ are derived from a system of different Eq. 4.10 if the response functions $R_d(E_d, E_\gamma)$ are known for a number of E_γ values covering the whole energy range of interest in the studied neutron capture. Typically, the γ-ray energy range of interest in neutron capture spans from few hundred keV up to 10 MeV. In the past $W(E_d)$ were derived experimentally through careful measurement of responses of the detection system to mono-energetic γ-rays [161]. In this way, the weighting functions were determined once for each capture setup, and were supposed not to be sample-dependent. It is worth noticing that the use of a single weighting function requires a special normalization procedure with a resonance with a specific γ-ray spectrum. This is not always possible and often results in time-consuming measurements.

Despite the inaccuracy shown at the very beginning, the Monte Carlo method seems the only practical method to take into account the systematic differences of the various samples and detector arrangements. Thanks to the huge improvement of present Monte Carlo codes, it was demonstrated [162] that accurate weighting functions could be derived from simulations with current MC code such as GEANT [163] and MCNP [149] if the geometry description accurately reflects the experimental conditions. The response is obtained by a convolution of the simulated response $R(E, E_\gamma)$ with a Gaussian function, which represents the energy resolution of the detector and is studied through the

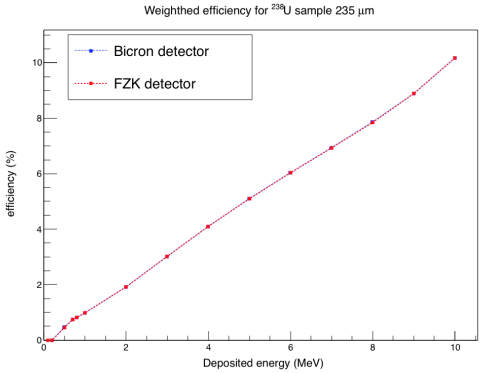

Fig. 4.4: Simulated γ-ray detection efficiency for a γ-ray homogeneous emission from a ^{238}U rectangle (235μm thick) after applying the weighting function. The detection system is the one used for this measurement, consisting of 2 C6D6 detectors placed at 90° with respect to the direction of the incoming neutron beam. As can be seen, the two different detectors have now the same efficiency, and it is directly proportional to the energy E_γ of the γ-ray.

comparison between the experimental and the simulated detector response to well-known mono-energetic γ-rays. At γ-ray energies below few of MeV standard radioactive sources, such as ^{88}Y, ^{137}Cs and Am-Be, can be used to determine the detector response. If it is needed to know the response of the detector for higher energies, (p,γ) induced reactions on light nuclei or capture γ-ray spectra for selected resonances of nuclei near closed shells can be used.

Weighting functions are obtained expressing $W(E_d)$ as a smooth polynomial function of the observed deposited energy E_d. The parameters of the function are determined by minimising the χ^2 of the least square fit of a number of γ-ray responses:

$$\chi^2 = \sum_j \left(kE_{\gamma j} - \int_{E_L}^{\infty} R_d(E_d, E_{\gamma j})\, W(E_d)\, \mathrm{d}E_d \right)^2 . \tag{4.13}$$

The lower integration limit E_L is related to experimental limitations such as the interference of noise and the use of a finite discrimination threshold E_D, which prevents to record low values of the deposited energy with a consequent loss of counts. To account for the missing part of the observed spectrum two procedures can be followed:

Lower limit = 0. The weighting functions are calculated using $E_L = 0$ MeV in Eq. 4.13. A correction is applied to take into account the missing counts coming both from γ-rays that deposited an energy below the discriminator threshold E_D and from γ-rays for which part of the response lies above the threshold. To this purpose,

tabulated transition probabilities (such as γ-rays emission spectrum) and Monte Carlo simulations are needed [162, 164].

Lower limit = E_D. The weighting functions are calculated with a finite discriminator level $E_L = E_D$ in Eq. 4.13. Weighting functions obtained in this way correct for the loss of counts due to responses lying partly above the discrimination threshold, and therefore the correction factor should take into account only for the γ-rays with an energy smaller than E_D.

For the analysis of ^{238}U(n,γ) reaction cross-section the second approach was followed. A detailed description is given is Section 5.2.2.

After applying the weighting function derived following this procedure, the efficiencies of the two different detector are proportional to the γ-ray energy, as required for the validity of Eq. 4.9 (see Figure 4.4). These two efficiencies are exactly the same thanks to the corrections for the different geometries and solid angle of the two detectors implemented in the simulations.

4.4 Neutron sensitivity

One of the main sources of background for (n,γ) measurement is related to the detection of γ-rays coming from subsequent captures of neutrons that have been scattered in the sample. This background follows the same energy dependence as the true capture events and may therefore compromise the analysis of resonances. This contribution is particularly significant for light and medium weight nuclei, but also for some heavier nuclei near to shell closure for which neutron widths in s-wave resonances can be some order of magnitude larger than capture width ($\Gamma_n/\Gamma_\gamma \sim 10^3 - 10^4$).

Clearly, for these isotopes a reliable measurement of neutron capture cross-section can be achieved only with detectors with the lowest neutron sensitivity, defined as the ratio between the detection efficiency for γ-rays coming from subsequent captures of scattered neutrons (ε_n) and for capture events (ε_γ). Detectors which owns this characteristic are typically organic scintillators, since they are mainly composed of elements with minimal neutron capture cross-sections, with the exception of hydrogen. The best choice for the scintillation material turned out to be liquid deuterated benzene (C_6D_6) [158].

In a typical neutron capture cross-section measurement, the sample-related neutron background is generated by neutrons both directly scattered towards the detectors and captured therein, and scattered randomly at the sample and then captured in other materials of the experimental hall. Neutrons detected within a time delay smaller, or at

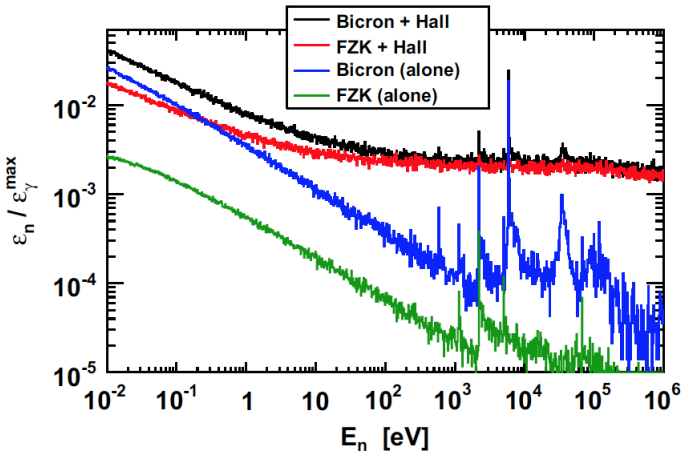

Fig. 4.5: Neutron sensitivity of Bicron and FZK C_6D_6 detectors in two configurations: detectors surrounded by the entire experimental hall (overall neutron sensitivity) and isolated detectors (intrinsic neutron sensitivity). Figure from [168].

least of the same order, of the time of flight width of the resonance of interest lead to a counting rate which is indistinguishable from that of capture events.

The background related to the neutron sensitivity is in principle easily taken into account by measuring the yield of a carbon sample. In fact ^{nat}C has a negligible capture cross-section, and therefore its measured reaction yield should purely represent the contribution of the background related to the neutron sensitivity of the experimental setup. The neutron sensitivity could also be measured as:

$$\frac{\varepsilon_n}{\varepsilon_\gamma} = \frac{C'_C}{C'_X}\frac{Y_{c,X}}{Y_{n,C}}, \tag{4.14}$$

where C'_C and C'_X indicates the net count rate for respectively the carbon and the sample measurements, $Y_{c,X}$ is the theoretical capture yield for the sample of interest and $Y_{n,C}$ the yield due to elastic neutron scattering in carbon.

However, while this procedure allows to derive the average level of neutron background, it does not provide its time structure. For this reason, Monte Carlo simulations are needed to properly determined the neutron sensitivity of the detection systems [167, 168].

In Figure 4.5 the neutron sensitivity for the C_6D_6 detection setup at the n_TOF facility is shown, derived from simulations performed with the GEANT4 simulation kit [169, 170]. The very low intrinsic neutron sensitivity of both detectors, and in particular of the optimized FZK, is clearly visible. However, when the whole experimental setup is considered the overall neutron sensitivity increases considerably for both detec-

tors, exhibiting basically the same flat behaviour above 10 eV. The average value of the neutron sensitivity over the range between 10 eV and 1 MeV results to be approximately 2×10^{-3} for both detectors.

The way to correct data for the neutron sensitivity contribution can be easily inferred from Eq. 4.5: the capture yield Y_c is in fact obtained subtracting to the measured yield the elastic one multiplied by the neutron sensitivity, that is:

$$\left(1 - e^{-n\sigma_{tot}}\right) \frac{\sigma_\gamma}{\sigma_{tot}} = Y_{obs} - \left(1 - e^{-n\sigma_{tot}}\right) \frac{\varepsilon_n}{\varepsilon_\gamma} \frac{\sigma_n}{\sigma_{tot}}. \tag{4.15}$$

However, it is important to consider that from the adopted definition the neutron sensitivity represents the detector response to neutrons of a given energy, not at the energy reconstructed from the neutron time of flight. For this reason, the most reliable way to obtain a realistic estimate of the background related to the neutron sensitivity of the experimental setup with its time dependence is to perform complete simulations, including the specific sample and the exact energy distribution of the neutron fluence. This is the approach followed in this work, and will be analyzed in detail in Section 5.4.2.

4.5 Summary

The experimental methods to measure neutron induced capture cross-sections have been here presented, and both the measurement principles and the detection setups have been described. Particular attention has been paid to the detection systems in use at the n_TOF facility, i.e. the total absorption detection, with the use of the Total Absorption Calorimeter (TAC), and the total energy detection, which exploits two C_6D_6 scintillators. This last technique is the one used to analyze the measurement of this work, and has the great advantage to minimize as possible the background induced by scattered neutrons, which is, as explained, one of the main sources of background for (n,γ) measurement.

Chapter 5
^{238}U(n,γ) measurement with C_6D_6: data reduction

A high precise and accurate measurement of ^{238}U(n,γ) reaction cross-section has been performed in April 2012 at the CERN n_TOF facility using C_6D_6 scintillation detectors over an energy range from thermal to 1 MeV. The goal of this measurement (part of a larger proposal) is to provide a cross section as precise as possible in order to reach, together with other measurements, an uncertainty of 2%. The data reduction, i.e. the analysis procedure from raw data to capture yield, is here described in detail, with particular emphasis on the background subtraction.

5.1 Experimental campaign

The experimental campaign for the measurement of ^{238}U(n,γ) reaction cross-section using C_6D_6 scintillators took place during April 2012 and lasted for 35 days. During this period, the proton current was monitored with the pick-up detector system based on the wall current monitor (WCM) of the CERN Proton Synchrotron. In addition, the subsequent neutron beam was monitored at the experimental area with the SiMON detector. The C_6D_6 scintillator performances were controlled on a weekly basis.

Together with ^{238}U(n,γ), it was necessary to perform some auxiliary measurements to accurately characterize the background and to validate the analysis procedure.

- In order to correct for time-dependent background, induced by the neutron beam, measurements were carried out without samples in the beam (hereafter is referred to as Empty-Frame or Sample-Out measurements).
- Beam off measurements were carried out to characterize the room background and the activity of the sample and air.
- To validate the entire analysis procedure, ^{197}Au(n,γ) reaction cross-section measurement was carried out with a sample similar to ^{238}U.

Table 5.1: Details of time allocation for the ^{238}U experiment.

	No filters		With filters	
Sample	# Protons	Running time	# Protons	Running time
^{238}U	7.85×10^{17}	10 days	7.02×10^{17}	7 days
Sample Out	6.271×10^{16}	6 days	1.64×10^{17}	3 days
^{238}U packing	9.65×10^{16}	2 days		
Beam Off		0.25 days		
Calibrations		0.25 days		
^{nat}Pb	1.50×10^{17}	2 days	1.53×10^{17}	2 days
^{197}Au (300μm)	8.33×10^{16}	2 days	9.93×10^{16}	2 days
^{197}Au (50μm)	4.86×10^{16}	2 days		
^{nat}C (5 mm)	1.46×10^{17}	3 days	1.66×10^{17}	2 days
^{nat}C (10 mm)	9.71×10^{16}	3 days	1.11×10^{17}	3 days

- Measurements with a C sample were performed, as carbon is a pure neutron scatterer ($\sigma_n \gg \sigma_\gamma$) and therefore can be used to estimate the background due to scattered neutrons from the ^{238}U sample.
- A natural Pb sample, with the same area as the ^{238}U one, was used to evaluate the counts due to in-beam γ rays that Compton scatter on the sample. Lead was also chosen since it has a similar atomic number Z to uranium and a negligible capture cross-section.
- Runs with black-resonance filters were performed to determine the energy dependence of the background. A black resonance, by definition, removes all the neutrons from the beam so that all the counts left can be only related to background. More details about this technique can be found in Appendix B.

In Table 5.1 the different measurements, together with the time dedicated are summarized.

5.1.1 Samples

The ^{238}U sample was provided by the EC-JRC-IRMM laboratory (GELINA [66]). From an isotopic analysis, done in 1984, it resulted to be an extremely pure 6.125(2)-gram metal plate, containing less than 1 ppm of ^{234}U, about 11 ppm of ^{235}U and less than 1 ppm of ^{236}U.

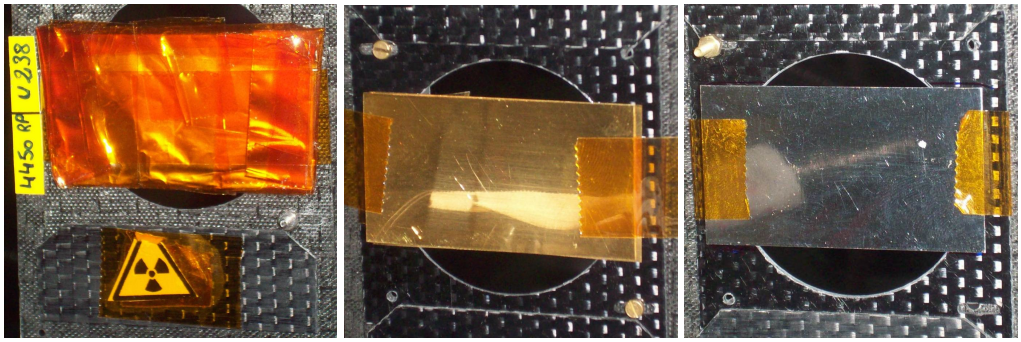

Fig. 5.1: Pictures of the ^{238}U (left), ^{197}Au (center) and ^{nat}Pb (right) sample used during the experimental campaign.

Table 5.2: Characteristics of the samples.

Sample	Size (mm)	Mass (g)	Atomic density (atoms/barn)
^{238}U	53.80×30.02	6.125 ± 0.002	$(9.64 \pm 0.04)10^{-4}$
^{nat}Pb	53.77×30.19	9.44	1.725×10^{-3}
^{197}Au	53.30×29.65	9.213	1.773×10^{-3}
^{197}Au	53.30×29.65	1.547	2.9×10^{-4}
^{nat}C	53.35×30.20	28.89	8.94×10^{-2}
^{nat}C	53.35×30.20	14.638	4.49×10^{-2}

The sample is rectangular in shape, 53.80 mm × 30.02 mm, and covered 97% of the neutron beam. To comply with CERN radio protection regulations, the sample was encased in $\sim$ 60 μm of aluminum foil and $\sim$ 75 μm of Kapton foil. The effects of this canning has been studied during the measurement campaign and resulted to be negligible.

All the samples were mounted in a remote-controlled strip, built in carbon fiber.

In order to cover the same fraction of neutron beam, the samples used in this experimental campaign have been chosen with the same geometry, as can be seen in Figure 5.1. In Table 5.2 the main features of the samples are listed.

5.1.2 Stability of the detection systems

The stability of the apparatus was monitored, both for the flux and the capture detectors. Concerning the neutron flux stability, we investigated the ratios between the hits registered by the silicon monitors and the number of protons derived from the current measurement from the pick-up signal. We selected only those runs where the ratios be-

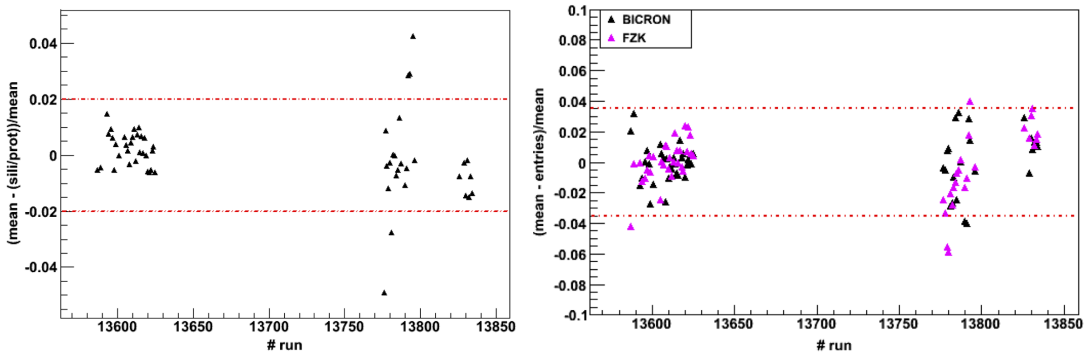

Fig. 5.2: Left: Percentage difference between the hits registered by the silicon monitors and the proton current derived from the pick-up signal. The ±3.5% level is shown with the red dotted lines. Right: Percentage deviation of the number of entries per run (normalized to the number of protons) from the mean value, for Bicron (black) and FZK (magenta) detectors. The ±3.5% level is indicated with the red dotted lines.

tween the number of incident particles deviated by no more than 3.5% (see left panel of Figure 5.2).

Moreover, the stability of the two C_6D_6 detectors was investigated by selecting the capture events corresponding to the first saturated resonances in ^{238}U (the same procedure was adopted for ^{197}Au measurement) and recording the number of counts registered by the detectors normalized to the number of protons. The number of events per run recorded with the gold sample in beam deviates from the mean value by only 0.6% for the FZK and by 1% for the BICRON detector (therefore all the runs are considered reliable and included in the analysis). The large number of ^{238}U runs needed a more accurate analysis, because they span over the entire duration of the campaign. In fact, we found that the normalized number of entries per run deviates by about 6% from the mean value, a percentage too big to be acceptable for our analysis. To reduce the dispersion of the data set, we rejected those runs with percentage deviations greater than 3.5% (see right panel of Figure 5.2). With this constraint the distribution of the percentage deviation resulted to be less than 2% for 90% of the runs. By applying these conditions we rejected in total 1.5% of the data from the BICRON and 5% for the FZK detector, not significantly affecting the statistics of the measurement.

5.2 Operation and performance of the C_6D_6 scintillators

As described in Section 4.3.2 the experimental setup for the ^{238}U(n,γ) reaction measurement consisted of two deuterated benzene scintillators, opposite each other at 90° with

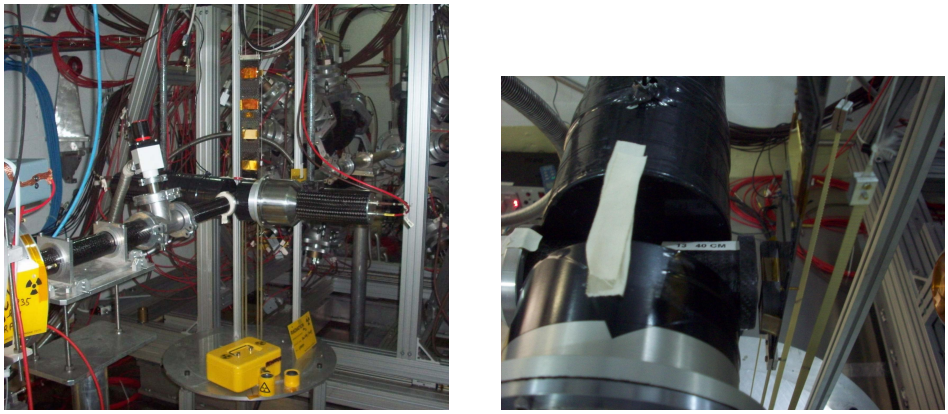

Fig. 5.3: Pictrues of the detection setup. Bicron scintillator is on the left and FZK on the right. The sample exchanger is visible in between the two detectors.

respect to the beam, 9 mm away from the sample: one commercial (Bicron) and one custom made (FZK) [160]. In Figure 5.3 pictures of the experimental setup are shown.

The geometry of the detection system covered a small solid angle, so to approach the Total Energy Technique requirement, i.e. only one γ ray per capture event is detected by the detection system. To completely fulfil the requirement, during the offline data reduction a time window of 30 ns has been fixed to exclude events recorded in coincidence.

5.2.1 Energy calibration and resolution

In order to be as precise as possible, an accurate study of the calibrations between the flash-ADC channels and the deposited energy was performed on a weekly basis using three standard γ-ray sources: ^{137}Cs (661.7 keV), ^{88}Y (898 keV and 1.836 MeV) and Am/Be (4.44 MeV). This procedure is also important to check the stability of the detectors over the whole campaign. Comparing the different calibration spectra for each source we actually noticed a small variation of the gain, which was adjusted by applying different calibration curves as can be seen in Figure 5.4. Even if the differences are of the order of few percent, a proper correction is important, since the Total Energy Technique is sensitive to the amplitude spectrum. Therefore we extracted six calibration lines from the different calibration runs. After these calibrations are applied the spectra resulted perfectly aligned (see the right panel of Figure 5.4).

The peaks in the amplitude spectra, corresponding to the well known Compton edge of the different γ rays emitted by the sources, are broadened by the detector resolution.

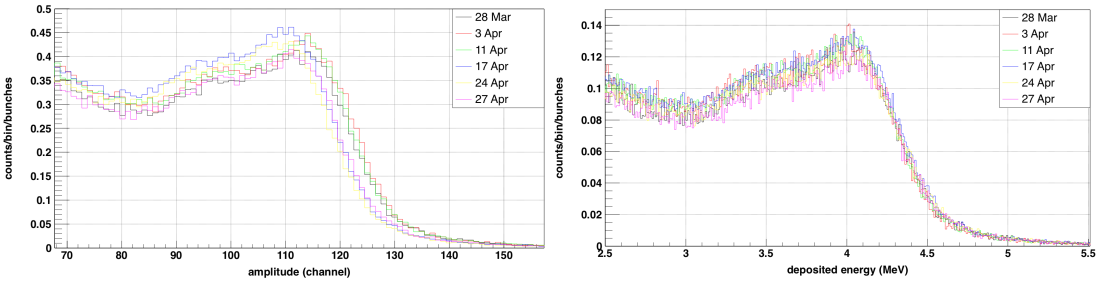

Fig. 5.4: Amplitude spectra for the Am-Be source: on the left as a function of flash-ADC channels, on the right as a function of deposited energy after the application of the different calibration lines. It is clearly visible that with this method we manage to achieve the stability of the performances of the detectors.

Extracting the channel numbers associated to these peaks we calibrated the flash-ADC channels. In particular, the observed peaks have been analyzed with the software package ROOT [171] and fitted with a Gaussian function:

$$f(x) = A\, \mathrm{e}^{-\frac{(x-\mu)^2}{2\sigma^2}}, \tag{5.1}$$

where A is the amplitude and μ the mean value related to the Compton edge of the γ ray. The best-fit curve was found through the minimization of the χ^2. In Figure 5.5 the amplitude spectra for Bicron detector corresponding to the three different γ ray sources are shown together with the Gaussian best-fit curves. For both detectors a small non-linearity has been observed in the energy calibration, and therefore a second order polynomial was used to fit the four energy points.

From calibration measurements we can identify the energy resolution (ΔE) of the detectors, which corresponds to the full width at half maximum of the gaussian distribution (FWHM$= 2\sqrt{2\ln 2}\ \sigma$). An accurate determination of the energy resolution is needed to broaden the results of the simulations concerning the detection system, which by themselves account only for the broadening due to physical processes not including the electronic one.

Bicron detector is characterized by a relative energy resolution $\Delta E/E \sim 15\%$ at 662 keV and $\Delta E/E \sim 5.2\%$ at 4.4 MeV, while FZK detector has $\Delta E/E \sim 21\%$ at 662 keV and $\Delta E/E \sim 7.5\%$ at 4.4 MeV[1]. In the bottom right panel of Figure 5.5 the amplitude spectrum of ^{88}Y is shown together with the simulation before and after applying the energy resolution broadening.

Thanks to the accurate flash-ADC channel to energy calibration, it was possible to properly choose the thresholds in deposited energy so to exclude as much background

[1] The scintillation liquid volume in Bicron detector is about 3/4 with respect of the FZK one.

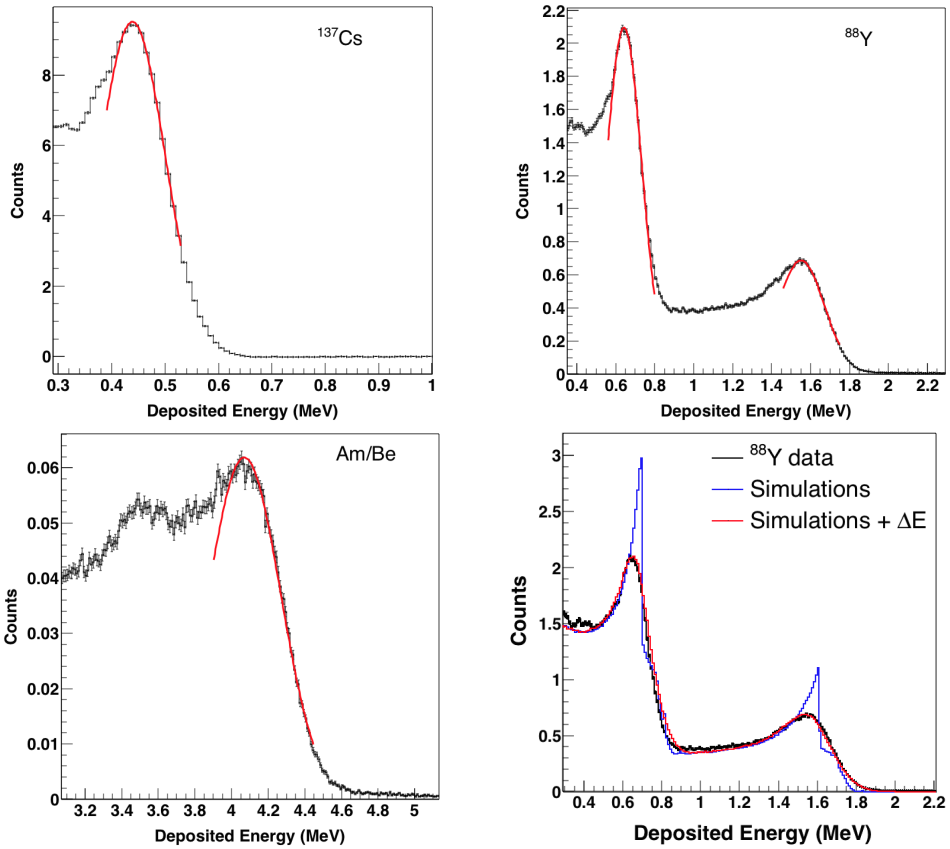

Fig. 5.5: Calibrated amplitude spectra for ^{137}Cs (661.7 keV), ^{88}Y (898 keV and 1.836 MeV) and Am/Be (4.44 MeV) γ-ray sources. The red lines correspond to the Gaussian fit. In the bottom right panel, the ^{88}Y spectrum is shown together with the simulations, before (blue) and after (red) applying the broadening due to energy resolution.

counts as possible not affecting too much the statistic. For this measurement the threshold have been chosen to be $E_{\text{dep}}^{\text{min}} = 0.250$ MeV and $E_{\text{dep}}^{\text{max}} = 5.53$, corresponding to γ-ray energies of $E_\gamma = 407$ keV and $E_\gamma = 5.77$ MeV respectively. The higher threshold corresponds to the neutron separation energy of the ^{239}U nucleus, $S_n = 4.806$ MeV, to which a 15% resolution is added.

5.2.2 Weighting functions

As already mentioned, the detection technique used within this measurement was the Total Energy Technique. As explained in Section 4.3.2, it requires the determination of the so-called weighting function in order to satisfy the required proportionality between

Fig. 5.6: Experimental setup as implemented in GEANT4 geometry files. Together with the detector the sample holder, the supports and the beam line are included.

detection efficiency and the deposited energy. To this end, a very accurate knowledge of detector response for different γ-ray energies is required. This response depends on γ rays transportation both in the detection system and within the sample itself, and it has been simulated by means of GEANT4 [169] Monte Carlo code (see Figure 5.6 and 5.7). In these simulations, the γ rays are emitted randomly within the sample following the gaussian xy-distribution of the neutron beam profile, being z the direction of the neutron beam. Figure 5.6 shows a three dimensional view of the experimental setup as modelled in GEANT4 geometry file. In the description of the detection system not only the active volume, but also the other components of the detectors, such as the boron free quartz window, the Al or carbon fiber chamber and the photomultiplier are implemented. In addition, the sample exchanger and the carbon-fiber beam line were implemented as well. The detector responses are collected separately, and two different weighting functions were calculated.

The polynomial dependence of the weighting function W on the energy deposited by γ rays is determined by a least-squares fit to a number of γ-ray responses in the energy range of interest, i.e. from 100 keV up to 10 MeV:

$$\min \sum_j \left(\sum_i W_i R_{ij} - k E_{\gamma j} \right)^2 , \tag{5.2}$$

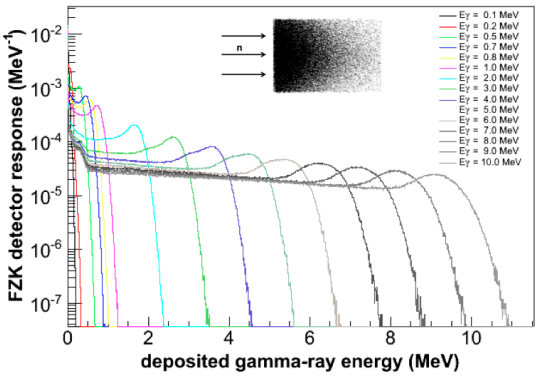

Fig. 5.7: Simulated response of the FZK detector for different mono-energetic γ rays considering an exponential attenuation of γs inside the sample (see text for details). The response has been convoluted with the energy resolution of the detector.

where the proportionality constant k is taken equal to 1 MeV^{-1}, and the index j indicates the energy bin. As described in the PHWT paragraph of Section 4.3.2, because of experimental limitations it is necessary to put a threshold (250 keV for both detectors) in the calculation of the weighting functions to account for the missing low-energy part of the observed spectrum.

The effects of neutron transportation within the sample becomes significant only when the product $n\sigma_{\mathrm{tot}} > 1$, where n indicates the areal density in atoms/barn and σ_{tot} is the total cross section. In the present case, where the a ^{238}U sample has an areal density $n = 9.56 \times 10^{-4}$ atoms/barn, this condition is fulfilled only in correspondence of the peak-energy of the first 3 s-wave resonances. For this reason we produced two different weighting functions: one considering an homogeneous distribution in the z-direction of the γ-ray initial positions within the sample, while in the other case an exponential attenuation was assumed. The first case is used for the resonance shape analysis (RSA) and the analysis of the unresolved resonance region, while the second one is applied for the extraction of the normalization factor through the saturated resonance technique (see Section 5.5).

The quality of the fitted weighting function was evaluated through the calculation for each simulated response to monoenergetic γ rays with an energy E_γ of the quantity Q, defined as:

$$Q = \frac{\sum_i W_i R_{ij}}{E_{\gamma j}}, \tag{5.3}$$

which has an expected value of 1. In Figure 5.8 the weighting functions for the detection system of Figure 5.6 for exponential attenuation and homogeneous emission of monoen-

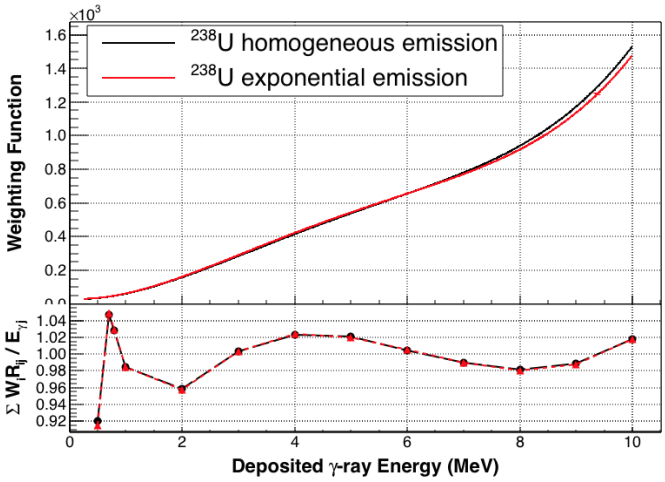

Fig. 5.8: Weighting functions for γ ray emission from the ^{238}U with an homogeneous z-distribution (black) and an exponential attenuation in the z-direction (red). The bottom panel shows the verification of the proportionality of the weighting functions plotting the ratio Q defined in Eq. 5.3 as a function of the deposited energy.

ergetic γ rays are compared. In the bottom panel the quantity Q is plotted to verify the quality of the weighting function.

Within this work, the weighting functions found for the ^{238}U sample are used to weight the ^{238}U(n,γ) and the background counting rate.

5.3 Capture Yield extraction

The experimental capture yield was extracted dividing the weighted counts C_w, calculated as in Eq. 4.12 after a time-to-energy conversion, by the incident neutron fluence ϕ_n, as in Eq. 4.2:

$$Y_{exp}(E_n) = N\frac{C_w(E_n)}{\phi_n(E_n)}. \tag{5.4}$$

Weighting the counts via the PHWT, so to achieve the proportionality between deposited energy and detection efficiency, means also to take into account the efficiency $\varepsilon_{n,\gamma}$ of the two C_6D_6 to detect a capture event. Therefore the normalization factor N takes into account the effective area of the ^{238}U sample intercepted by the neutron beam, which is $\sim$ 97%, the efficiency loss that could not be included in the simulations and the absolute value of the evaluated flux. As will be explained in Section 5.5, N has been determined through the saturated resonance method [165].

5.3.1 Time-to-energy calibration

The time-to-energy relation for this measurement was studied accordingly to the procedure described in Ref. [124]. As described in Section 3.2.1, at n_TOF the effective flight path is influenced by the time traveled by neutrons within the spallation target and the moderator, resulting in an additional distance ΔL to be added to the geometrical flight path L_0. It is demonstrated (see Ref. [124]) that at the n_TOF facility ΔL varies with the square root of the neutron energy, fact that allows us to express the energy-dependent term of the flight path in terms of a fixed, experimentally determined time offset t_0: $\Delta L = -t_0 \times \sqrt{E_n}/72.2983$. Eq. 3.5 becomes therefore:

$$E_n = \left(722.983 \frac{L_0}{t + t_0}\right)^2, \tag{5.5}$$

where E_n is expressed in eV, L_0 in cm and t and t_0 in ns. The reconstructed time of flight $t = t_m - t_{\gamma-\text{flash}}$ is provided from the Pulse Shape Analysis routine.

Since the expected energy dependence of the flight path starts becoming significant only above a few keV, in order to determine the values of the energy-independent term L_0, a function given by Eq. 5.5 has been fitted to the data from specific ^{238}U resonances with well-known energies. We selected the the first four ^{238}U(n,γ) resonances, which are considered well-known [173], plus three resonances at energies around hundreds of eV. The time-of-flight of the resonances is determined as the mean value of the best-fit gaussian curve which represents the data, and they have been associated to the corresponding resonance energies tabulated in ENDF/B-VII.1 library. The flight-path fit is shown in Figure 5.9 and it gives as result $L_0 = 184.24 \pm 0.02$ cm for both detectors. Because at higher energies no standard energy references are available, this procedure cannot be

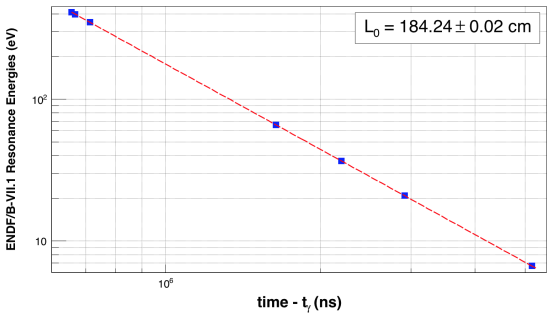

Fig. 5.9: Resonance energies from ENDF/B-VII.1 library as a function of neutron time of flight as provided from the Pulse Shape Analysis routine for the ^{238}U(n,γ) measurement. The fit of a function given by Eq. 5.5 is shown as a red line. In this low energy range the time-to-energy calibration is sensitive only to the geometrical distance L_0, which is found to be $L_0 = 184.24 \pm 0.02$ cm.

followed to find the time offset t_0. For this reason, we analyzed resonances from 500 eV to 1 keV using the R-matrix code SAMMY. The results gives $t_0 = -41 \pm 13$ ns.

5.3.2 Neutron flux

In Section 3.4.1 the n_TOF neutron flux for the first experimental area has been presented. As described, after combining together the results of five different detectors an evaluated flux has been released in Ref. [151] for three years of the n_TOF Phase-2, i.e. 2009, 2010 and 2011. For 2012 measurement campaigns not all these detector were available, but the neutron flux has been constantly monitored using the SiMON detector [135].

In Figure 5.10 the flux extracted from silicon monitor measurements in 2012 is compared to the evaluated flux for year 2011. From this comparison it firstly results that the boron content in the moderator changes year after year, in particular it increased from 2011 to 2012. Secondly, it shows up that in the 2012 measurement campaign the neutron intensity seems about 13% lower than in the past, unless a loss of efficiency occurred, possibly due to a change of the position of the SiMON detector or to a degeneration of the ^{6}Li converter foil. However, between 0.1 eV and 150 keV (the maximum energy to which the Silicon Monitor could be used, see Table 3.2) the ratio between the flux in 2012 and the evaluated flux in 2011 shows that the shapes mostly agrees within 2% apart from fluctuations at energies corresponding to dips due to in-beam material (such as Al

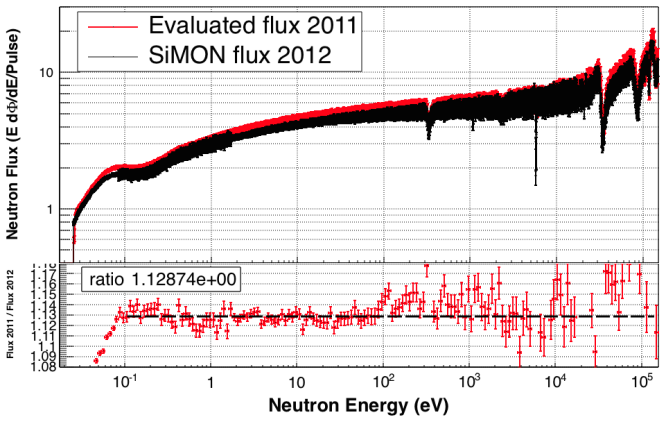

Fig. 5.10: n_TOF neutron flux in 2012 (black) compared with the 2011 evaluated flux. In the bottom panel the ratio 2011/2012 shows a $\sim$ 13% decrease of the neutron intensity in 2012, but a constant behaviour in shape between the two years starting from 0.1 eV. The deviation at lower energies is due to a change in the boron content in the moderator.

and Mn). This constant behaviour allows us to use the 2011 evaluated flux to extract the yield for the ^{238}U(n,γ) measurement starting from 0.1 eV neutron energy. The different intensity is taken into account in the normalization procedure, which will be explained in Section 5.5.

5.4 Background subtraction

The dead-time corrected spectra were evaluated as precisely as possible, and to determine the background which affected the ^{238}U(n,γ) measurement several contributions have been identified.

Beam Off background. It is the only time independent source of background and takes into account natural radioactivity and air activation. By definition, it can be evaluated measuring the counts detected by scintillators when the beam is off. This contribution turned out to be sensitive to the position of the sample in the sample exchanger, and for this reason different measurements have been performed corresponding to each position of the sample exchanger.

Sample Out background. This contribution is measured with the beam on but without samples in the beam, and it counts all the sources of background present in the experimental area not related to the sample itself. We studied also if the canning of the sample, made of Al and kapton, affected the background of the measurement, and their contribution was found to be negligible.

In-beam γ rays. This background is due to γ rays travelling along the neutron beam and detected by scintillators after Compton scattering or pair production on the sample. These two processes have cross sections that depends on Z and Z^2 respectively, and therefore to evaluate this contribution a measurement on a sample with a negligible capture cross-section and a charge number as similar as possible to uranium was needed. To this purpose a ^{nat}Pb sample was used.

Scattered neutrons. It is a sample-related neutron background and depends on the neutron sensitivity of the detectors, which has been introduced in Section 4.4. As outlined, neutrons scattered by the sample can in fact be later captured, or undergo inelastic reactions in the material of the detector and experimental area. γ-rays produced in this way cannot be distinguished from capture events in the sample. Our C_6D_6 scintillators are optimized to minimize this source of background, which could be very significative because of the magnitude of elastic cross section with respect to the capture one. We studied the contribution of scattered-neutron background both

measuring a ^{nat}C sample, which has a negligible capture cross-section with respect to the elastic one, and through dedicated Monte Carlo GEANT4 simulations.

Two independent methods have been followed to evaluate and subtract the background of ^{238}U(n,γ) measurement. (*i*) In the first method the time dependent background has been evaluated studying the ^{nat}Pb contribution, which contains the sample out background as well as the one related to in-beam γ rays and scattered neutrons. The shape of the resulting background has been properly scaled to uranium by taking advantages of measurements with black resonance filters. The beam off contribution, measured at the U sample position, was added in order to obtain the complete background function. (*ii*) In the second method we evaluated each single background components listed above using experimental measurements combined to GEANT4 simulations. From now on, the two methods are called filter-scaled and measured background, respectively.

It is important to remark that the analyses of background were carried out separately for the two detectors, although to avoid superabundance not all the plots are presented for both.

5.4.1 Filter-scaling background evaluation method

As outlined before, the n+^{nat}Pb measurement has been used to evaluate the shape of the time-dependent background, which contains the sample out, the in-beam γ rays and the scattered neutrons backgrounds. Moreover, in order to avoid the statistical fluctuations its shape was fitted with an analytical function based on a sum of parametrized exponentials.

As a first step, we subtracted the beam off contribution sample by sample, and then we fitted the contribution of the ^{nat}Pb sample with and without filters in beam. The use of black resonance filters (see Table 5.3) helped us to properly scale the lead contribution to uranium background level, following the procedure explained hereafter. Once found the scale factor, we added the contribution of beam off background measured at the U sample position in order to obtain the complete function for ^{238}U(n,γ) background.

In Figure 5.11 the weighted counts as function of neutron time of flight are shown for Bicron detector, both without (left panel) and with (right panel) black filters in-beam.

To subtract the time independent background it is convenient to look at the weighted counts divided for the binwidth as a function of TOF, so that the independence of the beam off background from the TOF is made explicit. For this reason, a constant function

Table 5.3: Black resonance filters used to evaluate the level of ^{238}U(n,γ) background.

Filter	Black-resonance Energy (eV)	Black-resonance TOF (ns)	Thickness (mm)
Ag	5.19	5.846×10^6	0.5
W	18.8	2.902×10^6	0.8
Co	132.0	1.159×10^6	0.25
Al	34.83×10^3	7.136×10^4	110
	86.27×10^3	4.534×10^4	

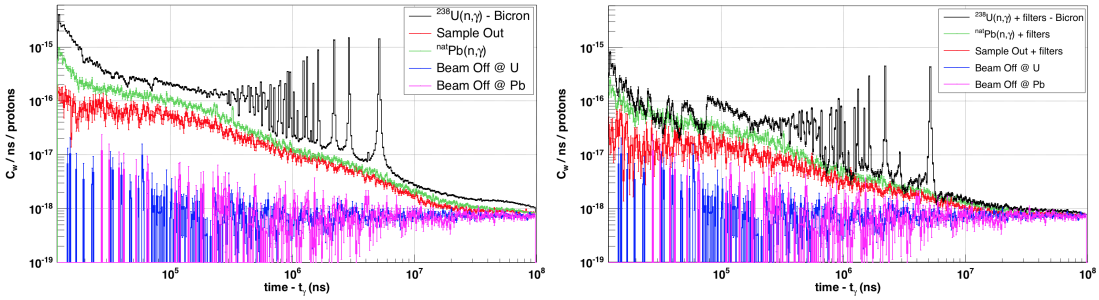

Fig. 5.11: TOF weighted counts recorded with Bicron detector (right) and when all filters (Ag, W, Co, Al) are present in beam (left). Counts are divided for the binwidth and normalized to the number of protons.

which represents its contribution can be simply found, avoiding in that way fluctuations due to counting statistic.

After the beam off background subtraction we used a sum of six parametrized exponentials to reproduce the $^{\text{nat}}$Pb contribution:

$$Pb(t) = A\, e^{Bt} + C\, e^{Dt} + E\, e^{Ft} + G\, e^{Ht} + I\, e^{J(t+1.e7)} + K\, e^{L(t+1.e7)} + M. \qquad (5.6)$$

The parameters have been obtained fitting the n+$^{\text{nat}}$Pb counts for both detectors. In Figure 5.12 the comparison between experimental data and the function in Eq. 5.6 with proper parameters is shown together with the residuals.

As previously outlined, we determined the level of the background with the help of measurements with black resonance filters in beam. The quantity of in-beam material needed to this aim, however, is not negligible and attenuates both the neutron beam and the in-beam photons. For this reason, a scaling procedure is needed to properly reproduce the background present during the measurement. In this work we followed the procedure introduced by Aerts *et al.* [172] for the analysis of the capture cross-section of ^{232}Th in the unresolved resonance region.

We firstly scaled the Pb contribution with filters in the beam to the U measurement, by multiplying it for the ratio $\text{U}_F(\text{Al}_{35keV})/\text{Pb}_F(\text{Al}_{35keV})$, where $\text{U}_F(\text{Al}_{35keV})$

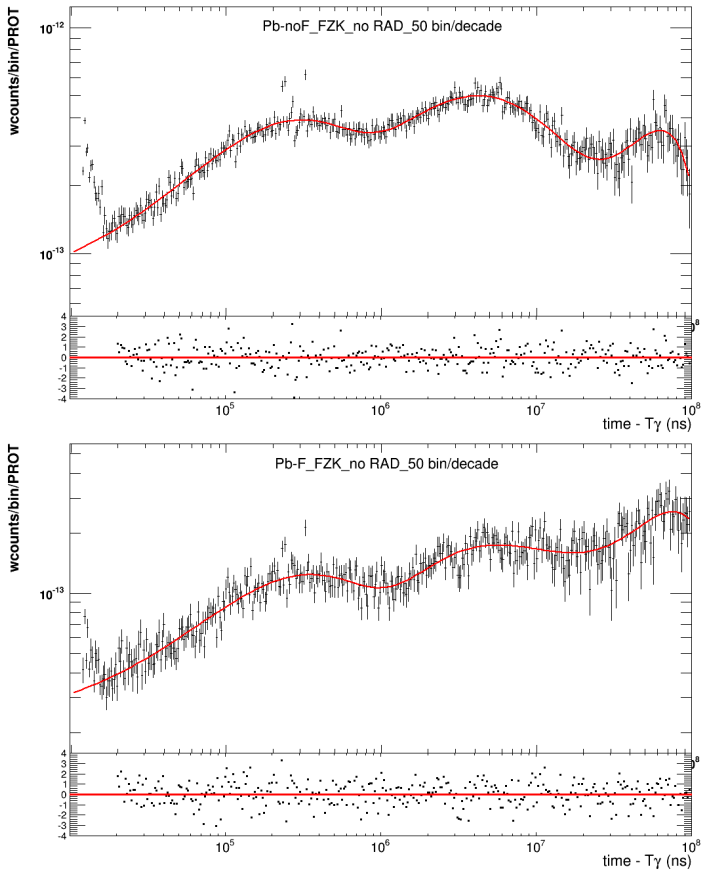

Fig. 5.12: Fit of the lead contribution without (left) and with (right) filters in beam. Counts are intended as counts per bin using 50 bins/decade, and normalized to the number of protons.

and $\mathrm{Pb}_F(\mathrm{Al}_{35keV})$ are the number of counts at the Al dip observed in uranium and lead spectrum with all filters in beam. Afterwards, the function that reproduces the total n+^{238}U background is found using:

$$B(t) = a\, t^b + \frac{k_1}{k_2(t)}\, Pb(t), \tag{5.7}$$

where to ease the fitting procedure the weighted counts are not divided for the binwidth.

Here, the first power function reproduce the beam off background at the ^{238}U sample position, and the values of a and b are obtained fitting the beam off background. The $k_2(t)$ factor represents the ratio between lead contributions with and without filters, i.e. $k_2(t) = Pb_F(t)/Pb(t)$, where Pb_F and Pb has the structure of Equation 5.6. Because of the influence of the black-resonance filters, this ratio has a time dependence which must be taken into account. The last factor k_1 is deputed to scale the contribution of Pb

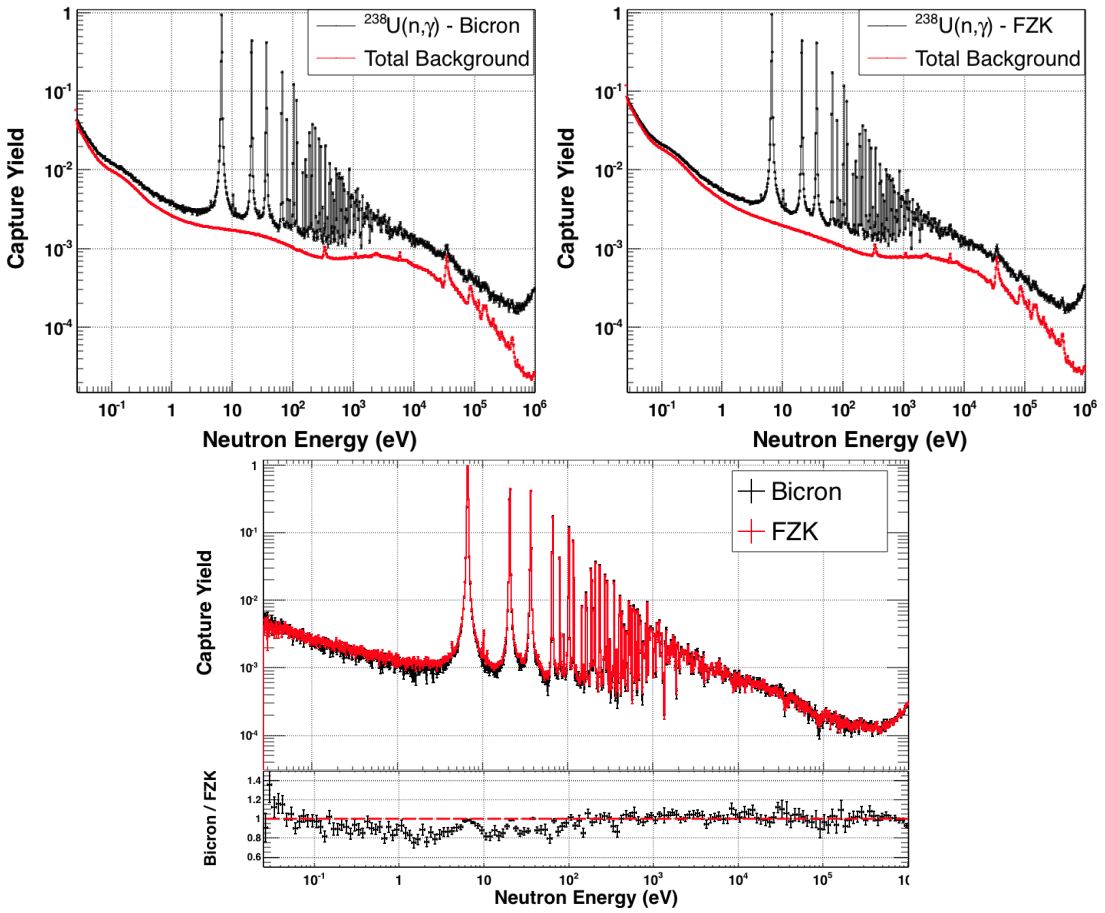

Fig. 5.13: Capture yields are shown in black for Bicron (upper left panel) and FZK (upper right panel) detectors, compared with the total background (red line) obtained via the filter-scaling procedure. In the bottom panel the comparison between the two background-free yields is shown. The agreement is very good from 100 eV up to 1 Mev, while at low energies one can clearly distinguish in the ratio some inconsistencies corresponding to the valley of the resonances, probably due to a residual background present in FZK detector.

without any filters to the ^{238}U with filters in. To do this, we averaged the ratios between Aluminum dips values in ^{238}U with filters and Pb without:

$$k_1 = \frac{1}{2}\left(\frac{U_F(Al_{35keV})}{Pb(Al_{35keV})} + \frac{U_F(Al_{86keV})}{Pb(Al_{86keV})}\right). \tag{5.8}$$

Once found these coefficients, it was possible to determine a function which represents the total background for ^{238}U(n,γ) measurement. The uncertainty related to this function is 5%. In Figure 5.13 the yield with the total background is shown for both detectors. In the bottom panel the comparison between the normalized, background-free capture

yields points out the good agreement between the results obtained with the two detectors separately, with the exception of the resonance valleys at $E_n < 100$ eV, probably due to some residual background in FZK detector. However, this background was fitted with the R-matrix code SAMMY.

5.4.2 Single background-component evaluation method

To evaluate the background level, together with the filter-scaling method we followed a second independent method, studying separately the contribution of each source of background.

The beam off and sample out backgrounds have been determined through experimental measurements. As we outlined above, the beam off background contribution depends on the sample position in the sample exchanger. In particular, the sample out measurement has been carried out in the position of the sample exchanger below the uranium sample. Therefore, to find the proper background for the uranium sample, we subtracted to the sample out background the corresponding beam off contribution and we afterwards added to it the beam off background measured at the uranium sample position. In order to avoid statistical fluctuations, the resulting shape has been fitted with a function as in Eq. 5.6 to find the proper parameters. The uncertainty of the fit was 5%.

The background contribution originated from sample-scattered neutrons is an important component of the background. In fact it follows the same energy dependence as the capture events, being completely undistinguishable. Usually, at n_TOF we used to evaluate the contribution related to the neutron sensitivity of the detection system through ^{nat}C measurement. Since natural carbon can be considered as a pure scatterer (being its capture cross-section negligible) all the counts detected by the scintillators are due to scattered neutrons. Once extracted the carbon yield, it is scaled to take into account the different areal density n and elastic cross sections σ_n between ^{nat}C and ^{238}U samples:

$$Y_n^{\mathrm{U}} = \frac{n_{\mathrm{U}}}{n_{\mathrm{C}}} \frac{\sigma_n^{\mathrm{U}}}{\sigma_n^{\mathrm{C}}} Y^{\mathrm{C}}. \tag{5.9}$$

Recent studies from Žugec *et al.*, however, demonstrated that this method is unsatisfactory to proper determined the background component due to scattered neutrons. In Ref. [168] is demonstrated that the high-energy part of the neutron beam induces reactions whose products have an effect in the low energy ($E_n \lesssim 100$ eV) region of the capture yield. Therefore, GEANT4 simulations have been performed so to understand and estimate the scattered neutron background. In the simulation, the complete geom-

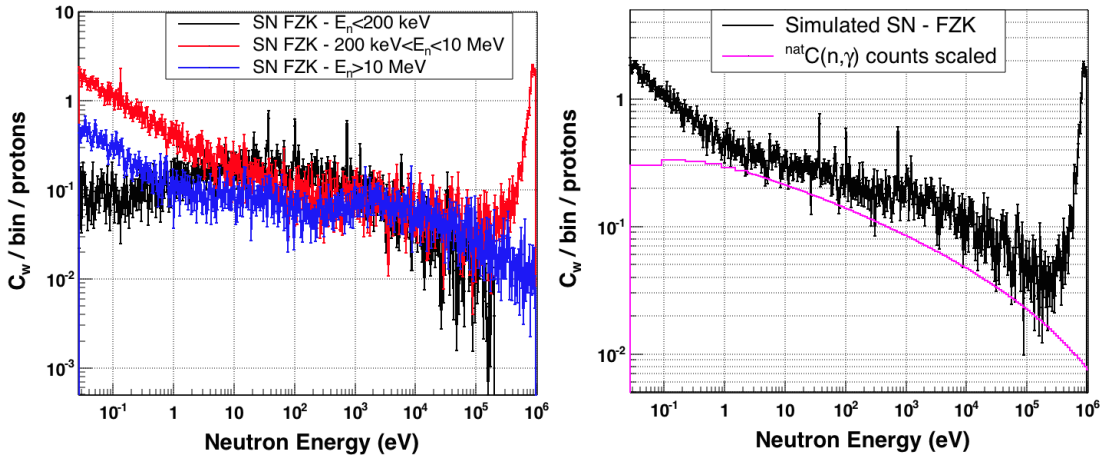

Fig. 5.14: Scattered-neutron background obtained from GEANT4 simulations for the FZK detector. The counts are weighted with the ^{238}U weighting function, and normalized to the number of protons. The left panel shows the contribution from different energy regions of the incident neutron beam, while in the left panel the total background determined with simulations is compared with the one determine through n+$^{\text{nat}}$C measurement.

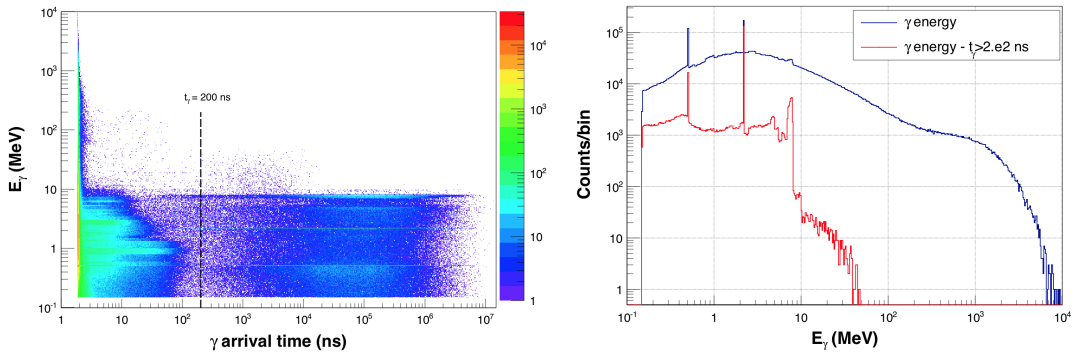

Fig. 5.15: Initial in-beam γ-rays energy distribution as simulated with the Monte Carlo code FLUKA (right) and as a function of the arrival time of γ-rays in the experimental area (left). The effects of the γ-flash are excluded with a condition in the arrival time $t_\gamma > 200$ ns. The two clearly visible lines in the spectrum corresponds to the 480-keV γ rays coming from the n+^{10}B reaction and the 2.2 MeV γ rays from the deuterium formation.

etry of EAR-1 for the ^{238}U(n,γ) measurement was implemented, and a particular care was put to validate the reliability of the γ-ray cascades generated within GEANT4 in the neutron capture reaction. All the details can be found in Ref. [168]. The output of the simulation has been analyzed with the same conditions of the experimental data. In particular, we applied the weighting functions with homogenous emission, and the same normalization factor and time-to-energy calibration. In Figure 5.14 the scattered neutron

background obtained from GEANT4 simulations is shown for FZK detector. In the left panel the contribution from three different energy regions of the incident neutron beam can be seen. From the figure it is clear that the high energy part of the incident neutron beam ($E_n > 200$ keV) significantly contributes to the scattered neutron background at low energies. The right panel shows the comparison between the total scattered neutron background obtained with simulations and the one estimated scaling the carbon yield with Eq. 5.9. It results that the simple n+^{nat}C measurement underestimates the scattered neutron background, in particular not taking into account the contribution due to the high-energy incident neutrons.

The shape of the background due to in-beam γ rays is given by n+^{nat}Pb measurement once subtracted by beam off and sample out contributions. To take into account the difference in areal density between uranium and lead sample, as well as the different charge number Z, GEANT4 Monte Carlo simulations have been performed, using the same geometry implemented to determine the detector responses for the weighting functions calculation (see Figure 5.6). The initial in-beam γ-rays distribution has been provided from Monte Carlo FLUKA [146] simulations, and we put a condition on the arrival time of γ rays $t_\gamma > 200$ ns to eliminate signal from the γ-flash (see Figure 5.15). The output of the GEANT4 simulations gives the deposited energy in the two detectors when a γ ray impinges on the uranium or on the lead sample. We weighted the counts using the weighting functions obtained with homogeneous γ-ray emission and with the same analysis condition on the deposited energy: 0.250 MeV $< E_{dep} <$ 5.53 MeV. The ratio between the counts detected with the U sample over the counts detected with the Pb sample gives the scale factor to apply to the lead yield to find the in-beam γ-ray background.

Once studied and evaluated all the background components we summed over all the contributions in order to find the total background for the measurement. In Figure 5.16 the ^{238}U capture yield is shown together with the background dismantled in its different components for the two detectors (Bicron: upper left panel, FK: upper right panel). In the bottom panel of the figure the background-free yields of the two detectors are compared, and results to be in good agreement from few eV up to 1 MeV. At lower energies the background in FZK detector results to be quite higher with respect to Bicron one. As previously outlined, the R-matrix code SAMMY can take into account the effects of residual background, and therefore the two yields can be safely added.

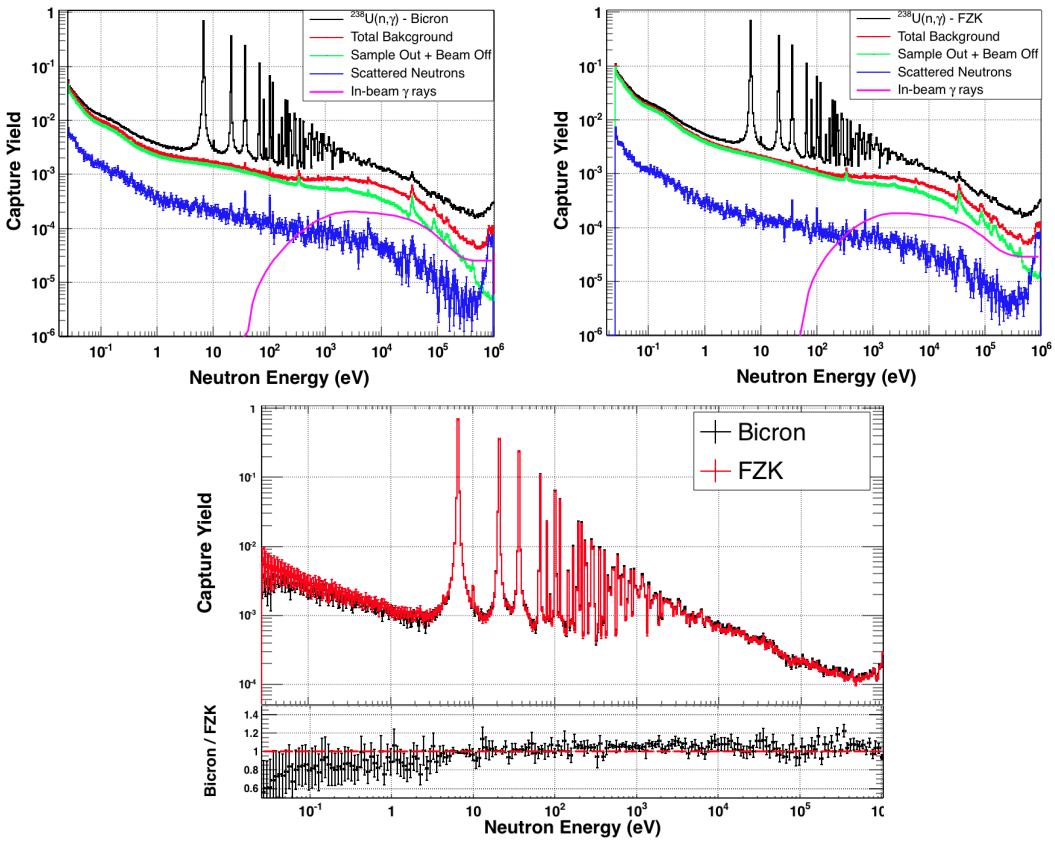

Fig. 5.16: Capture yield is shown in black for Bicron (upper left panel) and FZK (upper right panel) detectors, compared with the total background (red line) obtained via the filter-scaling procedure. In the bottom panel the comparison between the two background-free yields is shown. The agreement is very good from 100 eV up to 1 Mev, while at low energies one can clearly distinguish in the ratio some inconsistencies corresponding to the valley of the resonances, probably due to a residual background present in FZK detector.

5.4.3 Residuals background

Besides the background components listed at the beginning of this section, which we estimated through two independent methods, there could be some residual backgrounds. They are usually completely negligible, with an influence which remains within the uncertainties related to normalization or background subtraction. However, for this work, the ^{238}U(n,γ) cross section should be determined as precise as possible and therefore all the possible sources of background should be investigated.

First of all, we studied the inelastic scattering channels. As can be seen from the left panel of Figure 5.17, its cross section begins to be significative for $E_n \gtrsim 70$ keV. The

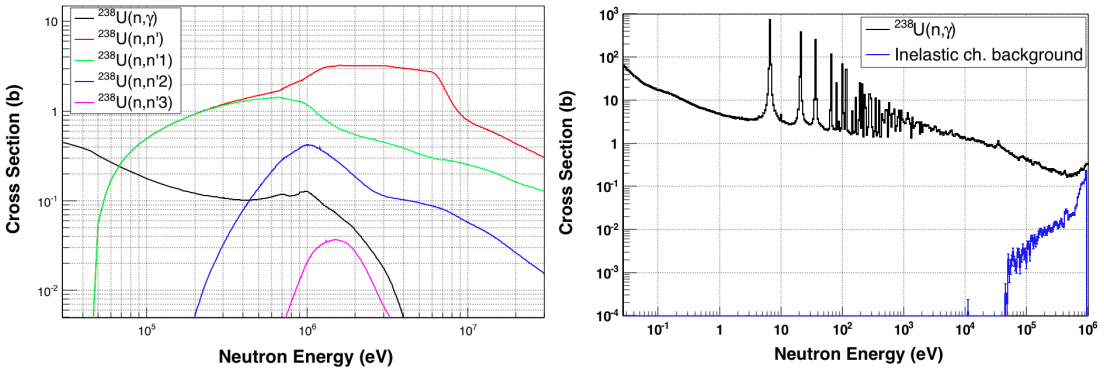

Fig. 5.17: Left panel: Neutron inelastic cross sections compared to the capture one (data from JEFF-3.2 library). Inelastic scattering cross-section becomes significative for $E_n \gtrsim 70$ keV. Right panel: Inelastic scattering contribution to the background as evaluated from GEANT4 simulations. This contribution becomes significative for incident neutron energies above 200 keV.

contribution to the background related to inelastic scattering has been evaluated through GEANT4 simulations. In principle, this background contribution is suppressed by the detector threshold $E_{\text{dep}} > 250$ keV, which corresponds to γ-ray energy of about 400 keV (and is therefore negligible for neutron energies below 400 keV). However a Monte Carlo simulation is required since the energy of the gamma ray produced in the inelastic scattering has to be convoluted with the energy-resolution of the detector. The results are shown in the right panel of Figure 5.17, where this contribution is compared to the total capture yield. It results that the effect of the energy resolution of the detector makes this background non-negligible for neutron energies greater than 200 keV. This background contribution was added to both filer-scaled and measured backgrounds.

At high energy, another problem arises related to the opening of the fission channel combined to the Pulse Height Weighting Technique. In fact, at incident neutron energies $E_n \gtrsim 100$ keV the fission channel starts to be open, but its cross section is $2 \div 3$ order of magnitudes lower than the capture one. However, applying the weighting functions to the counts the contribution of events with high energetic γ rays ($E_{\text{dep}} \sim$ few MeV) is enhanced, which is the case for fission events. Moreover, the multiplicity for fission events is higher, and consequential also the scintillator efficiency to detect a γ ray. These two effects could contribute to make the fission channel significative also in the hundreds of keV energy region. To verify this assumption, we studied the ratio between the unweighted counts C and the weighted one C_w, which is shown in the right panel of Figure 5.18. From the ratio a clear drop is visible at $E_n \sim 480$ keV, which means an artificial increase of the measured counts due to the weighting functions. For this reason, we decided to consider

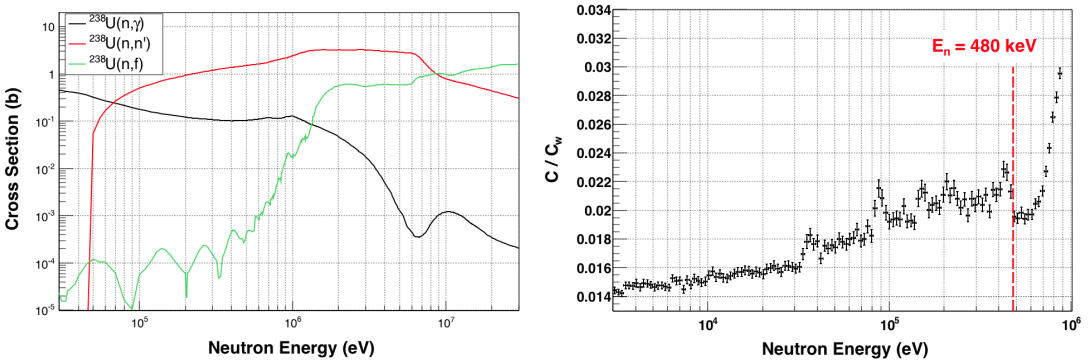

Fig. 5.18: Left panel: Neutron fission cross sections compared to the capture one (data from ENDF/B-VII.1 library). The opening of fission channel is at $E_n \gtrsim 100$ keV. Right panel: Ratio between unweighted C and weighted C_w counts from ^{238}U(n,γ). A drop is clearly visible at 480 keV, which means that the weighting function artificially increases the measured counts, probably because of the presence of high-energy, high-multiplicity γ-rays from fission.

the ^{238}U(n,γ) yield up to 480 keV. This choice also excludes background effects related to the influence of the γ-flash.

5.4.4 Comparison between the two methods

To associate an uncertainty to the level of the background, we compared the results obtained subtracting the background with the two different methods described above. In Figure 5.19 the two different normalized, background-free yields are plotted together with the ratio between the two (bottom panel in the figure).

This ratio reveals that for $E_n < 1$ eV a systematic deviation of about 10% is present between the two yields, $Y_{\text{meas}}/Y_{\text{filters}} \sim 10\%$.

In the Resolved Resonance Region, from $E_n = 1$ eV to 3 keV, the two yields agree within 4% apart from some point in the resonance valleys. In particular, the yield obtained subtracting the measured background shows a lower residual component in some resonance valleys.

In the Unresolved Resonance Region, from $E_n = 3$ keV to 100 keV the agreement is within the 4% as for the RRR, apart from energies corresponding to the two Al resonances at 35 keV and 86 keV, in which the yield obtained with the filter-scaled background presents two dips. The presence of Al absorption is due to in-beam materials (such as vacuum windows), and should give the same contribution both to capture and background counts. The dips in the background-subtracted yield indicates that this method is overestimating the background contribution at high energy. This is consistent to the

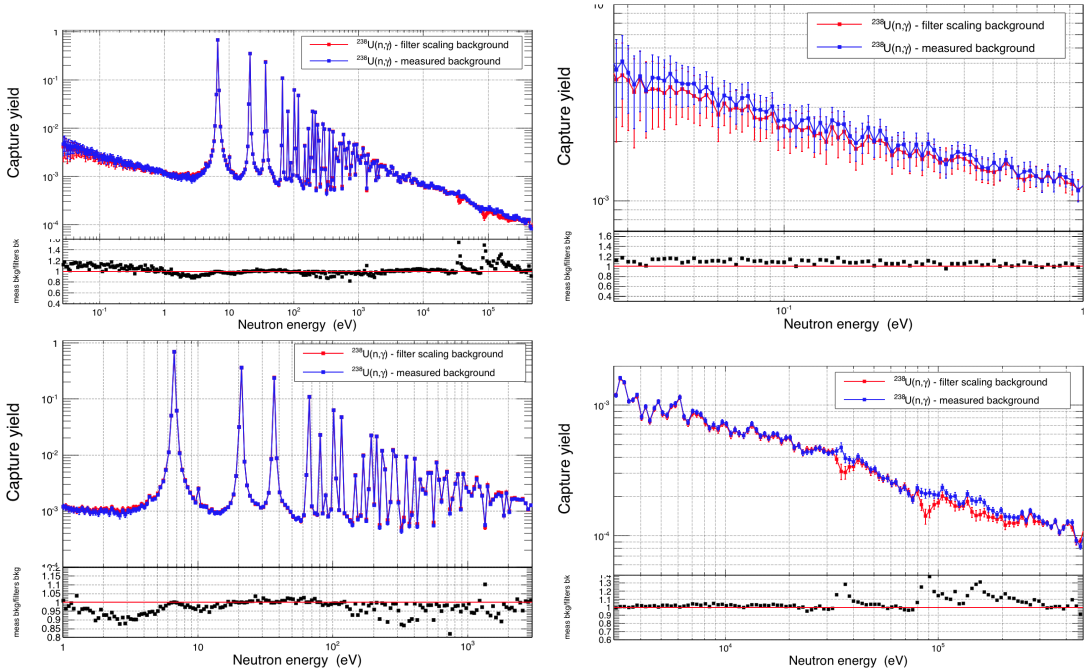

Fig. 5.19: ^{238}U(n,γ) normalized capture yield, obtained subtracting the filter-scaled background (red) and the measured background (blue) following the procedures described above. Thermal, Resolved and Unresolved Resonance region are zoomed out to better visualize the differences between the two yields. The percentage deviation between the two backgrounds is an estimation of the uncertainty in the level of background, and is reported in Table 5.4.

subsequent deviation of about 20% between the two yields for 100 keV$< E_n <$ 300 keV. For higher energies both the filter-scaled and the measured background become negligible with respect to the one related to inelastic scattering, and therefore the yields agree once more.

Since the background obtained with the filter-scaled method is affected by lager uncertainties (e.g. presence of Al in the beam and very low counting rate in the absorption dips) we decided to use the yield obtained subtracting the measured background.

From the comparison of the two yields, however, we are able to associate an uncertainty in the level of background, listed in Table 5.4. How these uncertainties propagate in the experimental yield depends on the signal to background ratio. This aspect is discussed in the next chapter (Section 6.2).

Table 5.4: Uncertainty on the level of ^{238}U(n,γ) background.

Region	Incident neutron Energy (eV)	Uncertainty (%)
Thermal	$0.027 < E_n < 1$	$8 - 10\%$
RRR	$1 < E_n < 3 \times 10^3$	5% - Resonance valleys < 2% - Resonance peaks
URR	$3 \times 10^3 < E_n < 100 \times 10^3$	4%
	$100 \times 10^3 < E_n < 480 \times 10^3$	10%

5.5 Capture Yield normalization

To find the normalization factor in Eq. 4.2 we applied to the counts first the weighting functions obtained with an exponential attenuation within the sample, and then the time-to-energy calibration. Moreover, a correction for the dead-time of the detectors is needed to correct for the rate dependence of counting losses in neutron time-of-flight measurements, as described in Ref. [166]. Afterwards, we divided te counts by the neutron flux obtaining an un-normalized capture yield to which the saturated resonance method is applied, as will be described hereafter.

The ^{238}U sample has been chosen in such a way that in the first three resonances all the neutrons arriving at the sample undergo at least one interaction, thus being saturated at their peaks. At this point the experimental capture yield $Y_c(E_n)$ becomes constant and close to one, and the normalization factor N is determined by comparing the measured yield with the expected one at the saturated region of the first three resonances. As demonstrated in Ref. [167], a normalization obtained from a saturated resonance for which $\Gamma_n \ll \Gamma_\gamma$ is nearly independent of the resonance parameters and target thickness.

The expected capture yields have been calculated separately for the two detectors with the resonance shape analysis code SAMMY [110]. A fit of the normalization factor has been performed starting from the resonance parameters present in ENDF/B-VII.1 library and letting only the resonance energy and the normalization value as free parameters. The result for the first resonance at 6.67 eV is shown in Figure 5.20 for FZK detector. To better understand the quality of the fit, for each bin we also calculated the Residuals:

$$\text{Residuals} = \frac{\text{data} - \text{fit}}{\Delta_{\text{statistical}}}, \tag{5.10}$$

where $\Delta_{\text{statistical}}$ is the uncertainty due to counting statistic. The distribution of the residual is expected to be a normal distribution centered in 0, the width of which is a

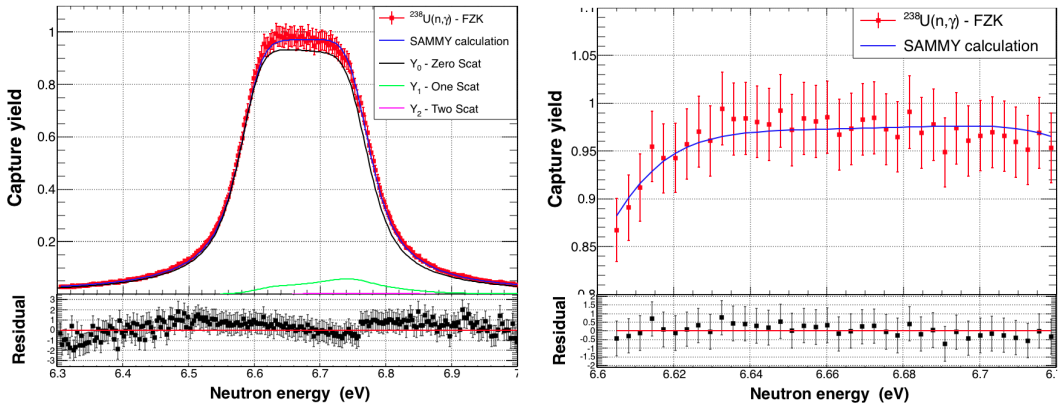

Fig. 5.20: Left panel: First saturated resonance at 6.67 eV measured with FZK scintillator (red point) and fitted with SAMMY (blue line). At the bottom also the residuals are plotted to show the quality of the fit. Right panel: Only the saturated plateau has been fitted to better identify the normalization factor. The yield has been extracted with 5000 bins/decade.

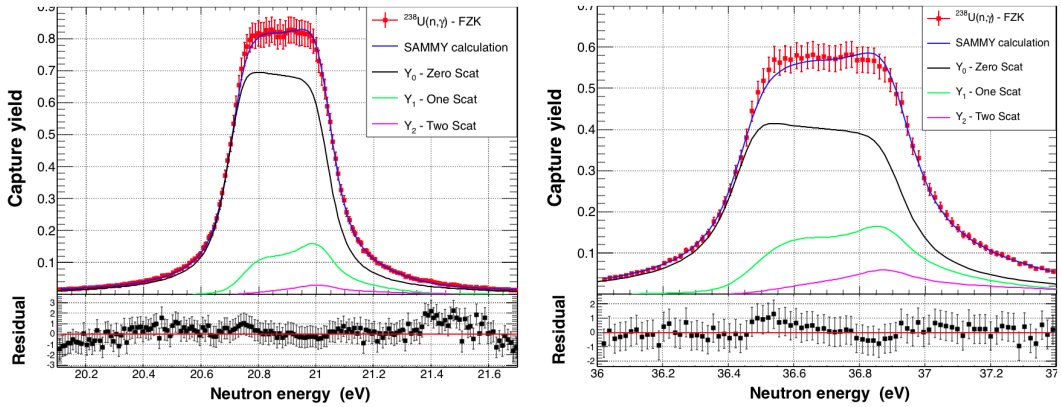

Fig. 5.21: Second saturated resonance at 20.9 eV (right panel) and third saturated resonance at 36.7 eV measured with FZK scintillator (red point) and fitted with SAMMY (blue line). At the bottom also the residuals are plotted to show the quality of the fit. The yield has been extracted with 5000 bins/decade.

representation of how much the difference between the data and its fit deviates from the statistical uncertainty.

To extract the normalization factor without being influenced by the resonance tails, the fit has been performed only in the saturated plateau of the resonance, as shown in the right panel of Figure 5.20.

The second (20.9 eV) and third (36.7 eV) resonances have a higher scattering cross section ($\Gamma_n/\Gamma_\gamma = 0.06$, 0.44 and 1.46 for the 6.7, 20.9 and 36.7 eV resonances respectively), as can be seen from the contributions due to the various neutron scattering inside the sample shown in Figure 5.21 (for comparison, also in Figure 5.20 these contributions are shown, which result to be almost completely negligible). However, the correction for the

multiple scattering implemented in SAMMY allowed us to fit these resonances as well. In Table 5.5 the results of the fit of the three resonances are listed for both detectors. The final normalization factors have been chosen as the average of the three values, which have a 1% deviation between themselves chosen as the normalization uncertainty: $N_{\mathrm{bic}} = 0.844 \pm 0.008$ and $N_{\mathrm{fzk}} = 0.991 \pm 0.009$.

Table 5.5: Normalization factor for the ^{238}U(n,γ) yield for Bicron and FZK scintillators.

Detector	Normalization factor			Percentage deviation		
	N_1	N_2	N_3	N_1/N_2	N_2/N_3	N_1/N_3
Bicron	0.838	0.837	0.856	0.06%	2%	2%
		$N_{\mathrm{bic}} = 0.844$			$\Delta N_{\mathrm{bic}}/N_{\mathrm{bic}} = 1\%$	
FZK	0.999	0.982	0.992	2%	0.9%	0.7%
		$N_{\mathrm{fzk}} = 0.991$			$\Delta N_{\mathrm{fzk}}/N_{\mathrm{fzk}} = 1\%$	

The normalization is a fundamental point for an accurate and precise extraction of the experimental yield. Exploiting a saturated resonance means to experimentally determine the geometrical beam-sample interception area eliminating any errors due to sample alignment. Moreover, this method allowed us also to correct for the absolute value of the incident neutron flux that, as showed in Section 5.3.2, could change year by year.

In addition, since we used the saturated resonances from ^{238}U(n,γ), the yield is self-normalized and the uncertainties are drasticcally reduced. For instance, we eliminated inconsistencies due to internal-conversion processes and problems related to the alignment of the samples that can arise if a reference sample, such as ^{197}Au, is used.

5.6 Summary

In this Chapter we described all the details of the data reduction procedure and yield extraction for the ^{238}U(n,γ) measurement. Starting from the description of the experimental campaign, we showed how the stability of the detection system has been checked.

After the proper determination of the weighting functions, needed to apply the total energy technique, we proceeded to the extraction of the capture yield.

We justified the use of the 2011 evaluated flux, showing the good agreement with the 2012 flux from Silicon Monitor.

Particular attention has been paid to the subtraction of the background. Two different methods have been followed, and from the comparison between the two we associated an uncertainty to the background level of 2% to 10% depending on the energy region.

We described the normalization procedure exploiting the saturated resonance method together with the associated uncertainty.

These steps are the basic requirements for the final goal of the measurement: to provide the ^{238}U(n,γ) reaction cross-section as precise as possible, so to reach, once combined with the other measurements, the 2% uncertainty.

Chapter 6
^{238}U(n,γ) measurement with C_6D_6: results

The capture yield obtained as described in the previous chapter is used to extract the ^{238}U(n,γ) reaction cross section. In particular, in the Resolved Resonance Region (RRR) (1 eV $< E_n <$ 3 keV) we analyzed the experimental yield with the resonance shape analysis (RSA) code SAMMY to obtain the parametrization of the capture cross-section in term of resonance parameters. Since RSA codes need starting values for the resonance parameters the JEFF-3.2 neutron data library was used. In the Unresolved Resonance Region (URR) the cross section is obtained from the experimental yield by applying a correction factor to take into account the sample-related effects of self-shielding and multiple scattering. The resulting cross section and the cross-section parameters are compared to the values present in literature.

6.1 The SAMMY code

The multilevel multichannel R-matrix code SAMMY [110] was developed by Dr. Nancy Larson and released for use in analysis of neutron-induced cross section data at the Oak Ridge Electron Linear Accelerator in 1980. It is now widely used to analyze a great variety of data, thanks to the corrections for several experimental conditions available in the code, such as Doppler and resolution broadening, multiple-scattering corrections for capture or reaction yields, normalizations and backgrounds. This work exploits the SAMMY code with the purpose to evaluate the resonance parameters of ^{238}U(n,γ) cross section in the Resolved Resonance Region.

The theoretical reaction yield is obtained through the Reich-Moore approximation of the multi-level R-matrix formalism (see Section 2.2.1.3), and convoluted with the experimental resolution. The resonance parameters together with other parameters related to the experimental set up (like, for example, normalization, background level, effective

temperature, target thickness) can be determined by a least-square fit to the experimental data. The fitting procedure is the Bayes' method (generalized least-square), and consist in the minimisation of the χ^2 defined as:

$$\chi^2(\mathbf{a},\mathbf{b}) = (\mathbf{D} - \mathbf{T}(\mathbf{a},\mathbf{b}))^T \, V_{Z_D}^{-1} \, (\mathbf{D} - \mathbf{T}(\mathbf{a},\mathbf{b})) \, . \tag{6.1}$$

Here, **a** is the vector of resonances and **b** the vector of experimental parameters. The experimental data are represented by a data vector **D**, while **T** represents the corresponding theoretical values (i.e., calculated values of cross section or transmission plus corrections). The covariance matrix V_{Z_D} represents not only the experimental errors of the data but also any theoretical errors resulting from approximations used in calculating **T**. Within the code the full covariance matrix is properly treated.

6.2 Discussion on the uncertainties

The total uncertainty in the ^{238}U(n,γ) cross section is a combination of several components related to the sample characteristics and the analysis procedure. Alongside the uncorrelated uncertainty due to the counting statistics, correlated uncertainties are involved.

The uncertainty related to sample characterization is almost negligible since the sample mass has been determined at the EC-JRC-IRMM with an accuracy of about 1‰.

An important source of correlated uncertainty is the yield normalization. Applying an internal normalization derived from the first three saturated resonances (E_n = 6.673 eV, E_n = 20.871 eV and E_n = 36.681 eV) the uncertainty in the normalization factor is reduced to less than 1%. This correlated uncertainty component has to be combined with an uncertainty ranging from 1% to 5% due to the neutron flux shape.

The background subtraction plays a fundamental role in determining the uncertainties at all energies, this is why its determination required a detailed study. In Table 5.4 the relative uncertainties on the background level are listed. These uncertainties propagate to the final capture yield depending on the signal to background ratio S/B:

$$\text{Background-subtraction uncertainty} = \left(\frac{\Delta B}{B}\right) \frac{1}{S/B} \tag{6.2}$$

where B represents background counts. Therefore, for energies within the RRR the error due to background subtraction is almost completely negligible, being the signal to background ratio more than a factor of 10. In the URR the signal to background ratio is

about a factor of 2, and therefor for 3 keV $< E_n <$ 100 keV the error due to background subtraction is $\sim$ 2%, while for 100 keV $< E_n <$ 480 keV is $\sim$ 5%.

In Table 6.1 all the correlated uncertainties are listed for the different energy ranges.

Table 6.1: Summary of the correlated uncertainties in the ^{238}U(n,γ) cross section measurement.

Source of uncertainty	Uncertainty RRR	Uncertainty URR	Reference
Sample mass	0.03%	0.03%	Section 5.1.1
Neutron flux - shape	1-2%	3<E_n<100 keV: 4-5% 100<E_n<480 keV: 2%	Section 3.4.1
Normalization	1%	1%	Section 5.5
Background subtraction	1-2%	3<E_n<100 keV: 2% 100<E_n<480 keV: 5%	Section 5.4.4
Total	2-3%	3<E_n<100 keV: 4.5-5.5% 100<E_n<480 keV: 5.5%	

6.3 Analysis of the RRR

As previously pointed out, in the Resolved Resonance Region the level distance D is large compared to the natural width Γ and the instrumental resolution. As shown in Figure 3.7 this condition is satisfied at the n_TOF spectrometer up to E_n = 20 keV. However, the signal to background ratio decreases as the energy increases, and the statistics determines the upper energy limit of the RRR. Within this measurement, we can accurately resolve resonances up to E_n = 2.2 keV, and the highest resonance we can analyze is at 2.95 keV.

Within this energy region, a resonance shape analysis has been performed, by means of the R-matrix code SAMMY, on the yield obtained at n_TOF. The resolution function of the n_TOF spectrometer is implemented in SAMMY via a numerical description derived from Monte Carlos simulations (see Section 3.3.2.2).

Although we analized the background-subtracted capture yield, some residual background can be present. As previously outlined, the SAMMY code gives an independent value to the background level through the fitting procedure. We found two different residual-background components, one constant and one exponential, which are shown in the left panel of Figure 6.1 and follow the equation:

$$B(E) = a\mathrm{e}^{bE} + c, \tag{6.3}$$

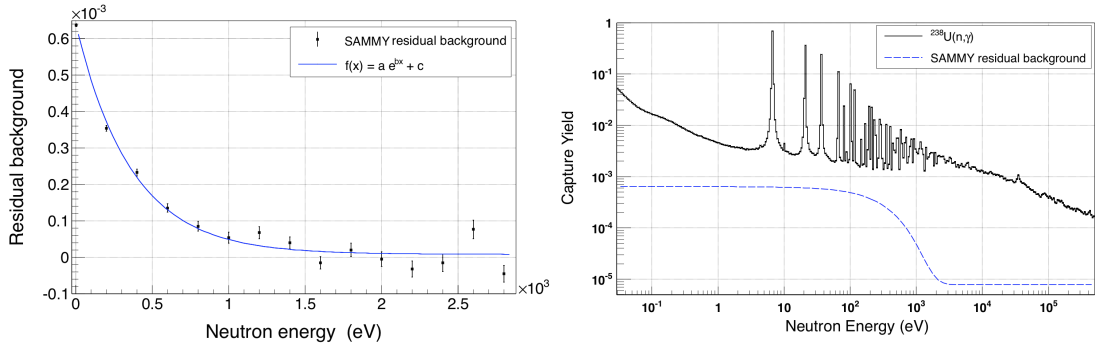

Fig. 6.1: Residual background present in the capture yield. Left panel: black points are the values given by the SAMMY best fit for the background level parameter in different energy intervals, and follow Eq. 6.3 given as a blue line. Right panel: the obtained residual background is plotted in comparison with the capture yield.

where $a = 6.29 \times 10^{-4}$ eV, $b = -2.7$ eV^{-1} and $c = 7.8 \times 10^{-6}$ eV. From the figure is clear that from $E_n = 1.5$ keV the residual-background is represented by only the constant component, while at lower neutron energies some additional background needs to be included. The identified residual background barely influenced the capture yield, as can be seen in the right panel of Figure 6.1.

Once subtracted this additional background to the capture yield, we proceed to extract from it the resonance parameters as explained in Section 6.1. Starting from initial values taken from JEFF-3.2 library, our fitting strategy is to leave as free parameter only the smallest between radiative Γ_γ and elastic Γ_n partial widths, while the other one was kept fixed. In few cases, in order to improve the description of the resonance shape analysis we left both the partial widths free.

In Figure 6.2 and 6.3 the measured capture yield together with the SAMMY best-fit curve are shown. The residuals are plotted in the bottom panel to underline the quality of the fit.

From the resonance parameters obtained through the SAMMY fit procedure we calculated the resonance kernels κ, defined in Eq. 2.72. The values are listed in Table 6.2 and we used this quantity to compare our data to ENDF/B-VII.1 and JEFF-3.2 libraries and to the results obtained with the Total Absorption Calorimeter (also referred to as TAC). This measurement has been performed at n_TOF in 2011 with the same ^{238}U sample of the present work. The preliminary results have been presented by T. Wright *et al.* [63], and the resonance shape analysis has been carried out leaving both the partial widths as free parameters in the fitting procedure. To the TAC data an uncertainty $\gtrsim 2\%$ has been associated.

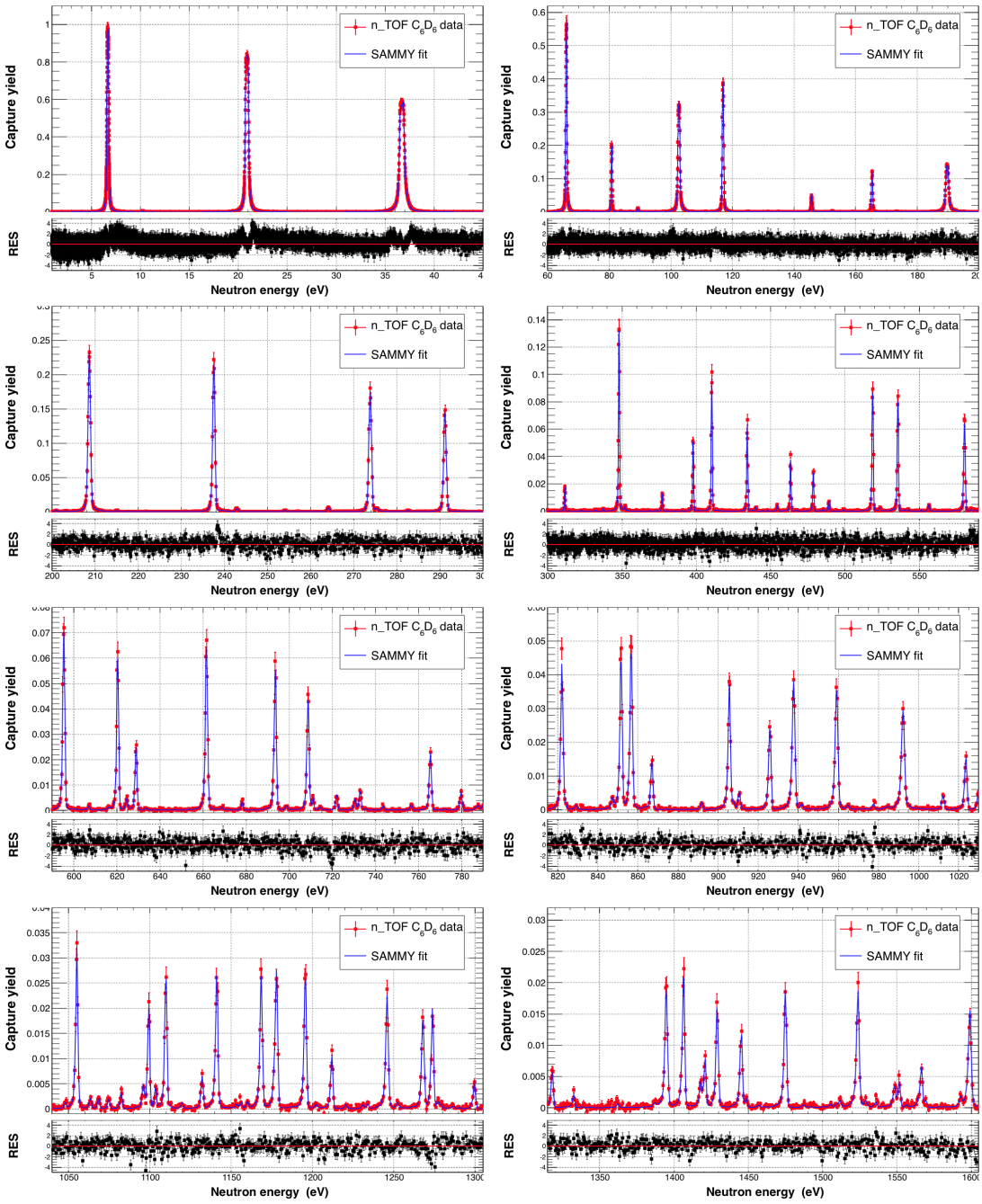

Fig. 6.2: Experimental capture yield for ^{238}U(n,γ) reaction obtained with C_6D_6. The SAMMY best-fit curve is plotted as well. The bottom panels shows the residuals to underline the quality of the fit.

Fig. 6.3: *Continued from previous page.*

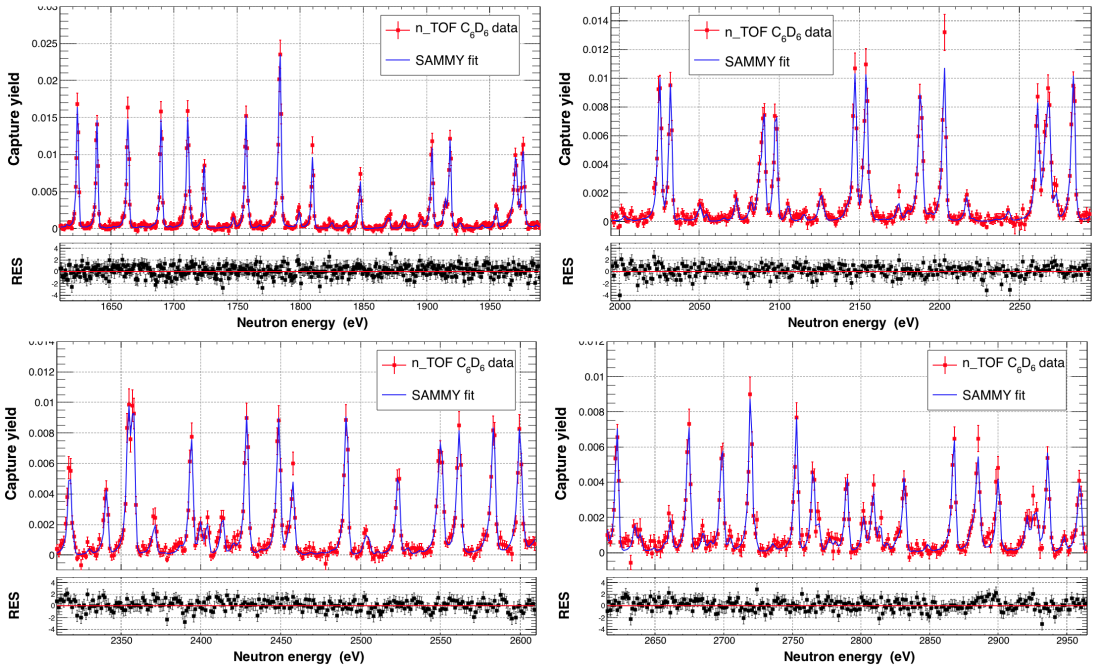

Kernels obtained leaving both Γ_n and Γ_γ partial widths as free parameters during the fitting procedure in our work are marked with an asterisk in Table 6.2. The first three resonances are not included because, being saturated, the resonance shape analysis cannot give accurate parameters.

From the table it is visible that some kernels, most of which obtained from a 2-parameters fit, have large relative errors. This is due to a lack of statistics for resonances with small counting rates, and more reliable results will be obtained combining this data-set to the one obtained with the TAC.

Table 6.2: Resonance kernels (κ) for ^{238}U+n calculated from parameters obtained from SAMMY fit of n_TOF C_6D_6 data, and from ENDF/B-VII.1 and JEFF-3.2 libraries and from TAC data.

	C_6D_6		TAC	ENDF/B-VII.1	JEFF-3.2
E_R	κ	$\Delta\kappa/\kappa$	κ	κ	κ
(eV)	(meV)	%	(meV)	(meV)	(meV)
66.03	12.0 ± 0.08	0.6	12.08	11.87	11.89
80.75	1.77 ± 0.02	1	1.73	1.73	1.74
102.56	17.9 ± 0.1	0.7	17.67	17.97	17.61
116.89	11.6 ± 0.1	0.9	11.79	11.86	12.05

Table 6.2: Resonance kernels (κ) for ^{238}U+n calculated from parameters obtained from SAMMY fit of n_TOF C_6D_6 data, and from ENDF/B-VII.1 and JEFF-3.2 libraries and from TAC data.

	C_6D_6		TAC	ENDF/B-VII.1	JEFF-3.2
E_R (eV)	κ (meV)	$\Delta\kappa/\kappa$ %	κ (meV)	κ (meV)	κ (meV)
145.66	0.93 ± 0.02	2	0.88	0.85	0.85
165.32	3.03 ± 0.05	2	2.94	2.82	2.82
189.68	19.2 ± 0.2	1	19.00	20.71	20.70
208.53	15.3 ± 0.2	1	15.37	15.66	15.70
237.40	12.0 ± 0.2	2	13.19	12.90	12.95
273.68	11.7 ± 0.2	2	12.09	12.32	11.94
291.02	9.8 ± 0.2	2	9.83	9.66	9.55
311.35	1.14 ± 0.04	3	1.03	1.01	1.00
347.83	17.0 ± 0.3	2	16.32	17.11	17.25
376.97	1.11 ± 0.05	4	1.07	1.06	1.07
397.64	5.0 ± 0.1	3	4.88	4.62	4.62
410.27	11.0 ± 0.3	2	10.88	10.44	10.54
434.12	7.3 ± 0.2	3	7.05	6.91	6.87
463.25	4.7 ± 0.1	3	4.55	4.43	4.42
478.49	3.7 ± 0.1	3	3.41	3.40	3.40
488.89	1.0 ± 0.4	44	0.90	0.83	0.83
518.44	15.6 ± 0.4	2	15.82	15.28	15.39
535.38	15.0 ± 0.4	3	14.93	15.60	15.72
580.20	13.3 ± 0.4	3	14.95	14.39	14.49
595.14	17.4 ± 0.4	2	17.30	18.20	18.20
620.07	12.9 ± 0.4	3	12.37	13.04	13.15
628.63	5.0 ± 0.2	3	4.95	5.12	5.20
661.29	20.0 ± 0.6	3	19.77	20.29	20.45
693.17	14.6 ± 0.4	3	14.32	14.83	14.92
708.38	11.3 ± 0.4	4	10.80	11.30	11.36
721.68	1.45 ± 0.09	6	1.25	1.12	1.36
730.20	1.0 ± 0.9*	88	1.01	1.00	0.98
765.18	6.3 ± 0.3	4	5.96	6.43	6.43
790.89	5.0 ± 0.2	5	5.06	5.21	5.19
821.69	15.6 ± 0.5	3	15.82	16.64	16.80
851.14	17.1 ± 0.7	4	16.36	17.38	17.21
856.22	19.0 ± 0.6	3	17.58	18.53	18.47
866.59	5.0 ± 0.2	4	4.61	4.74	4.74

Table 6.2: Resonance kernels (κ) for ^{238}U+n calculated from parameters obtained from SAMMY fit of n_TOF C_6D_6 data, and from ENDF/B-VII.1 and JEFF-3.2 libraries and from TAC data.

	C_6D_6		TAC	ENDF/B-VII.1	JEFF-3.2
E_R (eV)	κ (meV)	$\Delta\kappa/\kappa$ %	κ (meV)	κ (meV)	κ (meV)
905.17	15.7 ± 0.6	4	15.25	16.65	16.19
925.20	9.6 ± 0.4	5	9.55	9.36	9.68
937.17	19.4 ± 0.7	4	18.82	20.56	20.58
958.67	21.3 ± 0.8	4	18.96	20.91	20.65
991.76	22.6 ± 1	4	21.25	22.82	22.81
1023.11	7.2 ± 0.4	6	6.50	6.56	6.56
1054.64	18.2 ± 0.8	4	17.55	18.54	18.54
1098.86	9.4 ± 0.5	5	9.76	11.14	11.14
1109.27	14.3 ± 0.7	5	14.21	14.14	14.14
1140.53	18.9 ± 0.9	5	19.16	20.97	20.97
1167.83	18 ± 1	6	17.31	18.33	18.33
1177.40	16.9 ± 0.8	5	16.85	17.08	17.08
1195.03	17.9 ± 0.8	5	17.39	18.56	18.56
1211.32	6.5 ± 4	61	6.63	4.01	6.54
1245.27	20 ± 1	5	18.86	21.13	21.13
1267.26	12.2 ± 0.7	5	13.04	12.95	12.95
1273.20	13.6 ± 0.7	6	11.42	12.28	12.28
1298.82	3.5 ± 3	76	3.33	3.36	3.36
1394.04	19.3 ± 1	6	20.64	20.77	20.77
1405.67	17.6 ± 1	6	17.62	17.58	17.58
1420.01	6.1 ± 0.5	8	6.80	6.86	6.86
1428.25	13.7 ± 0.8	6	12.15	12.95	12.95
1444.33	9.8 ± 0.7	7	9.59	9.86	9.86
1474.08	18.0 ± 1	5	18.03	19.41	19.41
1522.95	21.0 ± 1	6	19.93	21.05	21.05
1565.54	6.1 ± 0.7	12	4.72	4.71	4.71
1591.69	1.3 ± 1	92	1.29	1.29	1.29
1598.16	21.2 ± 1	5	20.79	21.70	21.70
1622.95	18.1 ± 1	5	17.13	18.83	18.83
1638.34	15.4 ± 1	6	15.39	15.82	15.82
1662.70	18.8 ± 1	6	19.66	20.91	20.91
1689.05	17.6 ± 1	6	18.69	18.98	18.98
1710.06	17.6 ± 1	7	17.52	18.14	18.14

Table 6.2: Resonance kernels (κ) for ^{238}U+n calculated from parameters obtained from SAMMY fit of n_TOF C_6D_6 data, and from ENDF/B-VII.1 and JEFF-3.2 libraries and from TAC data.

	C_6D_6		TAC	ENDF/B-VII.1	JEFF-3.2
E_R (eV)	κ (meV)	$\Delta\kappa/\kappa$ %	κ (meV)	κ (meV)	κ (meV)
1723.05	9.9 ± 0.7	7	10.52	10.45	10.45
1756.14	19.2 ± 1	6	18.22	19.65	19.65
1782.61	23.9 ± 18	76	20.10	20.94	20.94
1783.17	20 ± 16	80	20.91	21.82	21.82
1808.67	12.0 ± 0.8	7	11.06	10.86	10.86
1846.35	$9 \pm 6^*$	71	8.08	7.95	7.95
1903.08	15.1 ± 1	8	15.77	15.47	15.47
1917.44	16.8 ± 1	7	15.76	15.14	15.14
1954.05	3.6 ± 3	85	3.74	3.73	3.73
1969.29	20.6 ± 2	9	21.10	22.36	22.36
1975.18	20.6 ± 2	9	21.48	21.94	21.94
2023.99	17.4 ± 1	7	19.21	20.92	20.92
2030.79	15.0 ± 1	8	15.72	15.84	15.84
2088.87	12.7 ± 1	9	13.14	12.69	12.69
2096.60	12.9 ± 1	8	12.91	13.18	13.18
2145.86	17.7 ± 2	9	17.67	17.62	17.62
2153.07	21 ± 2	8	20.47	21.41	21.41
2186.90	23 ± 2	7	22.05	22.15	22.15
2201.65	$20 \pm 7^*$	36	20.89	21.59	21.59
2260.03	15 ± 2	10	17.63	18.82	18.82
2264.50	$6 \pm 2^*$	39	5.14	5.14	5.14
2266.89	$20 \pm 3^*$	16	19.38	20.95	20.95
2282.24	20 ± 2	8	19.54	20.64	20.64
2316.23	10 ± 6	56	10.27	10.24	10.24
2353.11	16 ± 2	11	15.93	16.01	16.01
2356.07	21 ± 2	9	19.08	18.31	18.31
2392.34	16 ± 1	9	13.58	13.48	13.48
2427.27	21.6 ± 2	7	19.14	20.18	20.18
2447.08	20.5 ± 2	8	20.93	20.92	20.92
2456.11	$11 \pm 8^*$	72	10.89	10.92	10.92
2489.54	22 ± 3	15	16.58	18.96	18.96
2521.73	$12 \pm 6^*$	49	12.63	11.55	11.55
2548.55	24 ± 2	9	22.36	22.30	22.30

Table 6.2: Resonance kernels (κ) for ^{238}U+n calculated from parameters obtained from SAMMY fit of n_TOF C_6D_6 data, and from ENDF/B-VII.1 and JEFF-3.2 libraries and from TAC data.

	C_6D_6		TAC	ENDF/B-VII.1	JEFF-3.2
E_R (eV)	κ (meV)	$\Delta\kappa/\kappa$ %	κ (meV)	κ (meV)	κ (meV)
2559.93	22 ± 2	9	21.07	21.35	21.35
2581.52	23.5 ± 2	9	19.47	21.93	21.93
2597.99	27 ± 3	10	19.61	22.36	22.36
2620.42	17 ± 6*	36	15.96	15.90	15.90
2672.58	21 ± 2	9	20.52	21.37	21.37
2696.90	16 ± 7*	44	14.04	14.30	14.30
2717.68	24 ± 2	8	19.80	20.39	20.39
2751.21	21 ± 9*	42	18.14	17.90	17.90
2763.01	12 ± 6*	48	11.23	10.92	10.92
2787.89	11 ± 7*	65	11.12	10.84	10.84
2806.88	9 ± 4*	44	8.29	8.05	8.05
2829.77	12 ± 8*	70	12.04	11.97	11.97
2865.84	20 ± 2	9	19.08	20.88	20.88
2883.21	20 ± 2	11	21.05	22.24	22.24
2934.11	17 ± 6*	36	15.24	15.25	15.25
2957.45	12 ± 6*	51	12.72	12.67	12.67

6.3.1 Comparison with ENDF/B-VII.1 and JEFF-3.2

As previously outlined, we used the resonance kernels to compare the present data with evaluated data libraries. For the comparison, we analyzed the ratio of C_6D_6 kernels over others, and we studied this ratio as a function of: (*i*) resonance energy E_R, (*ii*) the kernels themselves, and (*iii*) the ratio $g\Gamma_n/\Gamma_\gamma$, being g the statistical spin factor. Each comparison will be analyzed and explained in this section.

In Figure 6.4 C_6D_6 kernels over ENDF/B-VII.1 and JEFF-3.2 are shown as a function of resonance energy. This plot tests the accuracy of our measurement. Because of the large number of measurement carried out so far, and the effort spent in producing an accurate ^{238}U(n,γ) evaluation, as described in Section 1.7.1, the values of resonance kernel ratios are expected to be distributed around one. However, in some cases the two libraries

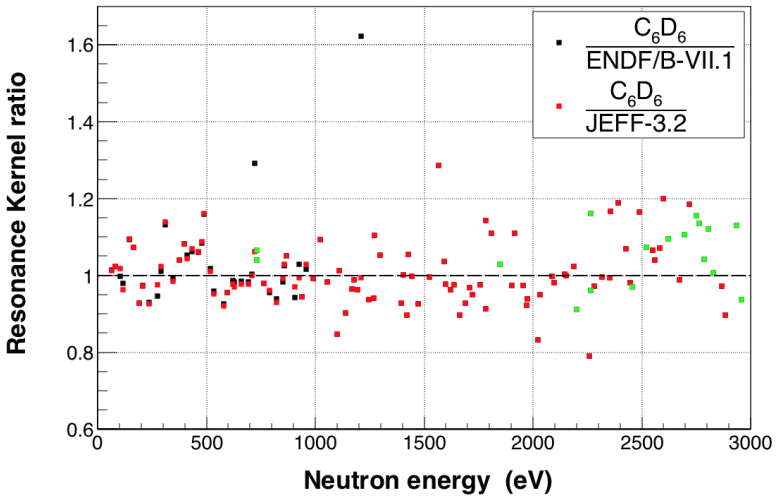

Fig. 6.4: Resonance kernels ratio as a function of resonance energy: C_6D_6 over ENDF/B-VII.1 as black points, C_6D_6 over JEFF-3.2 as red points. From E_n = 1.5 keV onward the two libraries report exactly the same sets of resonance parameters. Green points are kernels obtained with the two partial widths as free parameters of SAMMY fit.

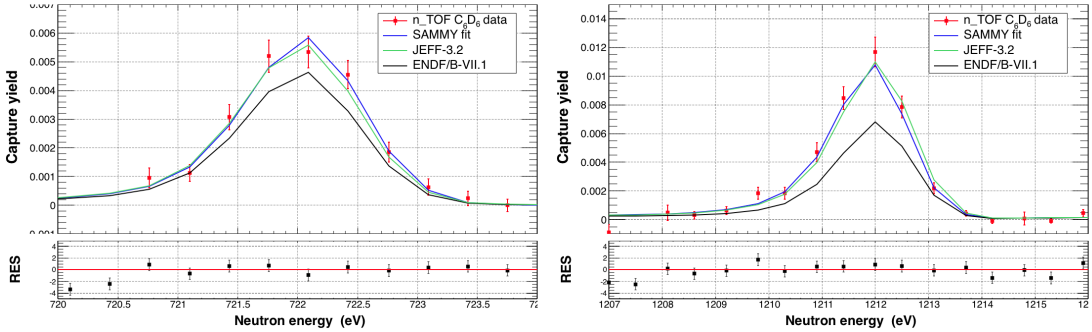

Fig. 6.5: Resonances at E_R = 721.68 eV and E_R = 1211.31 eV. Data from this work are red points, and the SAMMY best fit is shown as a blue line. Calculations performed using JEFF-3.2 and ENDF/B-VII.1 resonance parameters are shown as green and black lines respectively. It is visible that the ENDF/B-VII.1 library wrongly reported the parameters for both resonances, and in particular it underestimates the values of the capture kernels. See text for a detailed explanation.

present sizable differences for some resonances below 1.5 keV. In this energy region, there are two resonances, at 721.68 eV and 1211.31 eV, which strongly differs from those indicated by the ENDF/B-VII.1 library, while are in good agreement with JEFF-3.2. This indicates that the evaluated values of the capture partial width are underestimated in ENDF/B-VII.1 library, being Γ_γ = 3.15 meV and Γ_γ = 6.6 meV respectively.These two resonance have larger capture widths, as correctly reported in JEFF-3.2: Γ_γ = 23.0 meV and Γ_γ = 17.55 meV respectively (see Figure6.5).

To better understand the comparison between this work and evaluated resonance parameters, we studied the statistical distribution of resonance kernel ratios shown in Figure 6.6 (we neglected the two incorrect resonances of ENDF/B-VII.1). We found that, for 1 eV $< E_R <$ 1.5 keV, the ratios have a gaussian distribution centered in 1, with a standard deviation $\sigma = 0.06$, as shown in the right panel of Figure 6.6. The distribution for all energies (1 eV $< E_R <$ 3 keV) has a slightly larger mean value $\mu = 1.01$, meaning that we are overestimating the resonance kernels of about 1%, and a larger standard deviation $\sigma = 0.08$. Moreover, from the left panel of Figure 6.6, it is clear that the distribution is not perfectly gaussian, with a large right tale (in the direction of higher resonance kernels). As can be seen from the bottom panel of Figure 6.6, this behaviour is related to high energy resonances: from 2.2 keV to 3 keV, in fact, C_6D_6 resonance kernels are 7% above evaluated ones on average. In this energy region the data starts to suffer

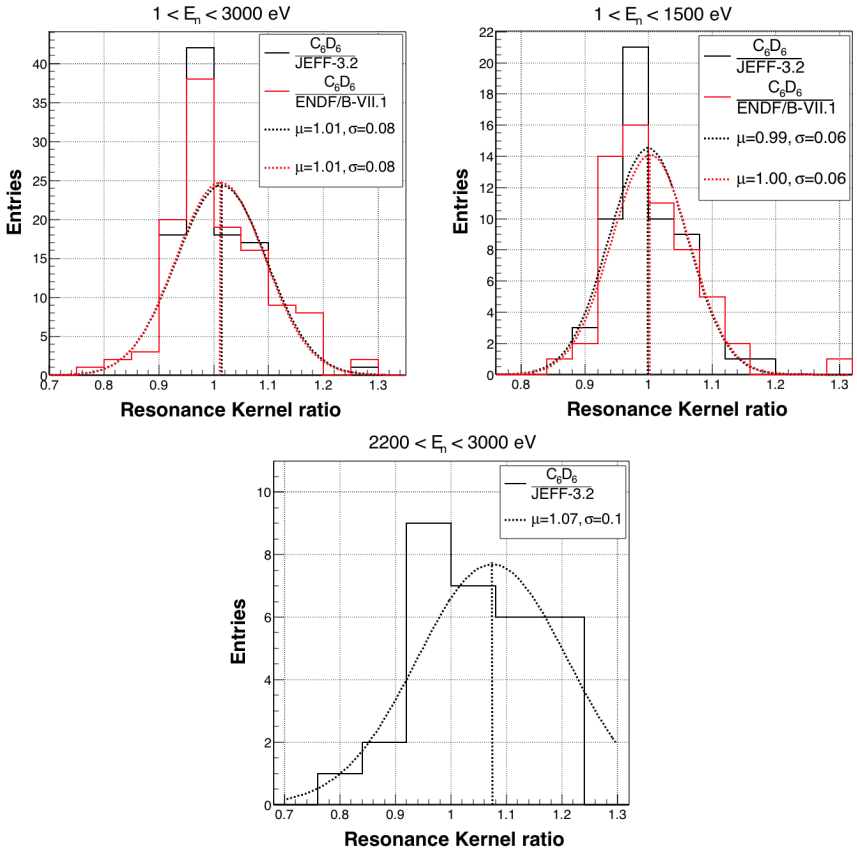

Fig. 6.6: Statistical distribution of resonance kernel ratios for different energy regions: black line indicates C_6D_6 over JEFF-3.2, red line C_6D_6 over ENDF/B-VII.1. The gaussian best-fit curve is also plotted with the same color code (for energies above 1.5 keV the two libraries adopt the same parameters, therefore only one curve is shown).

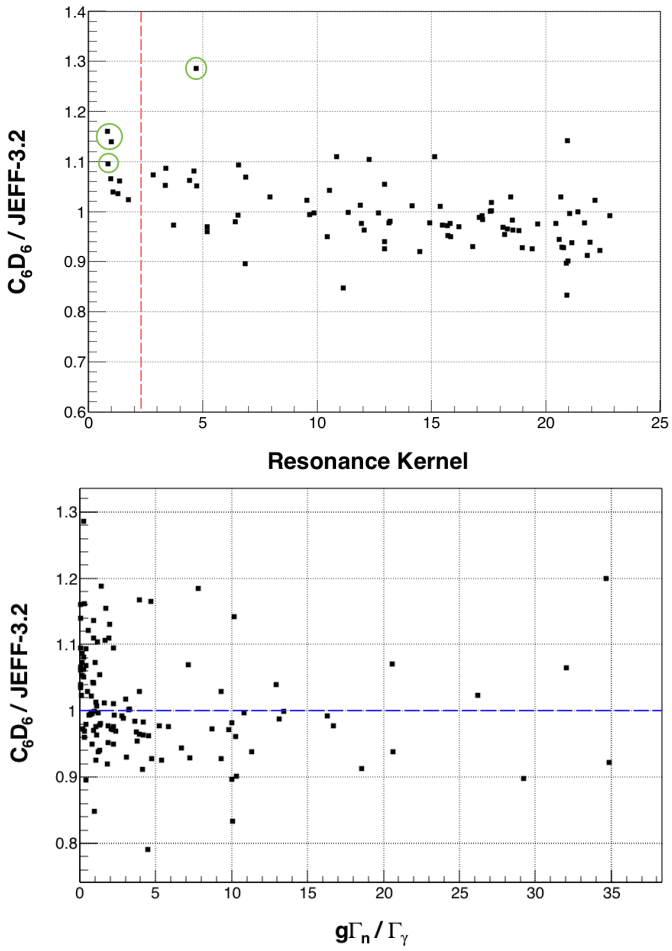

Fig. 6.7: Top panel: C_6D_6 resonance kernels over JEFF-3.2 as a function of JEFF-3.2 resonance kernels. For $\kappa <$ 2.3 meV C_6D_6 data stay systematically above evaluated parameters. Bottom panel: C_6D_6 resonance kernels over the ratio $g\Gamma_n/\Gamma_\gamma$ (partial widths from JEFF-3.2).

for lack of statistic, and therefore resonances observed in this work could be analyzed up to 2.2 keV.

Resonance kernel ratios, i.e. kernels obtained from this measurement over the ones calculated from data libraries, can be studied as a function of resonance kernel itself or of the ratio $g\Gamma_n/\Gamma_\gamma$, in order to find the presence of systematic effects related to resonance strength or to neutron scattering respectively. In Figure 6.7 the two plots are shown, the abscissa of which reports JEFF-3.2 evaluated values.

In the left panel the plot of kernel ratios versus JEFF-3.2 kernels is shown, from which it is visible that for small resonance (with kernels $\kappa < 2.3$ meV) measured resonance parameters are systematically above evaluated ones. Despite the low strength of these

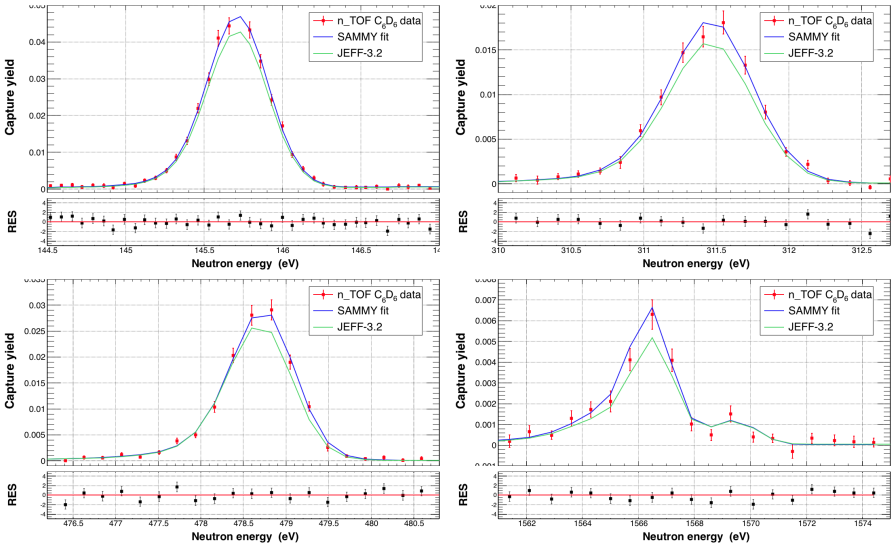

Fig. 6.8: Resonances at E_R = 145.66 eV (top left), E_R = 311.35 eV (top right), E_R = 488.89 eV (bottom left) and E_R = 1565.54 eV (bottom right). Data from this work are red points, and the SAMMY best fit is shown as a blue line. Calculation performed using JEFF-3.2 resonance parameters is shown as a green line for comparison. The bottom panel of each figure shows the residuals of the fit.

resonances, three of them are in the low energy region, E_R = 145.66, 311.35, 488.89 eV, where the statistics is very high. The fitting procedure is therefore quite accurate, and its results in Figure 6.8 shows that C_6D_6 data are actually higher than what predicted by JEFF-3.2. The same conclusion can be taken for the resonance at E_R = 1565.54 eV, a stronger resonance which, however, is $\sim$ 27% higher that what predicted from JEFF-3.2 parameters.

In the bottom panel of Figure 6.7 resonance kernel ratios are plotted as a function of $g\Gamma_n/\Gamma_\gamma$, where partial widths are taken from JEFF-3.2. A trend in this plot would be sign of systematic effects attributable to the neutron sensitivity of the detection system. No evidence of systematic effects are visible, as expected from the C_6D_6 detection set-up.

6.3.2 Comparison with TAC data

As described in Chapter 1, the measurement of ^{238}U(n,γ) cross section at n_TOF with C_6D_6 scintillators is part of a larger proposal, which includes also a measurement with the n_TOF Total Absorption Calorimeter.

To verify that the two analysis could contribute to improve the present accuracy of resonance parameters we followed the same procedure of the comparison with ENDF/B-

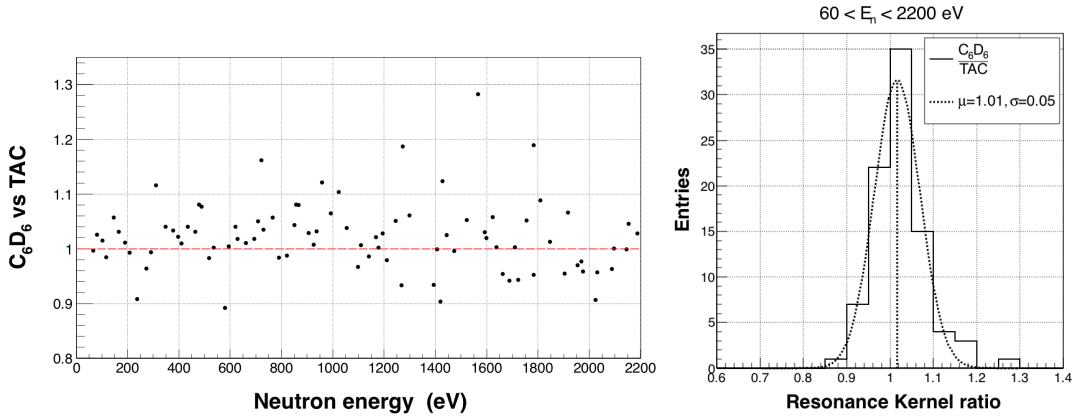

Fig. 6.9: Left panel: C_6D_6 over TAC resonance kernels as a function of resonance energies. No systematic effect are present. Right panel: Statistical distribution of resonance kernel ratios.

VII.1 and JEFF-3.2 libraries. We studied the ratio of C_6D_6 over TAC resonance kernels as a function of resonance energy, and afterwards the statistical distribution of the ratios themselves. The results are shown in Figure 6.9. The fitting procedure used to analyze TAC data is not exactly the same used for C_6D_6, and therefore it is possible that differences in the absolute values are due to some consequent effects. Anyway, the kernel ratios have a very sharp gaussian distribution with a very small standard deviation $\sigma = 0.05$. The distribution is centered in $\mu = 1.01$, showing that no systematic effect is present.

As described in the previous section, to check for systematic effects we plotted resonance kernel ratios as a function of resonance kernels (Figure 6.10) and of $g\Gamma_n/\Gamma_\gamma$ ratio (Figure 6.11).

In Figure 6.10 the ratios show an average good agreement between the two data sets. Some small tendencies cannot be excluded, however they can be due either to differences in the fitting procedure or to residual systematic effect (as it seems to be in Figure 6.11). Thus these ratios are not conclusive enough and further investigations are needed for the final comparison between TAC and C_6D_6 data.

From this analysis we can conclude that both the measurement are extremely accurate, and can be combined together so to solve statistics problems related to the C_6D_6 measurement for small resonances and neutron sensitivity issue of the TAC detector for resonances with very large Γ_n. In this way they can contribute to the reduction of the cross section uncertainty down to the required 2%.

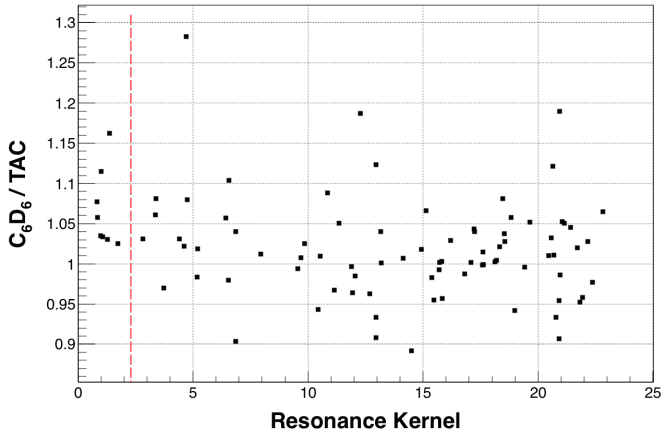

Fig. 6.10: C_6D_6 over TAC resonance kernels as a function of resonance kernels. For $\kappa < 2.3$ meV C_6D_6 data stay systematically above TAC ones, probably because thanks to the higher statistics data obtained with the calorimeter can properly fit also very small resonances.

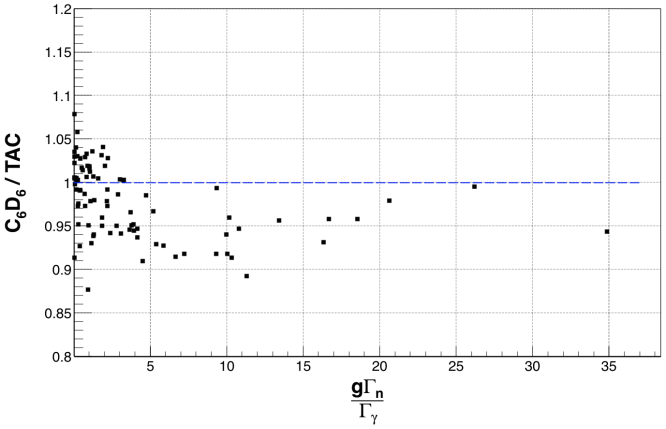

Fig. 6.11: C_6D_6 over TAC resonance kernels over the ratio $g\Gamma_n/\Gamma_\gamma$. For resonances with large Γ_n, it seems that TAC data lays slightly below C_6D_6 ones.

6.4 Analysis of the URR

When the resonance widths become comparable to the level distance it is not possible anymore to analyze the cross section through a RSA. In this region, referred to as Unresolved Resonance Region, the analysis procedure for the extraction of the capture cross section from the measured yield is based on average parameters. In this work the analysis of the URR starts from energies $E_n = 3$ keV up to $E_n = 480$ keV (the explanation of the upper energy limit can be found in Section 5.4.3).

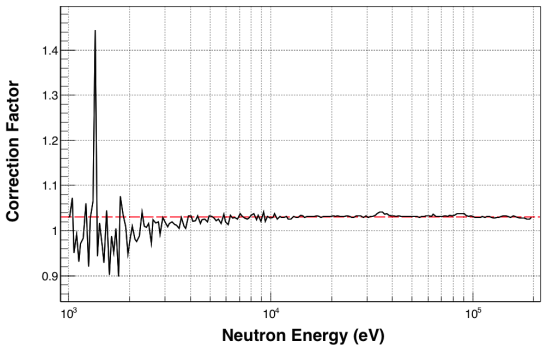

Fig. 6.12: Correction factor for the sample-related effects, i.e. self-shielding and multiple scattering, obtained from MCNP simulations. The red line points out the 3% level.

To extract the cross section the thin-sample approximation of Eq. 4.6 is used. At high energies, in fact, the total cross section become quite low ($\sigma_{\text{tot}} \sim 1$ barn) and, as the areal density is $n = 9.56 \times 10^{-4}$ at/barn, the condition $n\sigma_{\text{tot}} \ll 1$ is fulfilled. The sample-related effects, such as the self-shielding and the multiple scattering, are taken into account applying a correction factor obtained from Monte Carlo MCNP simulations. The correction factor CF depends on the neutron energy and is shown in Figure 6.12 as a function of incident neutron energy from 1 keV to 200 keV. As the resonance structure becomes negligible, i.e. from $E_n = 3$ keV, the correction factor is almost constant and leads to a $\sim 3\%$ increase of the measured values. Therefore, the capture cross section is extracted from the measured yield as:

$$\sigma_\gamma = \frac{Y_c}{n} \times CF. \tag{6.4}$$

Within the following plots the uncertainty shown are only statistical, to which the correlated ones must be added. In Table 6.3 the average capture cross section and total uncertainty derived from the data analyzed in this work are presented. Correlated uncertainties are separated in all the different components listed in Table 6.1.

Table 6.3: Average capture cross section ($\overline{\sigma}_\gamma$) and total uncertainty derived from the data analyzed in this work. The counting statistic uncertainty is listed in column 5, while in columns from 6 to 9 the correlated uncertainties summarized in Table 6.1 are listed. The correction factor of Figure 6.12 is given in column 3.

E_{low} (keV)	E_{high} (keV)	$\overline{\sigma}_\gamma$ (mb)	CF	$u_{\overline{\sigma}_\gamma}$ (mb)	u_{mass} (mb)	u_{flux} (mb)	u_{norm} (mb)	u_{bkg} (mb)
3	4	1315	1.0063	16.53	0.3947	26.31	13.15	26.31
4	5	979.6	1.0154	17.41	0.2939	19.59	9.796	19.59

Table 6.3: Average capture cross section ($\overline{\sigma}_\gamma$) and total uncertainty derived from the data analyzed in this work. The counting statistic uncertainty is listed in column 5, while in columns from 6 to 9 the correlated uncertainties summarized in Table 6.1 are listed. The correction factor of Figure 6.12 is given in column 3.

E_{low} (keV)	E_{high} (keV)	$\overline{\sigma}_\gamma$ (mb)	CF	$u_{\overline{\sigma}_\gamma}$ (mb)	u_{mass} (mb)	u_{flux} (mb)	u_{norm} (mb)	u_{bkg} (mb)
5	6	1006	1.0238	20.34	0.3020	20.13	10.06	20.13
6	7	947.8	1.0277	20.68	0.2843	18.95	9.478	18.95
7	8	917.8	1.0262	21.99	0.2753	18.35	9.178	18.35
8	9	753.0	1.0241	21.31	0.2259	15.06	7.530	15.06
9	10	757.5	1.0223	21.72	0.2273	15.15	7.575	15.15
10	11	697.3	1.0362	21.50	0.2092	31.37	6.973	13.94
11	12	662.3	1.0291	22.57	0.1987	29.80	6.623	13.24
12	13	657.7	1.0247	23.52	0.1973	29.59	6.577	13.15
13	14	738.1	1.0287	23.94	0.2214	33.21	7.381	14.76
14	15	639.4	1.0313	23.88	0.1918	28.77	6.394	12.78
15	16	629.2	1.0299	24.44	0.1888	28.31	6.292	12.58
16	17	624.5	1.0300	25.07	0.1874	28.10	6.245	12.49
17	18	637.2	1.0296	24.93	0.1912	28.67	6.372	12.74
18	19	574.5	1.0299	24.80	0.1724	25.85	5.745	11.49
19	20	600.8	1.0295	25.60	0.1802	27.03	6.008	12.01
20	21	566.6	1.0314	25.19	0.1700	25.49	5.666	11.33
21	22	510.2	1.0310	24.75	0.1531	22.96	5.102	10.20
22	23	496.6	1.0303	24.37	0.1490	22.34	4.966	9.932
23	24	460.9	1.0305	23.57	0.1383	20.74	4.609	9.218
24	25	464.9	1.0303	24.92	0.1395	20.92	4.649	9.298
25	28	486.3	1.0307	14.60	0.1459	21.88	4.863	9.726
28	31	467.8	1.0315	13.76	0.1404	21.05	4.678	9.356
31	34	466.3	1.0319	17.99	0.1399	20.98	4.663	9.326
34	37	470.7	1.0408	28.13	0.1412	21.18	4.707	9.415
37	40	401.6	1.0338	20.92	0.1205	18.07	4.016	8.033
40	43	412.5	1.0304	18.00	0.1238	18.56	4.125	8.250
43	46	387.2	1.0306	17.00	0.1162	17.42	3.872	7.744
46	49	349.6	1.0302	16.07	0.1049	15.73	3.496	6.992
49	52	337.2	1.0309	15.99	0.1012	15.17	3.372	6.744
52	55	299.9	1.0304	15.11	0.0900	13.49	2.999	5.998
55	58	288.0	1.0308	15.53	0.0864	12.96	2.880	5.760
58	61	272.2	1.0319	14.91	0.0817	12.25	2.722	5.445
61	64	269.0	1.0297	13.94	0.0807	12.10	2.690	5.381

Table 6.3: Average capture cross section ($\overline{\sigma}_\gamma$) and total uncertainty derived from the data analyzed in this work. The counting statistic uncertainty is listed in column 5, while in columns from 6 to 9 the correlated uncertainties summarized in Table 6.1 are listed. The correction factor of Figure 6.12 is given in column 3.

E_{low} (keV)	E_{high} (keV)	$\overline{\sigma}_\gamma$ (mb)	CF	$u_{\overline{\sigma}_\gamma}$ (mb)	u_{mass} (mb)	u_{flux} (mb)	u_{norm} (mb)	u_{bkg} (mb)
64	67	242.0	1.0315	13.90	0.0726	10.89	2.420	4.840
67	70	240.6	1.0304	14.10	0.0722	10.82	2.406	4.812
70	73	226.8	1.0310	13.93	0.0681	10.20	2.268	4.537
73	76	204.7	1.0311	13.42	0.0614	9.215	2.047	4.095
76	79	214.8	1.0328	14.00	0.0645	9.668	2.148	4.296
79	82	239.2	1.0333	15.95	0.0718	10.76	2.392	4.784
82	85	225.3	1.0362	18.71	0.0676	10.14	2.253	4.507
85	88	220.1	1.0378	20.62	0.0660	9.906	2.201	4.403
88	91	221.2	1.0371	19.50	0.0664	9.958	2.213	4.425
91	94	220.4	1.0344	18.30	0.0661	9.918	2.204	4.408
94	97	214.9	1.0309	16.88	0.0645	9.671	2.149	4.298
97	100	212.8	1.0324	15.73	0.0639	9.579	2.128	4.257
100	105	230.7	1.0292	13.38	0.0692	4.615	2.307	11.53
105	110	230.1	1.0288	13.97	0.0690	4.603	2.301	11.50
110	115	211.3	1.0293	13.23	0.0634	4.226	2.113	10.56
115	120	207.0	1.0293	14.26	0.0621	4.141	2.070	10.35
120	125	194.4	1.0296	13.43	0.0583	3.888	1.944	9.720
125	130	180.7	1.0276	11.10	0.0542	3.615	1.807	9.037
130	135	187.8	1.0282	11.15	0.0563	3.756	1.878	9.390
135	140	218.4	1.0293	13.78	0.0655	4.368	2.184	10.92
140	145	196.3	1.0317	15.53	0.0589	3.927	1.964	9.819
145	150	191.1	1.0318	15.11	0.0573	3.822	1.911	9.556
150	155	191.2	1.0296	15.00	0.0574	3.824	1.912	9.562
155	160	197.8	1.0312	15.85	0.0594	3.958	1.979	9.895
160	165	187.8	1.0303	14.42	0.0563	3.756	1.878	9.390
165	170	178.8	1.0282	13.48	0.0537	3.577	1.788	8.942
170	175	164.8	1.0272	12.13	0.0494	3.296	1.648	8.241
175	180	160.9	1.0265	11.38	0.0483	3.218	1.609	8.045
180	185	158.1	1.0262	11.15	0.0475	3.163	1.581	7.908
185	190	147.8	1.0256	11.21	0.0444	2.957	1.478	7.392
190	195	153.0	1.0261	11.35	0.0459	3.061	1.530	7.654
195	200	160.3	1.0300	11.54	0.0481	3.207	1.603	8.018
200	205	149.3	1.0300	12.07	0.0448	2.986	1.493	7.467

Table 6.3: Average capture cross section ($\overline{\sigma}_\gamma$) and total uncertainty derived from the data analyzed in this work. The counting statistic uncertainty is listed in column 5, while in columns from 6 to 9 the correlated uncertainties summarized in Table 6.1 are listed. The correction factor of Figure 6.12 is given in column 3.

E_{low} (keV)	E_{high} (keV)	$\overline{\sigma}_\gamma$ (mb)	CF	$u_{\overline{\sigma}_\gamma}$ (mb)	u_{mass} (mb)	u_{flux} (mb)	u_{norm} (mb)	u_{bkg} (mb)
205	210	142.9	1.0300	12.36	0.0429	2.858	1.429	7.147
210	215	142.2	1.0300	11.27	0.0427	2.845	1.422	7.113
215	220	142.0	1.0300	10.92	0.0426	2.841	1.420	7.103
220	225	140.8	1.0300	11.26	0.0423	2.817	1.408	7.043
225	230	140.5	1.0300	11.34	0.0422	2.811	1.405	7.029
230	235	139.2	1.0300	10.65	0.0418	2.784	1.392	6.962
235	240	138.8	1.0300	10.43	0.0417	2.776	1.388	6.941
240	245	148.2	1.0300	10.54	0.0445	2.964	1.482	7.410
245	250	153.7	1.0300	10.61	0.0461	3.074	1.537	7.686
250	255	145.2	1.0300	10.22	0.0436	2.904	1.452	7.261
255	260	132.2	1.0300	9.593	0.0397	2.644	1.322	6.610
260	265	133.8	1.0300	9.664	0.0401	2.676	1.338	6.690
265	270	159.7	1.0300	10.75	0.0479	3.194	1.597	7.985
270	275	159.7	1.0300	10.75	0.0479	3.194	1.597	7.985
275	280	150.0	1.0300	11.52	0.0450	3.002	1.501	7.504
280	285	144.0	1.0300	11.98	0.0432	2.881	1.440	7.203
285	290	143.8	1.0300	11.94	0.0432	2.877	1.438	7.192
290	295	140.4	1.0300	11.15	0.0421	2.808	1.404	7.020
295	300	140.4	1.0300	11.15	0.0421	2.808	1.404	7.020
300	305	136.1	1.0300	11.01	0.0409	2.723	1.361	6.809
305	310	129.5	1.0300	10.79	0.0389	2.590	1.295	6.477
310	315	129.5	1.0300	10.79	0.0389	2.590	1.295	6.477
315	320	127.0	1.0300	10.66	0.0381	2.541	1.270	6.354
320	325	125.4	1.0300	10.57	0.0376	2.508	1.254	6.270
325	330	125.4	1.0300	10.57	0.0376	2.508	1.254	6.270
330	335	120.0	1.0300	9.823	0.0360	2.400	1.200	6.001
335	340	117.4	1.0300	9.439	0.0352	2.349	1.174	5.872
340	345	117.4	1.0300	9.439	0.0352	2.349	1.174	5.872
345	350	126.3	1.0300	10.28	0.0379	2.526	1.263	6.316
350	355	131.7	1.0300	10.75	0.0395	2.634	1.317	6.586
355	360	131.7	1.0300	10.75	0.0395	2.634	1.317	6.586
360	365	120.7	1.0300	10.50	0.0362	2.415	1.207	6.039
365	370	106.2	1.0300	10.14	0.0319	2.125	1.062	5.313

Table 6.3: Average capture cross section ($\overline{\sigma}_\gamma$) and total uncertainty derived from the data analyzed in this work. The counting statistic uncertainty is listed in column 5, while in columns from 6 to 9 the correlated uncertainties summarized in Table 6.1 are listed. The correction factor of Figure 6.12 is given in column 3.

E_{low} (keV)	E_{high} (keV)	$\overline{\sigma}_\gamma$ (mb)	CF	$u_{\overline{\sigma}_\gamma}$ (mb)	u_{mass} (mb)	u_{flux} (mb)	u_{norm} (mb)	u_{bkg} (mb)
370	375	106.2	1.0300	10.14	0.0319	2.125	1.062	5.313
375	380	107.0	1.0300	10.10	0.0321	2.141	1.070	5.354
380	385	114.9	1.0300	9.702	0.0345	2.299	1.149	5.749
385	390	114.9	1.0300	9.702	0.0345	2.299	1.149	5.749
390	395	114.9	1.0300	9.702	0.0345	2.299	1.149	5.749
395	400	123.5	1.0300	10.81	0.0371	2.470	1.235	6.177
400	405	129.1	1.0300	11.48	0.0387	2.582	1.291	6.455
405	410	129.1	1.0300	11.48	0.0387	2.582	1.291	6.455
410	415	129.1	1.0300	11.48	0.0387	2.582	1.291	6.455
415	420	128.1	1.0300	13.58	0.0384	2.562	1.281	6.405
420	425	128.0	1.0300	13.66	0.0384	2.561	1.280	6.403
425	430	128.0	1.0300	13.66	0.0384	2.561	1.280	6.403
430	435	122.4	1.0300	13.40	0.0367	2.448	1.224	6.121
435	440	90.16	1.0300	11.78	0.0270	1.803	0.901	4.508
440	445	90.16	1.0300	11.78	0.0270	1.803	0.901	4.508
445	450	90.16	1.0300	11.78	0.0270	1.803	0.901	4.508
450	455	88.65	1.0300	11.42	0.0266	1.773	0.886	4.432
455	460	81.04	1.0300	9.364	0.0243	1.621	0.810	4.052
460	465	81.04	1.0300	9.364	0.0243	1.621	0.810	4.052
465	470	81.04	1.0300	9.364	0.0243	1.621	0.810	4.052
470	475	81.09	1.0300	9.363	0.0243	1.621	0.811	4.054
475	480	103.91	1.0300	8.66	0.0312	2.078	1.039	5.195

The ^{238}U capture cross section from this work is compared to evaluated libraries and previous measurement (retrieved from the EXFOR database) in Figure 6.13. From the figure it is possible to distinguish two different region:

$3 < E_n < 80$ keV. C_6D_6 data are in good agreement with measurement by Moxon, and they stay slightly above the evaluated libraries.

$80 < E_n < 480$ keV. All the data-sets starts to deviate from the libraries being higher than evaluated data, apart from Lindner [88] and, for $E_n > 200$ keV, from Fricke [68].

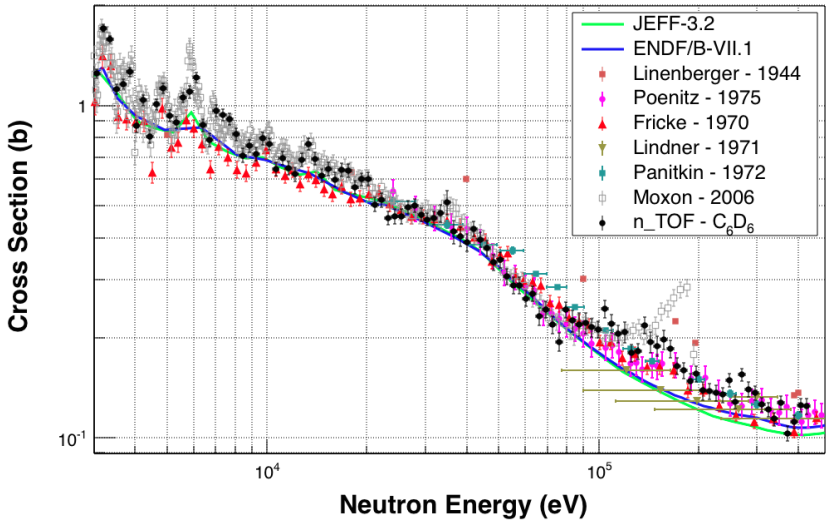

Fig. 6.13: Measured ^{238}U(n,γ) cross section (black) compared to previous measurements by Lienenberger [67], Poenitz [70], Fricke [68], Lindner [88], Panitkin [69], Moxon [85]. JEFF-3.2 and ENDF/B-VII.1 are plotted as continuos lines for comparison.

C_6D_6 data suffers from the big Al resonances at $E_n = 34.83$ keV, $E_n = 86.27$ eV, $E_n = 120.00$ eV and $E_n = 158.73$ eV, which produce a peak-behaviour in the cross section. Data in the neighbourhood of these energies are therefore not reliable. Nevertheless, it is clear that our data are systematically above other measurements apart from Moxon, laying significantly above the evaluated libraries.

In Figure 6.14 a more detailed comparison of the first energy region is shown. From left panel it is visible that our data are in very good agreement with the measurement by Moxon [85], while they differ slightly from Fricke [68]. In the right panel the ratio of C_6D_6 over Moxon confirms the agreement between the data-sets, while the ratios with JEFF-3.2 and ENDF/B.VII.1 clearly show that the measured cross section stays $\sim 5 - 15\%$ above the evaluated ones.

As outlined, in the higher energy region from 80 keV to 480 keV it is visible that the data from this work stays above other measurements. Figure 6.15 shows a more detailed comparison between C_6D_6 data with Moxon [85], Poenitz [70], Lindner [88], Fricke [68] and Panitkin [69]. The incorrect determination of the cross section in the neighbourhood of Al resonances clearly shows up with the presence of bumps between 100 and 200 keV. In Figure 6.16 the ratios between our data and Fricke and Poenitz is plotted together with the ratios over evaluated libraries. The shadowed regions are the untrustworthy ones because of the presence of Al resonances. Data from this work are in quite good agreement with Poenitz, while they are more than 10% above Fricke.

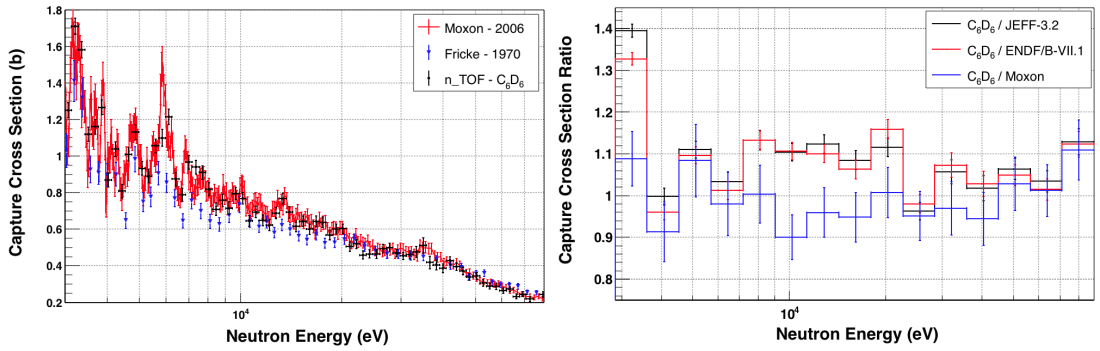

Fig. 6.14: Measured ^{238}U(n,γ) cross section (black) in the energy range $3 < E_n < 80$ keV. Left panel: n_TOF data compared to Moxon [85] and Fricke [68]. Right panel: Ratios between this work and Moxon (blue), JEFF-3.2 (red) and ENDF/B-VII.1 (black).

The figure shows also the ratio of C_6D_6 data over JEFF-3.2 and ENDF/B-VII.1, and it results that evaluated cross sections are more than 20% lower with respect of measured one.

As described in Chapter 1, this work is part of a larger proposal [2] which comprehends three independent measurement of ^{238}U(n,γ) cross section. The cross sections in the URR measured at n_TOF with C_6D_6 and TAC, and at GELINA with C_6D_6 are shown in Figure 6.17, where also the JEFF-3.2 evaluated cross section is plotted for comparison. From the ratios between the three data sets, plotted in Figure 6.18, it is visible that the two n_TOF data sets are in very good agreement between themselves (within $\pm$5%), while GELINA results lays systematically below.

From this analysis we can conclude that this measurement confirms the very high quality measurement by Moxon up to $E_n = 80$ keV, and gives precise results for neutron energies up to 480 keV. Moreover, the high precision data obtained at n_TOF with C_6D_6 and TAC agrees within few percents. The comparison between this work and both JEFF-3.2 and ENDF/B-VII.1 libraries suggests that the evaluations are underestimating the capture cross section in the URR, and gives therefore strong indications that a deep investigation is needed.

6.5 Summary

The ^{238}U(n,γ) yield obtained following the procedure explained in Chapter 5 has been analyzed to extract capture cross section.

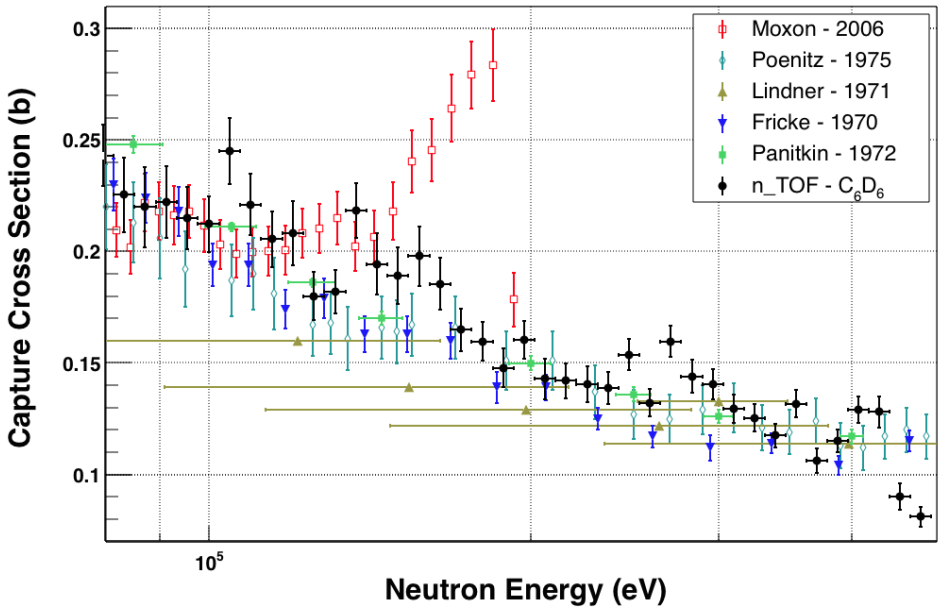

Fig. 6.15: Measured ^{238}U(n,γ) cross section (black) in the energy range 80 < E_n > 480 keV: data from this work compared to Moxon [85], Poenitz [70], Lindner [88], Fricke [68] and Panitkin [69].

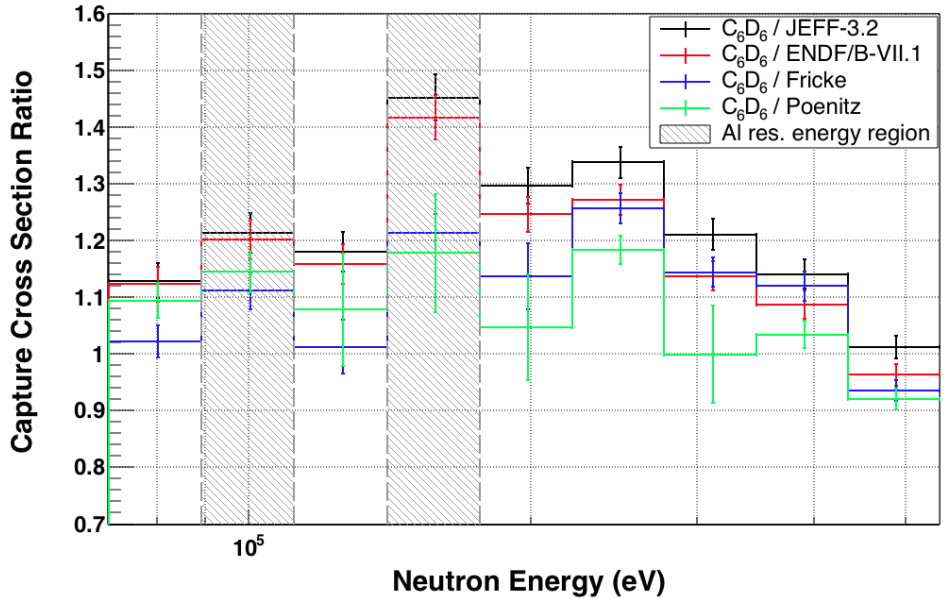

Fig. 6.16: Measured ^{238}U(n,γ) cross section (black) in the energy range 80 < E_n > 480 keV: ratios between this work and Fricke (blue), Poenitz (green), JEFF-3.2 (red) and ENDF/B-VII.1 (black).

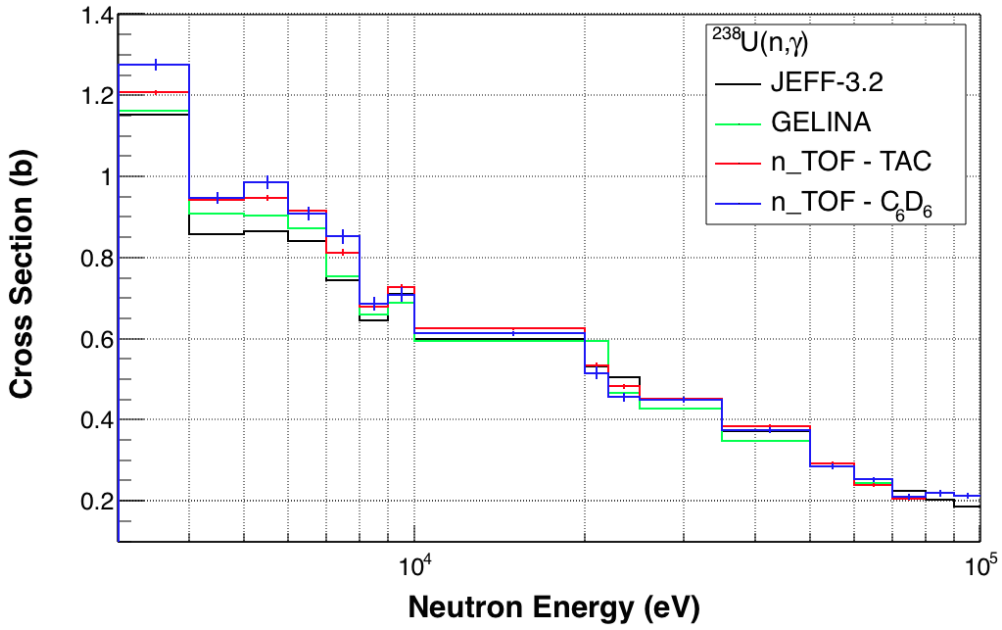

Fig. 6.17: Comparison between the three measurement parto of the proposal on ^{238}U radiative capture measurement [2] in the URR. Data from JEFF-3.2 library are plotted for comparison.

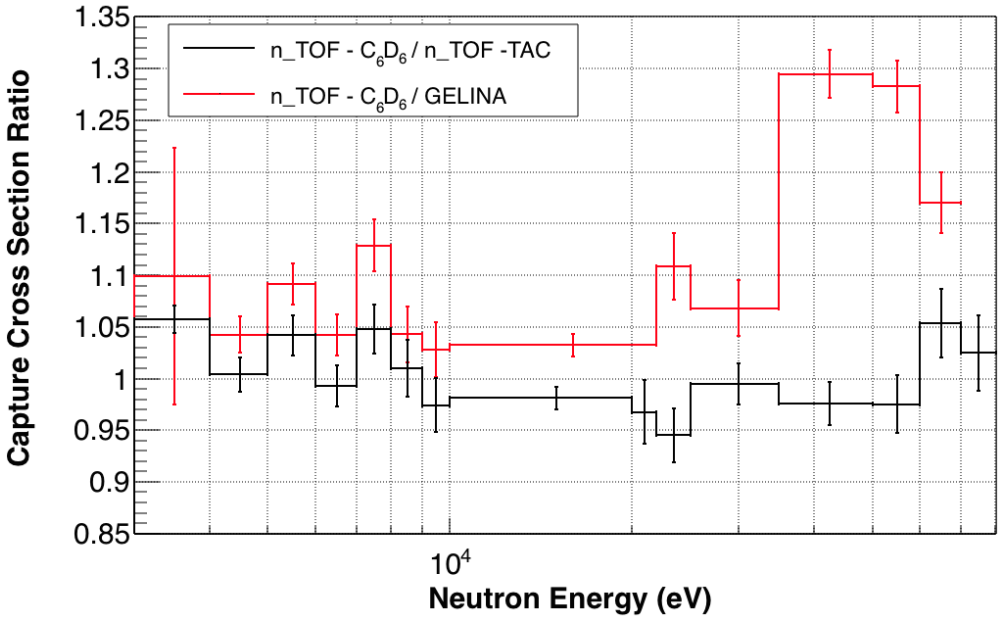

Fig. 6.18: Ratio of this work over TAC data (black) and data from GELINA (red).

In this work the Resolved Resonance Region of ^{238}U(n,γ) reaction has been located for incident neutron energies below 3 keV, and the cross section has been given in terms of resonance parameters. The parameters are obtained analyzing the data with the resonance shape analysis code SAMMY, which in its fitting procedure takes into account experimental effects, namely self-shielding, multiple scattering, Doppler and experimental broadening. A careful comparison has been made between our data and evaluated ones, which shows that very accurate data are provided.

The Unresolved Resonance Region has been analyzed in this work for incident neutron energies 3 keV $< E_n <$ 480 keV. Here the cross section is directly extracted from capture yield, and it is compared with other measurements and evaluations. It has been shown that our results are in good agreement with other measurements (in particular, with Moxon [85] up to E_n = 80 keV and with Poenitz [70] for 80 $< E_n <$ 480 keV), but they are systematically above the cross section presented in the JEFF-3.2 and ENDF/B-VII.1 evaluations.

The good quality of the cross section derived from the data analyzed in this work has been tested through a comparison with the data obtained at n_TOF with the Total Absorption Calorimeter. The two techniques are based on different measurement principles, and complements each other. Both in the resolved and unresolved resonance region the two measurements agrees between themselves within $\pm$5%, confirming the accuracy of the data provided and indicating that the two data-sets combined together could contribute to approach the final goal of a 1% to 3% uncertainty in the cross section.

Conclusions

The assessment of global energy resources states that fossil fuels as coal, oil and gas, enhanced by new extraction technologies, are plentiful and will last for decades. Nevertheless, the increasing problems in climate change, pollution and security imply a deep and almost total transformation of the world's energy system. Several scenarios have been studied, depending on philosophical principles of economical rationalism or environmentalism. Among them, the share of nuclear power, particularly in regional energy mix, appears as a practicable, reliable and available option to reduce greenhouse-gas emissions while improving energy security and adding stability to electricity costs.

Despite the tendency of OECD countries to phase-out nuclear, enhanced after the Fukushima accident in Japan, a significant effort towards improved reactor technologies is ongoing, with the development of new reactor concepts, intrinsically safe and with the capacity to burn radioactive waste. These technologies are especially focused on reactor operating with a fast neutron spectrum, because of their more efficient use of nuclear fuel and their capacity to fission transuranic elements present in radioactive waste. Six different reactor concepts, with both critical and supercritical technologies, are under development in the context of the Generation-IV International Forum (GIF). Moreover, different prototypes of a sub-critical device, consisting in a sub-critical reactor coupled to an external source of neutrons given by a particle accelerator and a spallation target, are being built in Europe (MYRRHA in Belgium and ESS in Sweden), Japan (KUCA) and India.

Neutron-nucleus reactions play a major role in the design and calculations of critical and subcritical nuclear systems, governing the behaviour of the reactor core. Capture and fission cross-section data are fundamental for calculations of reactor parameters as the multiplication factor, the power peak (i.e. the ratio between the maximum and the average peak density), the reactivity coefficients (i.e. the deflection of reactors from critical state), the nuclear density variation of isotopes due to transmutation and the

decay heat. Experimental nuclear data are available through different databases (e.g. EXFOR), and collected by several collaborating nuclear data agencies worldwide to form the nuclear data libraries. Nevertheless, the development of new reactor concepts and fuel cycles, and nuclear reactors applications for radioactive waste transmutation, have made clear that existing nuclear data are not always of good quality and in some cases are still lacking.

The role of the ^{238}U(n,γ) reaction cross-section is of extreme importance for the calculations of fast and thermal reactor parameters, being ^{238}U the main constituent of nuclear fuel. Moreover, the safety of nuclear reactors depends on the ^{238}U neutron capture cross-section both during their operating life and in terms of nuclear-weapons proliferation, because it determines the density of plutonium isotopes at the end of fuel cycles. The importance of this cross section led to several experimental measurements, but inconsistencies are still present, specifically in the high energy region, up to 15%. Moreover, the ENDF/B-VII evaluation [114] made some small modifications to the standard capture results that exceeded the uncertainties of the standards evaluation, and needs therefore to be further investigated. In addition, the nuclear data uncertainty assessment performed by WPEC Subgroup 26 for innovative reactor systems shows that the uncertainty in the radiative capture cross-section of ^{238}U should be further reduced to 1-3% in the energy range from 20 eV to 25 keV.

For all these reasons, the Nuclear Energy Agency inserted the reduction on the ^{238}U(n,γ) cross-section uncertainty as a primary nuclear data need. Because such an accuracy level is difficult to be obtained from results of a single measurement, independent experiments were scheduled at the GELINA (JRC-EU-IRMM laboratory, Belgium) and n_TOF (CERN, Switzerland) facilities.

This work aimed at providing a very accurate and precise ^{238}U radiative capture cross-section starting from the data collected at n_TOF with C_6D_6 scintillators. To this purpose, an extremely pure and well-characterized sample has been used in combination with an optimized detection setup very transparent to sample-scattered neutrons. Thanks to the well-suited detection system and the features of the facility, the capture cross-section on ^{238}U has been studied from 1 eV to 480 keV.

To fulfil the requirements of precision and accuracy, each step of the analysis procedure from the raw data to the experimental yield has been followed with extreme attention. Particular effort has been devoted to the subtraction of the background, since it has, together with the uncertainty associated to the incident neutron flux, the strongest influence on the cross-section uncertainty. The level and the shape of the background have been studied with two independent methods, whose results shows a 2% to 10% deviation. Their difference is an estimation of the uncertainty in the level of background, and it is

propagated to the final capture yield depending on the signal to background ratio (for 1 eV $< E_n <$ 3 keV, $S/B \gtrsim 10$ in resonance peaks, while for higher energies $S/B \sim 2$). Another important source of uncertainty is the normalization of the experimental yield. In this work, the saturated resonance technique has been applied, which permits to eliminate the error due to sample alignment and to correct for the effective absolute value of the neutron flux. Moreover, we exploited three ^{238}U(n,γ) saturated resonances, which means that the yield is self-normalized with a consequent drastic reduction of the related uncertainty.

Once obtained the ^{238}U(n,γ) experimental yield, it has been analyzed to extract capture cross-section. In this work the Resolved Resonance Region (RRR) has been located for incident neutron energies below 3 keV, and the cross section has been given in terms of resonance parameters. The parameters are obtained analyzing the data with the resonance shape analysis code SAMMY that takes into account experimental effects, namely self-shielding, multiple scattering, Doppler and experimental broadening. A careful comparison has been made between our data and evaluated ones, which shows that very accurate data are provided. Moreover, a comparison with the data obtained at n_TOF with the Total Absorption Calorimeter points out that the two data-sets combined together could contribute to approach the final goal of a 2% uncertainty in the cross section. The two techniques have in fact complementary characteristics that helps to eliminate systematic uncertainties from both the measurements.

The Unresolved Resonance Region (URR) has been analyzed in this work for incident neutron energies between 3 keV and 480 keV. Here the cross section is directly extracted from capture yield applying a correction factor to take into account self-shielding and multiple scattering effects. The results from this work are compared with other measurements and evaluations. A good agreement has been shown between this work and previous measurements, in particular with the ones by Moxon (up to $E_n = 80$ keV) and by Poenitz (for $80 < E_n <$ 480 keV). In addition, a preliminary comparison with the data obtained at n_TOF with the Total Absorption Calorimeter is possible for incident neutron energies up to 80 keV, showing that the two data sets are in very good agreement (within $\pm$5%). On the contrary, the comparison with evaluations shows that the cross section obtained from this work is systematically higher than the cross sections reported in major libraries such as JEFF-3.2 and ENDF/B-VII.1.

The extreme accurate data reduction performed led to very high-quality data for the radiative capture cross-section on ^{238}U. The results obtained in this work show a general agreement with nuclear data libraries, but nevertheless differences are present, in particular in the high-energy URR. Because of the great importance of a precise knowledge of this cross-section, as previously outlined, with the requirement of an uncertainty between

1% and 3% in the energy range from 20 eV to 25 keV, these results suggest that a deep investigation to understand the reason of these discrepancies is needed. Furthermore, when inserted in new evaluations, the good quality cross-section data from this work will help to reach the requirements of precision and accuracy demanded by new nuclear technologies.

Appendix A
Statistical properties of the resonance parameters

The study of the statistical properties of the resonance parameters describing the cross section in the RRR are of key importance to:

(i) test the consistency among reaction and total cross-section, taking into account all the physical constraints they are linked by;
(ii) collect the information from isolated resonances for its use in the description of the cross sections at higher neutron energies.

In the case of heavy nuclei with a large number of nuclear levels below the neutron separation energy S_n, the quasi-stationary levels above S_n show the characteristic features of the statistical model. In other words, the properties of the nuclear levels in the compound nucleus excited by incident neutrons have typical characteristics resulting from the random nature of matrix elements governing the nuclear transitions. The basic assumption for the statistical model is that the compound nucleus states are so complex that the values of the nuclear matrix elements have a Gaussian distribution with zero mean.

A.1 Resonance widths distribution

The resonance widths Γ_λ of each quasi-stationary level λ are defined (see Eq. 2.24) by the penetrability factor P_α and the reduced width amplitudes $\gamma_{\lambda\alpha}$ as

$$\Gamma_{\lambda c} = \sum_{\alpha=1}^{\nu} 2P_\alpha \gamma_{\lambda\alpha}^2 \tag{A.1}$$

where ν is the number of the possible decay modes c' for a given entrance channel c, and $\gamma_{\lambda\alpha}$ is known to follow a Gaussian distribution.

Assuming that P_α is nearly constant in the energy range under study and that $\langle \gamma_{\lambda\alpha} \rangle$ is constant for each level λ decaying via the mode α, the distribution of widths $\Gamma_{\lambda c}$ is given by a χ^2 distribution with ν degrees of freedom [104]

$$P(x,\nu)\,\mathrm{d}x = \frac{\nu/2}{\Gamma(\nu/2)} \left(\frac{\nu}{2}\, x\right)^{-\frac{\nu}{2}-1} \mathrm{e}^{-\frac{\nu}{2}x}\,\mathrm{d}x \tag{A.2}$$

$$x = \frac{\gamma_{\lambda c}^2}{\langle \gamma_{\lambda c}^2 \rangle} = \frac{\Gamma_{\lambda c}}{\langle \Gamma_{\lambda c} \rangle} \tag{A.3}$$

with mean value 1 and variance $2/\nu$. In the case of one-channel neutron scattering reactions the distribution for the normalized reduced neutron widths x for $\ell = 0$ resonances (i.e. s-waves) is also called Porter-Thomas distribution

$$P_{\mathrm{PT}}(x)\,\mathrm{d}x = \frac{1}{\sqrt{2\pi x}} \mathrm{e}^{-\frac{x}{2}}\,\mathrm{d}x. \tag{A.4}$$

The radiative width $\Gamma_{\lambda\gamma}$ for heavy nuclei is instead expected to be the sum of several partial widths $\Gamma_{\lambda\gamma i}$, where i indicates the nuclear levels below S_n. In the limit of infinite partial widths the χ^2 distribution turns into a Dirac delta function, which implies that all radiation widths have a constant value

$$\Gamma_{\lambda\gamma} = \Gamma_{\mu\gamma} = \sum_i \Gamma_{\lambda\gamma i} = \langle \Gamma_\gamma \rangle. \tag{A.5}$$

This constant behaviour of the radiative width for heavy nuclei can be also understood from the fact the number of primary transition from a level λ or from a higher energy level μ are practically the same.

The neutron induced fission can be considered as a few channels process. Hence its width distribution should follow a χ^2 with a few degrees of freedom. The value of ν is fitted from experimental data and usually found between 2 and 3.

Practically it is more convenient, instead of matching these distributions with observed data, to use a reverse cumulative distribution and compare the number of resonances with a value of $x = \Gamma_{\lambda c}/\langle \Gamma_{\lambda c} \rangle$ larger than a threshold value x_{th}

$$N(x_{th}) = N_0 \int_{x_{th}}^{\infty} P(x,\nu)\,\mathrm{d}x, \tag{A.6}$$

where the value N_0 gives the real number of resonances in the energy region considered. At low thresholds resonances are generally missing and the data deviates from the expectation. At higher threshold values, the observed data should be in agreement with the integrated distribution. This is illustrated in Figure A.1.

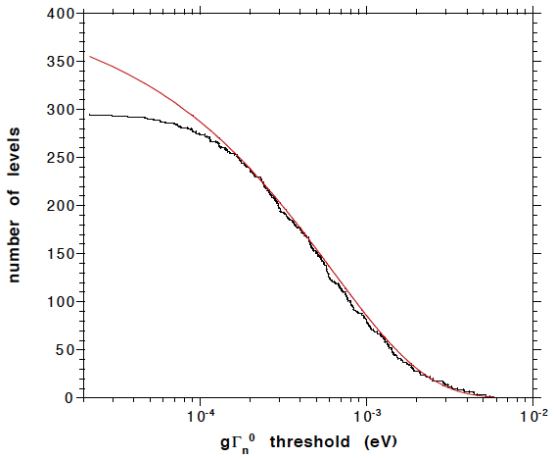

Fig. A.1: An example of the integrated number of levels above a threshold value of the neutron width together with the prediction of equation A.6. Figure from [100].

A.2 Level spacings

The distribution of observed resonances as a function of neutron energy is directly related to the level density of the compound nucleus at the neutron separation energy. The level density ρ^J can be calculated from the number of observed resonances N^J of a given spin J in an energy interval ΔE_n as

$$\rho^J = \frac{N^J}{\Delta E_n} = \frac{1}{\langle D^J \rangle} \tag{A.7}$$

where $\langle D^J \rangle$ is the average level spacing for a given spin J. There are several theoretical models aimed at the prediction of nuclear level densities as a function of the mass number that usually include shell and pairing effects [174].

The spacing between consecutive resonances for the same total angular momentum and parity should also exhibit a random behaviour that can be tested experimentally. For a set of N consecutive resonances with energies E_i, the level spacing is defined as $D_i = E_i - E_{i-1}$ and its probability distribution function should follow a distribution close to the Wigner one

$$P_{\mathrm{W}}(x)\,\mathrm{d}x = \frac{\pi}{2} x\ \mathrm{e}^{-\frac{\pi}{4}x^2} \tag{A.8}$$

$$x = \frac{D}{\langle D \rangle}. \tag{A.9}$$

The Wigner law, which corresponds to the limiting case for a chaotic system, was the first mathematical prediction of the level spacing to provide excellent agreement with the

experimental results. An interesting feature is that the distribution goes to zero for small x, i.e. for small separations between levels, which is known as the repulsion effect and reflects the fact that small spacings are less likely. The average value of the distribution is $\langle x \rangle = 1$ and its variance $\sigma^2 = (4/\pi - 1)$. The relative uncertainty of the average level spacing calculated from N resonances is

$$\frac{\Delta\langle D \rangle}{\langle D \rangle} = \sqrt{\frac{1}{N}\left(\frac{4}{\pi} - 1\right)}. \tag{A.10}$$

A.3 Strength functions

The neutron strength function S_ℓ is, together with the average level spacing $\langle D \rangle$ and the radiative width $\langle \Gamma_\gamma \rangle$, one of the main ingredients of the optical model calculations for high energy neutron cross sections. For a given angular momentum ℓ the strength function is calculated as

$$S_\ell = \frac{\langle g_J \Gamma^\ell_{\lambda n} \rangle}{\langle D_\ell \rangle} = \frac{1}{\Delta E} \sum_J \sum_\lambda g_J \Gamma^{\ell,J}_{\lambda n}, \tag{A.11}$$

where Roman subscripts refer to reaction channel and Greek subscripts to compound-nucleus levels. Here, ΔE is the energy range considered and $\Gamma^{\ell,J}_{\lambda n}$ is the reduced neutron width for a resonance with spin J and orbital momentum ℓ. The uncertainty of the strength function when it is calculated from a set of N resonances in the range ΔE is given by

$$\frac{\Delta S_\ell}{S_\ell} = \sqrt{\frac{1}{N}\left(\frac{4}{\pi} + 1\right)}. \tag{A.12}$$

Appendix B
Black Resonance Filters

In order to facilitate background studies in time of flight experiments, it is customary to put in the neutron beam-line a filter station where different slots can hold a filter consisting of materials with strong neutron resonances. These are called black resonances, or background, filters.

At n_TOF, the filter station is installed at 140 m from the spallation target, just in front of the first collimator. The filters are chosen thick enough to completely absorb the neutron beam at the energies of the strong resonances. Therefore, all the counts measured in the neighbourhood of the so-called black resonances can be attributed to the background. In Table B.1 the filters used in the n_TOF Phase-2 are listed.

Table B.1: Energy and thickness of the black resonance filters used in n_TOF experiments.

Element	**Resonance Energy (eV)**	**Thickness (atoms/barn)**
Ag	5.19	2.9×10^{-3}
W	18.8	5.0×10^{-3}
Mo	44.9	6.4×10^{-3}
Co	132.0	2.3×10^{-3}
Al	34.83 10^3 86.27 10^3	0.177

Black filters affect both the intensity and the shape of the neutron flux, as can be seen in Figure B.1. When filters are in beam, in fact, a decrease in the counting rate is visible not only at the black-resonance energies, and therefore combinations of different filters have to be adopted depending on the energy region one is interested in. At n_TOF the filter station can be operated remotely from the control room, allowing to change the configuration during measurements campaign.

In Figure B.2 an example of the attenuation of the neutron flux is shown for a measurement with Ag, W, Co and Al background filters. The presence of aluminum filter in-beam results in a loss of about 30% of incoming neutrons. Therefore it should be placed in the beam only for particular measurements, which requires an extremely careful determination of the background at high energy. This is the case, for example, of C_6D_6 scintillator measurement for the Unresolved Resonance Region.

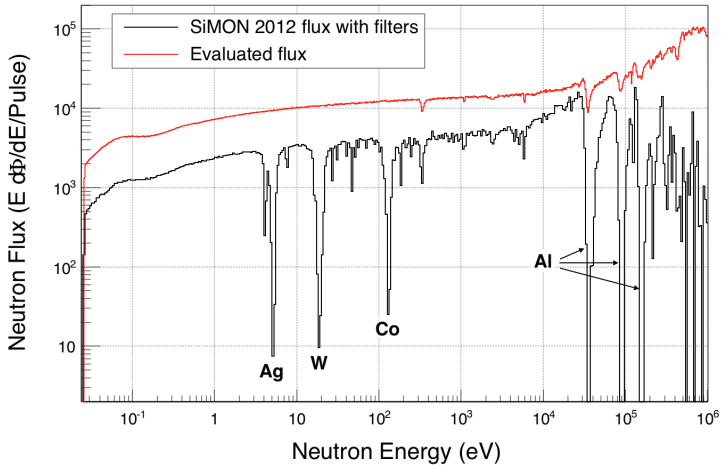

Fig. B.1: Typical neutron flux measurement with Ag, W, Co and Al black resonance filters at n_TOF. Six strong suppression of counts can be seen at TOF corresponding to the energy of the big resonances in Ag, W, Co and three resonances of Al.

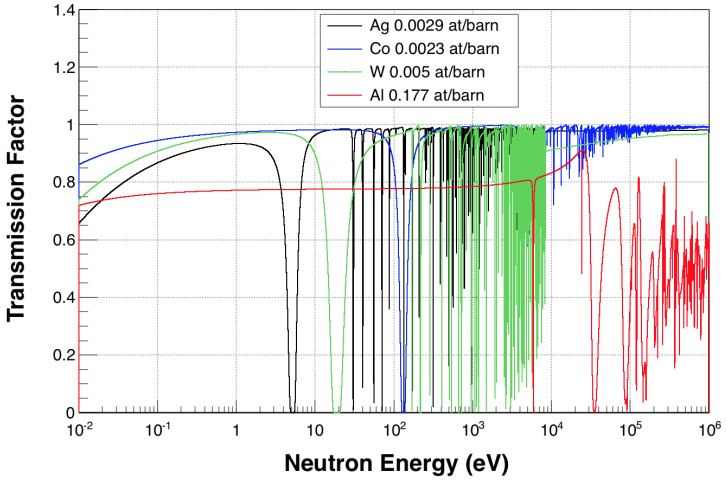

Fig. B.2: Neutron flux attenuation due to Ag, W, Co and Al background filters in beam.

References

1. NEA-HPRL, High Priority Request List, hwww.nea.fr/html/dbdata/hprli.
2. P. Schillebeeckx *et al.*, *Total and radiative capture cross section measurements for ^{238}U at GELINA and n_ TOF*, The ANDES deliverable 1.8 of Work Package 1 - Task 1.2, European Union, 2013.
3. World Energy Council, Conseil Mondial de l'Énergie, http://www.worldenergy.org.
4. World Energy Council, *Energy for tomorrow's world*, London, 1993.
5. World Energy Council, *World Energy Resources, 2013 Survey*, London, 2013.
6. International Energy Agency, www.iea.org.
7. International Energy Agency, *World Energy Outlook 2013*, Paris, 2013.
8. International Energy Agency, *CO_2 Emissions from Fuel Combustion - Highlights*, Paris, 2014.
9. Greenpeace International, European Renewable Energy Council (EREC), Global Wind Energy Council (GWEC), *Energy [R]evolution - A Sustainable World Energy Outlook*, available from http://www.greenpeace.org/international/en/publications/Campaign-reports/Climate-Reports/Energy-Revolution-2012/, 2012.
10. B.W. Brook, *Could nuclear fission energy, etc., solve the greenhouse problem? The affirmative case*, Energy Policy **42** (2012) 4.
11. B.W. Brook and C.J.A. Bradshaw, *Key role for nuclear energy in global biodiversity conservation*, Conservation Biology, **0** (2014) 1.
12. S. Hong, C.J.A. Bradshaw and B.W. Brook, *Evaluating options for the future energy mix of Japan after the Fukushima nuclear crisis*, Energy Policy **56** (2013) 418.
13. M. Nicholson, T. Biegler and B.W. Brook, *How carbon pricing changes the relative competitiveness of low-carbon baseload generating technologies*, Energy **36** (2011) 305.
14. International Energy Agency, *Energy Technology Perspectives 2014 - Harnessing ElectricityÕs Potential*, http://www.iea.org/etp/.
15. M. Nicholson, *The Power Maker's Challenge*, Springer-Verlag, London, 2012.
16. T. Trainer, *Can renewables etc. solve the greenhouse problem? The negative case*, Energy Policy **38** (2010) 4107.
17. R.E. Grumbine and M.K. Pandit, *Threats from India's Himalaya dams*, Science **339** (2013) 36.
18. P. Kyle, L. Clarke, G. Pugh, M. Wise, K. Calvin, J. Edmonds and S. Kim, *The value of advanced technology in meeting 2050 greenhouse gas emissions targets in the United States*, Energy Economics **31** (2009) S254.
19. M. Finer and C.N. Jenkins, *Proliferation of hydroelectric dams in the Andean Amazon and implications for Andes-Amazon connectivity*, PLOS ONE **7** (2012) 35126.

20. W.F. Laurance, M. Goosem and S.G.W. Laurance, *Impacts of roads and linear clearings on tropical forests*, Trends in Ecology and Evolution **24** (2009) 659.
21. International Energy Agency, *World Energy Outlook 2014*, Paris, 2014.
22. K.S. Krane, *Introductory Nuclear Physics*, John Wiley & Sons Inc.,1988.
23. D. Bodansky, *Nuclear Energy, Principles, Practices, and Prospects*, Springer, 2nd edition, 2004.
24. World Nuclear Association, http://www.world-nuclear.org.
25. W.M. Stacey, *Nuclear Reactor Physics*, Wiley Interscience, 2001.
26. International Energy Agency, *Design Features and Operating Experience of Experimental Fast Reactors*, IAEA Nuclear Energy Series No. NP-T-1.9, Vienna, 2013.
27. International Energy Agency, *Status of Innovative Fast Reactor Designs and Concepts*, http://www.iaea.org/NuclearPower/Downloadable/FR/booklet-fr-2013.pdf, 2013.
28. International Energy Agency, *IAEA Annual Report 2013*, http://www.iaea.org/sites/default/files/anrep2013_full_0.pdf, 2013.
29. Generation IV International Forum (GIF), https://www.gen-4.org/gif/jcms/c_9260/Public.
30. Generation IV International Forum (GIF), https://www.gen-4.org/gif/jcms/c_9357/gfr.
31. Generation IV International Forum (GIF), https://www.gen-4.org/gif/jcms/c_9358/lfr.
32. Generation IV International Forum (GIF), https://www.gen-4.org/gif/jcms/c_9359/msr.
33. Generation IV International Forum (GIF), https://www.gen-4.org/gif/jcms/c_9360/scwr.
34. Generation IV International Forum (GIF), https://www.gen-4.org/gif/jcms/c_9361/sfr.
35. Generation IV International Forum (GIF), https://www.gen-4.org/gif/jcms/c_9362/vhtr.
36. Sustainable Nuclear Energy Technology Platform, *European Sustainable Nuclear Industrial Initiative (ESNII)* http://www.snetp.eu/esnii/.
37. International Energy Agency, *Classification of Radioactive Waste - General Safety Guide*, IAEA Safety Standards Series No. GSG-1, IAEA, Vienna, 2009.
38. International Energy Agency, *Application of the Concepts of Exclusion, Exemption and Clearance*, IAEA Safety Standards Series No. RS-G-1.7, IAEA, Vienna, 2004.
39. Y. Kadi and J.P. Revol, *Design of an Accelerator-Driven System for the Destruction of Nuclear Waste*, Workshop on Hybrid Nuclear System for Energy Production Utilization of Actinides and Transmutation of Long-Lived Radioactive Waste, Trieste, 2001.

40. International Commission on Radiological Protection, *Age-Dependent Doses to Members of the Public from Intake of Radionuclides, Part 5. Compilation of Ingestion and Inhalation Dose Coefficients*, ICRP Publication 72, Pergamon Press, Oxford (1996).
41. Nuclear Energy agency (NEA), *Spent Nuclear Fuel Assay Data for Isotopic Validation - State-of-the-art Report*, Nuclear Science NEA/NSC/WPNCS/DOC(2011)5, OEDC 2011.
42. J.C. Wagner *et al.*, *Categorization of Used Nuclear Fuel Inventory in Support of a Comprehensive National Nuclear Fuel Cycle Strategy*, ORNL/TM-2012/308, FCRD-FCT-2012-000232, 2012.
43. RED-IMPACT Synthesis Report, *Impact of Partitioning, Transmutation and Waste Reduction Technologies on the Final Nuclear Waste Disposal*, Forschungszentrum Jülich, 2008.
44. M. Salvatores, I. Slessarev and A. Tchistiakov, *The transmutation of long-lived fission products by neutron irradiation*, Nucl. Sci. and Eng. **130** (1998) 309.
45. W. Gudowski, *Accelerator-driven transmutation projects. The importance of nuclear physics research for waste transmutation*, Nuclear Physics A **654** (1999) C436.
46. C. Rubbia et al., *An Energy Amplifier for cleaner and inexhaustible nuclear energy production driver by a particle beam accelerator*, CERN/AT/93-47(ET), 1993.
47. OECD Nuclear Energy Agency, *Accelerator-Driven Systems ADS and Fast Reactor Fr in advanced nuclear fuel cycles. A comparative study*, 2002.
48. Kyoto University Critical Assembly, http://www.rri.kyoto-u.ac.jp/en/facilities/ca.
49. Bhaba Atomic Research Center, Advanced reactor technology and nuclear power, http://www.barc.gov.in/randd/artnp.html.
50. The MYRRHA project, http://myrrha.sckcen.be/en.
51. The European Spallation Source, http://europeanspallationsource.se.
52. IAEA-NDS, Experimental nuclear reaction data. www.nds.iaea.org/EXFOR.
53. JEFF, Joint European fission and fusion file, https://www.oecd-nea.org/dbdata/jeff/#library.
54. JENDL, Japanese Evaluated Nuclear Data Library, http://wwwndc.jaea.go.jp/jendl/jendl.html.
55. ENDF, Evaluated Nuclear Data File, https://www-nds.iaea.org/exfor/endf.htm.
56. BROND, Russian Evaluated Neutron Data Library, http://www.ippe.obninsk.ru/podr/cjd/.
57. Zhuang Youxiang *et al.*, *CENDL-3 - Chinese Evaluated Nuclear Data Library, Version 3*, Journal of Nuclear Science and Technology, **39:sup2** (2002) 37.
58. M. Herman, *ENDF-6 Formats Manual*, Technical Report BNL-NCS-44945-05-Rev., Brookhaven National Laboratory, 2005.
59. M.B. Chadwick *et al.*, *The CIELO Collaboration: Neutron reactions on ^{1}H, ^{16}O, ^{56}Fe, $^{235,238}U$, and ^{239}Pu*, Nuclear Data Sheets **118** (2014) 1.

60. P.G. Young et al., Los Alamos National Laboratory report LA-12343-MS (1992).
61. C. Lampoudis *et al.*, *^{238}U Neutron Capture Cross Section Measurements at the GELINA Facility*, Nuclear Data Sheets **119** (2014) 14.
62. F. Mingrone *et al.*, *Measurement of the ^{238}U Radiative Capture Cross Section with C6D6 at the CERN n_ TOF Facility*, Nuclear Data Sheets **119** (2014) 18.
63. T. Wright *et al.*, *High-precision Measurement of the ^{238}U(n,γ) Cross Section with the Total Absorption Calorimeter (TAC) at n_ TOF, CERN*, Nuclear Data Sheets **119** (2014) 26.
64. Project FP7-249671 of the EURATOM FP7 ANDES, hwww.andes-nd.eu//i.
65. K.H. Böckhoff, A.D. Carlson, O.A. Wasson, J.A. Harvey and D.C. Larson, *Electron linear accelerators for fast neutron data measurements in support of fusion energy applications*, Nucl. Sci. & Eng. **106** (1990) 192.
66. W. Mondelaers and P. Schillebeeckx, *GELINA, a neutron time-of-flight facility for neutron data measurements*, Notiziario **11** (2006) 19.
67. G. A. Linenberger *et al.*, Los Alamos Scientific Laboratory Report No. 179, 1944 (unpublished).
68. M.P. Fricke, W.M. Lopez, S.J. Friesenhahn, A.D. Carlson and D.G. Costello, *Measurements of cross sections for radiative capture of 1-keV to 1-MeV neutrons by Mo, Rh, Gd, Ta, W, Re, Au and U-238*, Conf.: Nuclear Data for Reactors Conf., Helsinki Vol.2, p.265 (1970).
69. Yu.G. Panitkin and V.A. Tolstikov, *Radiative capture of neutrons by U-238 in the energy range 0.024 - 1.1 MeV*, Neutron Physics Conference, Kiev, Ukraina (1971) Vol.1, p.321.
70. W.P. Poenitz, *Measurements of the Neutron Capture Cross Sections of Gold-197 and Uranium-238 Between 20 and 3500 keV*, Nuclear Science and Engineering **57** (1975) 300.
71. M.G. Sowerby, *Summary of the Work of the NEANDC Task Force on U-238*, NEANDC-313U, Nuclear Energy Agency OECD, Paris, France (1994).
72. G. de Saussure, D.K. Olsen, R.B. Perez and F.C. Difilippo, Prog. in Nucl. En. **3** (1979) 87.
73. M.C. Moxon and M.G. Sowerby, *A review of the U-238 resolved resonance parameters* Harwell Report AERE-R 10597 (1982).
74. A. Courcelle, *Needs for Nuclear Data Measurements to Improve LEU-LWR Reactivity Prediction*, Note to WPEC Sub-group 22 (2003).
75. H. Derrien, L.C. Leal, N.M Larson and A. Courcelle, *Neutron Resonance Parameters of ^{238}U and the Calculated Cross Sections from the Reich-Moore Analysis of Experimental Data in the Neutron Energy Range from 0 keV to 20 keV*, ORNL/TM-2005/241, Oak Ridge National Laboratory (2005).

76. W.P. Poenitz, L.R. Fawcett, Jr. and D.L. Smith, *Measurement of the $^{238}U(n,\gamma)$ Cross Sections at Thermal and Fast Neutron Energies*, Nuclear Science and Engineering **78(3)** (1981) 239.
77. F. Corvi and G. Fioni, *Shape of the ^{238}U Neutron Capture Cross Section in the Range 0.002Ð0.1 eV*, Nuclear Data for Science and Technology, Mito, Japan (1988).
78. A. Meister *et al.*, *Experimental Study of the Doppler Broadening of Neutron Resonances at GELINA*, pp. 435Ð439 in Conference on Nuclear Data for Science and Technology, Trieste, Italy (1998).
79. G. de Saussure *et al.*, *Measurement of the ^{238}U Capture Cross Section for Incident Neutron Energy up to 100 keV*, ORNL/TM-4059, Oak Ridge National Laboratory (1973).
80. D.K. Olsen *et al.*, *Precise Measurement and Analysis of Neutron Transmission through Uranium-238*, Nucl. Sci. Eng. **2(3)** (1977) 479.
81. D.K. Olsen *et al.*, *Measurement and Resonance Analysis of Neutron Transmission through Uranium-238*, Nucl. Sci. Eng. **69(2)** (1979) 202.
82. R.L. Macklin *et al.*, *High Resolution Measurement of the ^{238}U Neutron Capture Yield from 1 to 100 keV*, Ann. Nucl. Energy, **18(10)** (1991) 567.
83. J.A. Harvey *et al.*, *High Resolution Transmission Measurements on ^{235}U, ^{239}Pu, and ^{238}U*, Nuclear Data for Science and Technology, Mito, Japan (1988).
84. M.C. Moxon, *The neutron Harwell capture cross section of U-238 in the energy region 5.2 to 250 keV (revised data)* (unpublished) (2006).
85. M.C. Moxon, Harwell Report AERE-R 6074 (1969).
86. J.L. Ullman *et al.*, *Measurement of the ^{238}U Neutron-capture Cross Section and Gamma-emission Spectra from 10 eV to 100 keV Using the DANCE Detector at LANSCE*, J. Korean Phys. Soc., **59** (2011) 1406.
87. J.L. Ullmann *et al.*, *Cross section and γ-ray spectra for 238U(n,γ) measured with the DANCE detector array at the Los Alamos Neutron Science Center*, Phys. Rev. C **89** (2014) 034603.
88. M. Lindner, R.J. Nagle and J.H. Landrum, *Neutron Capture Cross Sections from 0.1 to 3 MeV by Activation Measurements*, Nuclear Science and Engineering **59/04** (1976) 381.
89. H. Feshbach, A.K. Kerman and R.H. Lemmer, *Intermediate structure and doorway states in nuclear reactions*, Annals of Physics **41** (1967) 230.
90. F.H. Fröhner, *Evaluations and Analysis of Nuclear Resonance Data*, AEN-NEA JEFF Report 18 (2000).
91. F.H. Fröhner, *Nuclear theory for Applications*, Report IAEA-SMR-43, ICPT Trieste (1980) 59.
92. E.P. Wigner and L. Eisenbund, *Higher angular momenta and long range interaction in resonance reactions*, Physics Review **72** (1947) 29.

93. A.M Lane and R.G. Thomas, *R-Matrix Theory of Nuclear Reactions*, Review of Modern Physics **30** (1958) 257.
94. J. E. Lynn, *The Theory of Neutron Resonance Reactions*, Clarendon Press, Oxford (1968).
95. W. Hauser and H. Feshbach, *The Inelastic Scattering of Neutrons*, Physical Review **87** (1952) 366.
96. F. H. Fröhner, Nucl. Sci. Eng. **103** (1989) 119.
97. H. Feshbach, *Theoretical Nuclear Physics; Nuclear Reactions*, John Wiley & Sons (1991).
98. E. Bauge, J. P. Delaroche, M. Giro, *Lane-consistent, semimicroscopic nucleon-nucleus optical model*, Phys. Rev. C **63** (2001) 024607.
99. N. Bohr, *Neutron Capture and Nuclear Constitution*, Nature **137** (1936) 344.
100. F. Gunsing, *Neutron resonance spectroscopy*, CEA/Saclay, DSM/DAPNIA/SPhN.
101. G. Breit and E.P. Wigner, *Capture of slow neutrons*, Physical Review **49** (1936) 519.
102. V.H. Weisskopf and E.P. Wigner, Z. Physics **63** (1930) 54; **65** (1930) 18.
103. S.F. Mughabghab, *Atlas of Neutron Resonances, Resonance Parameters and Thermal Cross Sections, Z=1-100*, Elsevier (2006).
104. C.E. Porter and R.G. Thomas, *Fluctuations of nuclear reactions widths*, Physical Review **104** (1956) 483.
105. C.W. Reich and M.S. Moore, *Multilevel Formula for the fission process*, Physical Review **111** (1958) 929.
106. E. Browne, J. K. Tuli, Nuclear Data Sheets 122 (2014) 293.
107. R. E. Chrien and J. Kopecky, *The nuclear structure of $^{239}U^{*}$*, Nuclear Physics A **414** (1984) 281.
108. Evaluated Nuclear Structure Data File (ENSDF) Retrieval, http://www.nndc.bnl.gov/ensdf/.
109. P. A. Moldauer, *Statistics and the average cross section*, Nuclear Physics A **344** (1980) 185.
110. N. M. Larson, *Updated users guide for Sammy: multilevel R-matrix fits to neutron data using Bayes equations*, ORNL/TM-9179/R8, Oak Ridge National Laboratory, Oak Ridge, TN, USA (2008). Also ENDF-364/R2.
111. H. E. Jackson and J. E. Lynn, *Resonant absorption of neutrons by crystals*, Physical Review *127* (1962) 461.
112. F.H. Fröhner, E. Haddad, W.M. Lopez and S.J. Friesenhahn, *Accuracy of resonance parameters from combined area and self-indications measurements*, Proceedings of the International Conference on Neutron Cross Section Technology, Washington, D.C., 22-24 March (1996) 55-66.

113. D.J. Hughes, *A method for rapid analysis of neutron resonances*, J. Nuclear Energy **1** (1955) 237.
114. M.B. Chadwick *et al.*, *ENDF/B-VII.1 Nuclear Data for Science and Technology: Cross Sections, Covariances, Fission Product Yields and Decay Data*, Nuclear Data Sheets **112** (2011) 2887.
115. F.H. Fröhner, O. Bouland, *Treatment of external levels in neutron resonance fitting: application to the non-fissile nuclide* ^{52}Cr, Nucl. Sci. & Eng. **137** (2001) 70.
116. A. Foderaro, *The elements of neutron interaction theory*, Cambridge, MIT Press (1971).
117. P. Schillebeeckx *et al.*, *Determination of Resonance Parameters and their Covariances from Neutron Induced Reaction Cross Section Data*, Nuclear Data Sheets **113** (2012) 3054.
118. F.G.P. Seidl, *Fast chopper Time-of-Flight Measurement of Neutron Resonances*, Physical Review **95** (1954) 476.
119. M.E. Overberg, B.E. Moretti, R.E. Slovacek and R.C. Block, *Photoneutron target development for the RPI linear accelerator*, Nucl. Instr. Meth. A **438** (1999) 253.
120. K. Kino *et al.*, *Measurement of energy spectra and spatial distributions of neutron beams provided by the ANNRI beam line for capture cross-section measurements at the J-PARC/MLF*, Nucl. Instr. Meth. A **626−627** (2011) 58 − 66.
121. P.W. Lisowski and K.F. Schoenberg, *The Los Alamos neutron science center*, Nucl. Inst. Meth. A **562** (2006) 910.
122. The n_TOF Collaboration, *CERN n TOF Facility: Performance Report*, CERN INTC-2002-037 (2003).
123. C. Guerrero *et al.*, *Performance of the neutron time-of-flight facility n TOF at CERN*, European Physics Journal A **49** (2013) 27.
124. G. Lorusso *et al.*, *Time-energy relation of the n TOF neutron beam: energy standards revisited*, Nuclear Instruments and Methods in Physics Research A **532** (2004) 622.
125. C. Coceva, R. Simonini and D. K. Olsen, *Calculation of the ORELA neutron moderator spectrum and resolution function*, Nucl. Instr. Meth. **211** (1983) 459.
126. P.E. Koehler, *A determination of the energy resolution at LANSCE*, Nucl. Instr. Meth. A **350** (1994) 511.
127. M.C. Moxon and J.B. Brisland, *GEEL REFIT, A least squares fitting program for resonance analysis of neutron transmission and capture data computer code*, AEAInTec-0630, AEA Technology, October (1991).
128. C. Rubbia et al., Tech. Rep. CERN/LHC/98-02, CERN (1998).
129. http://home.web.cern.ch/about/updates/2013/02/long-shutdown-1-exciting-times-ahead.
130. The n_TOF Collaboration, *n TOF Experimental Area 2 (EAR2) preliminary feasibility study*, CERN-INTC-2011-032 / INTC-O-013 (2011).

131. The n TOF Collaboration, *Proposal for n TOF Experimental Area 2 (EAR-2).* CERN-INTC-2012-029 / INTC-O-015 (2012).
132. The CERN Accelerator Complex, http://public.web.cern.ch/public/en/research/AccelComplex-en.html.
133. U. Abbondanno *et al.*, Tech. Rep. CERN-SL-2002-053 ECT, (2003).
134. The n TOF Collaboration, *The neutron Time-Of-Flight facility, n_ TOF, at CERN (I): Technical Description*, CERN-n_TOF-PUB-2013-001 (2013).
135. S. Marrone *et al.*, Nuclear Instruments and Methods in Physics Research A **517** (2004) 389.
136. Y. Giomataris *et al.*, *Micromegas: a high granularity position sensitive gaseous detector for high particle-flux environments* Nuclear Instruments and Methods in Physics Research A **376** (1996) 29.
137. G. Charpak *et al.*, *First beam test results with Micromegas, a high-rate, high resolution detector*, CERN-LHC/97-08 (EET), DAPHNIA-97-05.
138. S. Andriamonje *et al.*, *A transparent detector for n_ TOF neutron beam monitoring*, Journal of the Korean Physical Society **59** 2 (2011) 1597.
139. S. Andriamonje *et al.*, *Development and performance of Microbulk Micromegas detectors*, Proceedings of the 1st International Conference on Micro-Pattern Gaseous Detectors, Crete, Greece, 2009.
140. C. Paradela *et al.*, Physical Review C **82** (2010) 034601.
141. L. Tassan-Got *et al.*, *Angular distributions in the neutron-induced fission of actinides*, CERN-INTC-2006-016, INTC-P-209.
142. U. Abbondanno *et al.*, *The data acquisition system of the neutron time-of-flight facility n_ TOF at CERN*, Nuclear Instruments and Methods in Physics Research A **538** (2005) 692.
143. S. Marrone *et al.*, *Pulse shape analysis of liquid scintillators for neutron studies*, Nuclear Instruments and Methods in Physics Research A **490** (2002) 299.
144. S. Marrone *et al.*, *Pulse shape analysis of signals from BaF_2 and CeF_3 scintillators for neutron capture experiments*, Nuclear Instruments and Methods in Physics Research A **568** (2006) 904.
145. CERN Advanced STORage manager, castor.web.cern.ch.
146. A. Ferrari and P.R. Sala, *Intermediate and High Energy Physics Models in FLUKA: Improvements, Benchmarks and Applications*, Proc. Int. Conf. on Nuclear Data for Science and Technology, NDST-97, ICTP, Miramare, Trieste, Italy, (19-24 May 1997).
147. C. Coceva *et al.*, Nuclear Instruments and Methods in Physics Research A **489** (2002) 346.
148. F. Gunsing *et al.*, *Measurement of resolved resonances of $^{232}Th(n,\gamma)$ at the n_ TOF facility at CERN*, Phys. Rev. C 85 (2012) 064601.

149. J. Briesmeister, *MCNP-A General Monte Carlo N-Particlke Transport Code-Version 4c2*, LA-13709-M (2000).
150. F. Gunsing *et al.*, *Status and outlook of the neutron time-of-flight facility n_ TOF at CERN*, NIM B 261 (2007) 925.
151. M. Barbagallo *et al.*, *High-accuracy determination of the neutron flux at n_ TOF*, Eur. Phys. J. A **49** (2013) 156.
152. A.D. Carlson, V.G. Pronyaev, D.L. Smith, N.M. Larson, C. Zhenpeng, G.M. Hale, F.J. Hambsch, E.V. Gai, Soo-Youl Oh, S.A. Badikov, T. Kawano, H.M. Hofmann, H. Vonach, S. Tagesen, Nucl. Data Sheets, *International Evaluation of Neutron Cross Section Standards*, **110** (2009) 3215.
153. D.B. Gayther, Metrologia **27** (1990) 221.
154. F. Belloni *et al.*, *Neutron beam imaging with an XY-micromegas detector at n_ TOF at CERN*, Phys. Scr. (2012) 014004.
155. M. Heil, R. Reifarth, M.M. Fowler, R.C. Haight, F. Kä, R.S. Rundberg, E.H. Seabury, J.L. Ullmann, J.B. Wilhelmy, K. Wisshak, *A 4π BaF_2 detector for (n, γ) cross-section measurements at a spallation neutron source*, Nuclear Instruments and Methods in Physics Research, A **459** (2001) 229-246.
156. C. Guerrero *et al.*, Nuclear Instruments and Methods in Physics Research A **608** (2009) 424Ð433.
157. M.C. Moxon and E.R. Rae, Nuclear Instruments and Methods **24** (1963) 445.
158. F. Corvi, *The measurement of neutron capture cross sections via prompt gamma-ray detection*, in: C. Coceva, et al. (Eds.), Proceedings Specialists Meeting on Measurement, Calculation and Evaluation of Photon Production Data (Bologna 1994) Report NEA/NSC/DOC (95) 1, pp. 229Ð246.
159. R.L. Macklin and J.H. Gibbons, Phys. Rev. **159** (1967) 1007.
160. R. Plag *et al.*, Nuclear Instruments and Methods in Physics Research A **496** (2003) 425.
161. F. Corvi, G. Fioni, F. Gasperini, P. B. Smith, *The weighting function of a neutron capture detection system*, Nuclear Science and Engineering **107** (1991) 272.
162. U. Abbondanno *et al.*, Nuclear Instruments and Methods in Physics Research A **521** (2004) 454.
163. GEANT, *Detector description and simulation tool*, CERN Program Library W5013 (1994).
164. C. Domingo-Pardo *et al.*, Physical Review C **74** (2006) 025807-1.
165. R.L. Macklin, J. Halperin and R.R. Winters, *Absolute neutron capture yield calibration*, Nuclear Instruments and Methods **164** (1979) 213.
166. M.S. Moore, *Rate dependence of counting losses in neutron time-of-flight measurements*, Nuclear Instruments and Methods **169** (1980) 245.

167. A. Borella *et al.*, Nuclear Instruments and Methods in Physics Research A **577** (2007) 626.
168. P. Žugec *et al.*, Nuclear Instruments and Methods in Physics Research A **760** (2014) 57.
169. S. Agostinelli, J. Allison, K. Amako *et al.*, Nuclear Instruments and Methods in Physics Research A **506** (2003) 250.
170. E. Mendoza, D. Cano-Ott, C. Guerrero, R. Capote, IAEA Technical Report INDC (NDS)-0612, Vienna, 2012.
171. R. Brun and F. Rademakers, *ROOT - An Object Oriented Data Analysis Framework*, Nuclear Instruments and Methods in Physics Research A **389** (1997) 81. See also http://root.cern.ch/.
172. G. Arerts *et al.*, *Neutron capture cross section of ^{232}Th measured at the n_ TOF facility at CERN in the unresolved resonance region up to 1 MeV*, Physical Review C **73** (2006) 054610.
173. N. Colonna *et al.*, *Time-energy relation to the n_ TOF neutron beam: energy standards revisited*, Nuclear Instruments and Methods in Physics Research A **532** (2004) 662.
174. T. Belgya et al., *Handbook for calculations of nuclear reaction data*, RIPL-2. IAEA-TECDOC-1506 (2006).
175. E. P. Wigner., Proc. Int. Conf. Neutron Physics by Time-of-Flight, Gatlinburg Tennessee, ORNL-2309 (1956).